Strong-field Breit-Wheeler pair creation in various physical scenarios

Inaugural-Dissertation

zur Erlangung des Doktorgrades der
Mathematisch-Naturwissenschaftlichen Fakultät der
Heinrich-Heine-Universität Düsseldorf

vorgelegt von

Alina Golub
aus Chmelnizkij

Düsseldorf, August 2022

aus dem Institut für Theoretische Physik I
der Heinrich-Heine-Universität Düsseldorf

Gedruckt mit der Genehmigung der
Mathematisch-Naturwissenschaftlichen Fakultät der
Heinrich-Heine-Universität Düsseldorf

Berichterstatter:
1. Prof. Dr. Dr. Carsten Müller
2. Prof. Dr. Reinhold Egger
3. Prof. Dr. Reinhard Alkofer

Tag der mündlichen Prüfung:
9. Dezember 2022

Zusammenfassung

In der vorliegenden Arbeit wird eine theoretische Betrachtung des Starkfeld-Prozesses der Breit-Wheeler-Paarerzeugung in verschiedenen Szenarien und Kopplungsregimen dargestellt. Dabei wird sowohl die Erzeugung von Elektron-Positron-Paaren in der Quantenelektrodynamik als auch von Quasiteilchen-Loch-Paaren in speziellen Festkörpersystemen untersucht, und es werden Querverbindungen zwischen diesen Phänomenen hergestellt.

Der lineare und der nicht-perturbative Prozess im starken Feld werden im Rahmen von Versuchsanordnungen diskutiert, bei denen Bremsstrahlungsphotonen mit den Energien bis zu mehreren GeV mit den elektromagnetischen Feldern eines Röntgenlasers (für den Zwei-Photonen-Fall) oder eines hochintensiven optischen Lasers (im nicht-perturbativen Bereich) wechselwirken. Als Ergebnis werden Prognosen zu der Anzahl von erzeugten Paaren gegeben. Im nicht-perturbativen Regime wird ein besonderes Augenmerk auf die Effekte der longitudinalen und transversalen Laserfokussierung gelegt, da die erforderlichen hohen Intensitäten nur bei eng fokussierten Laserpulsen erreichbar sind. Darüber hinaus wird die Paarbildung in einem alternativen theoretischen Gerüst der Quantenelektrodynamik im 2+1-dimensionalen Minkowski-Raum untersucht. In diesem Zusammenhang werden Veränderungen hervorgehoben, die durch die Verringerung der Anzahl von Raumdimensionen hervorgerufen werden, wie z.B. nicht verschwindende Beiträge der Teilchenraten an der Energieschwelle, wenn die Gesamtzahl der beteiligten Photonen ungerade ist. Zusätzlich wird die Abhängigkeit der Anzahl der erzeugten Paare vom Quanten-Nichtlinearitätsparameter im nicht-perturbativen Bereich modifiziert.

Schließlich wird die Zwei- und Drei-Photonen-Erzeugung von Quasiteilchen-Loch-Paaren in einem Festkörpersystem aus monolagigem Graphen mit einer Lücke zwischen den Valenz- und Leitungsbändern untersucht. Dabei werden Photonen mit Energien im eV-Bereich verwendet. Da die Prozessraten durch ein Modell beschrieben werden, das der modifizierten niederdimensionalen Quantenelektrodynamik ähnelt, zeigen sie das charakteristische Verhalten einer 2+1-dimensionalen Rechnung.

Abstract

In the present work a theoretical consideration of the Breit-Wheeler pair creation in various scenarios and coupling regimes is presented. Both the generation of electron-positron pairs in quantum electrodynamics and of quasiparticle-hole pairs in special solid-state systems are investigated, and cross-connections between these phenomena are established.

Thus, linear and strong field nonperturbative processes are discussed in setups, where several GeV bremsstrahlung photons impinge on a field of an x-ray (for the two-photon case) or high intensity optical (in nonperturbative regime) lasers, respectively, and estimations for the numbers of created pairs are provided. For the latter, special attention is paid to the effects of the longitudinal and transversal laser focusing since the required high intensities are achievable only in tightly focused laser pulses. Moreover, the pair creation in an alternative framework of quantum electrodynamics in 2+1 dimensional Minkowski spacetime is studied. In this context, peculiar changes induced by the reduction of space dimensions are highlighted such as nonvanishing contributions of the particle rates at the energy threshold when the total number of participating photons is odd. Additionally, the dependence of the number of created pairs on the quantum nonlinearity parameter in the nonperturbative regime is altered.

Finally, the two- and three-photon production of quasiparticle-hole pairs are studied in a solid state system of monolayered bandgapped graphene when using photons with energies in the eV range. To that end, the reaction rates are derived in a framework similar to the lower dimensional quantum electrodynamics and show characteristic behaviour of a 2+1 dimensional study.

Acknowledgments

I would like to gratefully acknowledge the supervision of Prof. Dr. Dr. Carsten Müller, which was always distinguished by understanding, motivation, support and great ideas. Moreover, many thanks go to my co-supervisor Dr. Selym Villalba-Chávez, who showed me how to become a physicist and steadily improve on the way, as well as to my great mentor Dr. Götz Lehmann, who finds the right words all the time when needed and has an excellent taste in cookies. I would also like to thank Alexandra Eckey, Lars Reichwein, Andreas Jacob and my dear officemate Fiona Grüll for bringing some fun to our work along with the participation in useful discussions and sharing of ideas. Furthermore, I am grateful to Elvira Gröters, Ute Birkenkamp-Pickshaus and Eugen Braun for ensuring the trouble-free life at the institute. Lastly, this thesis is dedicated to my family, who were always there for me regardless the complexity and duration of my endeavours.

List of publications

Results obtained in the scope of the present thesis were published in

1. **A. Golub**, R. Egger, C. Müller and S. Villalba-Chávez, *Dimensionality-driven photoproduction of massive Dirac pairs near threshold in gapped graphene monolayers*. Phys. Rev. Lett. **124**, 110403 (2020) [selected as an Editor's Suggestion].

In the above publication the Breit-Wheeler production of quasiparticle-hole pairs in bandgapped graphene occurring as a result of collisions of two and three laser photons was investigated. In this study I calculated the corresponding particle rates and produced the associated figure as well as contributed to the preparation of the manuscript.

2. **A. Golub**, S. Villalba-Chávez, H. Ruhl and C. Müller, *Linear Breit-Wheeler pair production by high-energy bremsstrahlung photons colliding with an intense x-ray laser pulse*. Phys. Rev. D **103**, 016009 (2021).

Here, a possible setup for observation of linear Breit-Wheeler pair creation was studied theoretically. The calculations of the estimated number of created pairs involving a focused description of the laser pulse and energy distribution of bremsstrahlung photons were provided by me. Moreover, I conducted all numerical studies, generated corresponding figures and prepared the manuscript.

3. **A. Golub**, S. Villalba-Chávez and C. Müller, *Strong-field Breit-Wheeler pair production in* QED_{2+1}. Phys. Rev. D **103**, 096002 (2021).

A discussion on the Breit-Wheeler particle production in a realm with lowered number of spacial dimensions from three to two is presented in the publication above. The corresponding rate of created particles in the Furry picture was established by me. In addition, the particular interest was paid to the regimes of the pair creation on the energy threshold as well as for low and high intensity parameters. To that end, I calculated the corresponding asymtotes and, also, prepared the manuscript.

4. F. C. Salgado, K. Grafenstein, **A. Golub**, A. Döpp, A. Eckey, D. Hollatz, C. Müller, A. Seidel, D. Seipt, S. Karsch, M.Zepf, *Towards pair production in the non-perturbative regime*. New J. Phys. **23**, 105002 (2021).

In this reference, the intended setup and technics for observation of Breit-Wheeler pairs in the high intensity regime envisaged by the collaboration FOR 2783 is described. My contribution to this publication consists of the involvement in the preparation of Secs. 2.1. and 4, where a theoretical description of pair creation in a pulsed plane wave and estimated number of produced particles were provided.

5. **A. Golub**, S. Villalba-Chávez and C. Müller, *Nonlinear Breit-Wheeler pair production in collisions of bremsstrahlung γ quanta and a tightly focused laser pulse*. Phys. Rev. D **105**, 116016 (2022).

This project deepens the theoretical insights of the former reference. Here, an estimation of the created Breit-Wheeler pairs in the strongly nonlinear nonperturbative regime is provided with particular attention on implication of the focused field profiles. Thus, the impact of transverse and longitudinal laser focusing could be elucidated. The corresponding analytical and numerical calculations as well as the associated figures and the preparation of the manuscript were performed by me.

Not included in the present thesis, but mentioned for completeness is the following article:

6. S. Villalba-Chávez, **A. Golub** and C. Müller *Axion-modified photon propagator, Coulomb potential, and Lamb shift*. Phys. Rev. D **98**, 115008 (2018).

Contents

Chapter 1

Introduction

Breit-Wheeler pair production, a reaction describing the creation of an electron-positron pair resulting from a collision of two or more photons from sources γ and γ', represents one of the most fundamental processes of quantum electrodynamics (QED). It allows for a striking possibility of matter creation purely from light, in accordance with Einstein's equivalence between mass and energy. Firstly described by G. Breit and J. A. Wheeler [1] in 1934, it can be presented symbolically as

$$n\gamma + \gamma' \to e^- + e^+, \tag{1.1}$$

where n stands for the number of participating γ photons. Thus, one distinguishes between a linear two-photon process when $n = 1$ and a nonlinear pair creation otherwise. The latter case was studied thoroughly by theoreticians in the 1960s and 1970s [2, 3, 4, 5] in configurations, where a quantised photon γ' impinges on an electromagnetic field of monochromatic plane wave or a constant field with equal electric and magnetic components. In the course of these studies, the focus was put on the different regimes of the particle production depending on the intensity parameter[1] $\xi = |e|\mathcal{E}_0/(m\omega)$ with the electron charge e and mass m, as well as the plane-wave field amplitude $\mathcal{E}_0$ and frequency ω. For $\xi \ll 1$ the process takes place in a perturbative weak field regime, where the pair creation rate is ruled by the absorption of a distinct small number of photons and is suppressed with growing n: $R \propto \xi^{2n}$. Conversely, for $\xi \gg 1$ one enters the nonperturbative strong field regime with the characteristic Schwinger-like behaviour $R \propto \mathrm{e}^{-8/(3\kappa)}$, where $\kappa = 2\omega'\mathcal{E}_0/(mE_c) \ll 1$ is the quantum nonlinearity parameter for the counterpropagating geometry of the corresponding fields and $E_c = m^2/|e| \approx 1.3 \times 10^{16}$ V/cm stands for the critical Schwinger field strength. In this parameter range a perturbative expansion in ξ is no longer possible and exact consideration is in order. A short summary of these findings, as they represent a starting point for the studies presented in this thesis, is discussed in chapter 3.

[1] Throughout this thesis and unless stated otherwise a natural unit system, where $c = \hbar = \epsilon_0 = 1$ with the speed of light c, the Planck's constant h divided over 2π and dielectric permittivity of vacuum ϵ_0, is employed. Moreover, a metric with the signature $\mathrm{diag}(g^{\mu\nu}) = (1, -1, -1, -1)$ and four-derivative $\partial^\mu = (\frac{\partial}{\partial t}, -\boldsymbol{\nabla})$ is used.

Regardless of the high interest from the theoretical point of view, experimental verification of the Breit-Wheeler process has been so far accomplished solely in the nonlinear multiphoton ($\xi \lesssim 1$) regime in an experiment conducted at the Stanford Linear Accelerator Center (SLAC) [6, 7]. The latter took place via two steps: Firstly, multi-GeV energy photons were generated via an interaction between a 46.6 GeV electron beam with an optical terawatt laser pulse of several eV frequency. Secondly, the backscattered photons reacted with the laser field creating Breit-Wheeler pairs and allowing for detection of about 100 created positrons during the entire experiment. In general, the main obstacle for observation of this process is dictated by the high energy required for the reaction to take place. Hence, in the described SLAC setup at least five laser photons were needed (when the laser-dressing is taken into account) in the second reaction step [8, 9].

The energy threshold lies even higher for the experimental verification of the linear Breit-Wheeler pair creation demanding $\omega\omega' \geq 2m^2$ for counterpropagating photon sources. Thus, a first observation of this channel has recently succeeded in collisions of quasireal photons produced by acceleration of gold ions to ultra-relativistic energies [10]. In addition, several theoretical proposals for experimental validation of the linear process involving real photons were put forward: there are studied designs combining thermal hohlraum radiation with plane-wave electromagnetic field [11] or photons produced from bremsstrahlung in a high-Z target [12]. Alternatively, incorporation of two Compton gamma sources [13], laser pulses interacting with thin aluminium targets or dense, short gas jets [14] and multi-PW laser beams penetrating through narrow tube targets [15] were pursued. Moreover, an experimental setup put forward at the Rutherford Appleton Laboratory is aiming to detect the two-photon Breit-Wheeler process in interactions of MeV bremsstrahlung photons with an x-ray laser [16].

Additionally, also the high intensity regime of the Breit-Wheeler pair production with $\xi \gg 1$ has eluded experimental detection so far. However, the complication here is represented by the requirement of extremely high effective field strength $(\omega'/m)\mathcal{E}_0$, which has to come close to the Schwinger scale. Consequently, solely with the recent development in the laser and accelerator facilities a step towards the detection of strong field Breit-Wheeler pairs can be taken (see Refs. [17, 18, 19, 20, 21] and references therein). Therefore, vast theoretical effort has been put on the realistic modelling of the involved laser field as the needed high intensity can be currently reached only in tightly focused, short laser pulses (see e.g. Refs. [22, 23, 24, 25, 26, 27, 28, 29, 30, 31, 32]).

In this context, the present thesis addresses theoretically the questions of Breit-Wheeler pair creation in different regimes and scenarios. To that end, after a presentation of general aspects of QED and a review on the pair production in a plane wave, which are exposed in chapters 2 and 3, correspondingly, chapter 4 is dedicated to the considerations of linear and strong field Breit-Wheeler reactions. Thus, in section 4.2 a possibility for observation of the two-photon process involving a bremsstrahlung photon impinging on an x-ray laser pulse is elucidated and the case of bremsstrahlung interaction with an optical laser is discussed in section 4.3. In the

latter, special attention is paid to the incorporation of the laser focusing and study of its impact on the pair production. These investigations are performed with regard to the planned experiment at the Center of Advanced Laser Applications (CALA), where an observation of the Breit-Wheeler pair creation in the highly nonlinear nonperturbative $\xi \gg 1$, $\kappa \approx 1$ regime for the first time is aimed [33].

Next, in chapter 5 the theory of quantum electrodynamics in 2+1 spacetime dimensions is introduced and applied to the Breit-Wheeler pair creation. Thus, the effect of lowering the spacial dimensionality is studied and striking differences to the ordinary QED are shown: In 2+1 dimensional spacetime, when an even number of strong field photons takes part in the particle production, the rate shows a nonvanishing behaviour at the energy threshold, where created particles possess zero momentum. In order to deepen the understanding of the found discrepancy and apply the results of this rather abstract chapter on a real physical system, the Breit-Wheeler pair creation in bandgapped graphene is considered in chapter 6.

Graphene monolayers with a gap between the valence and conduction bands represent a sophisticated theoretical (and experimental) laboratory for observation of Breit-Wheeler processes as valence electrons in this material when excited create a quasiparticle-hole pair. The time evolution of the quasiparticle and hole in the vicinity of the Fermi surface can be described by a relativistic Dirac-like equation in 2+1 spacetime dimensions. When irradiating the graphene sheet with two light sources, the analogues of Breit-Wheeler process take place. In subsections 6.2.1 and 6.2.2 of this thesis the two- and three-photon quasipair creation is studied. The calculation describing the linear Breit-Wheeler reaction in bandgapped graphene represents an alternative to the approach in section 4.2 which requires much lower energy. Additionally, the study of the three-photon reaction is distinguished by the non-zero threshold behaviour predicted in chapter 5 and providing this way a path for an experimental observation of the results in the lower dimensional Minkowski spacetime. Finally, the conclusions are provided in the last chapter, whereas some technical details are displayed in appendices.

Chapter 2

Theoretical framework of QED

The interaction of electrons, positrons and photons is described by the fundamental theory of QED. The basic quantity from which all observables can be derived, is the corresponding action. It reads [34]

$$S[a,\psi,\bar{\psi}] = \int d^4x \left(\bar{\psi}(x) \left(i\not{D} - m \right) \psi(x) - \frac{1}{2\zeta} \left(\partial_\mu a^\mu(x) \right)^2 - \frac{1}{4} f_{\mu\nu}(x) f^{\mu\nu}(x) \right), \tag{2.1}$$

where the Feynman notation $\not{D} = \gamma_\mu D^\mu$ with $4 \times 4-$dimensional Dirac $\gamma-$matrices (see appendix A.1.1 for further details) and Dirac adjoint $\bar{\psi} = \psi^\dagger \gamma^0$ of a four-dimensional bispinor fermion field ψ are introduced. Moreover, m and e, $e < 0$, denote the electron mass and charge, correspondingly, and $D^\mu = \partial^\mu + iea^\mu$ stands for the covariant derivative. The electromagnetic sector is represented by $U(1)$ gauge field a^μ and the electromagnetic field tensor $f^{\mu\nu}$. Here, ζ stands for the gauge fixing parameter and it allows for the canonical quantisation of the electromagnetic field in a Lorentz covariant way. Hence, from Eq. (2.1) we read off the fermionic, photonic and interaction Lagrangian densities

$$\begin{aligned} \mathcal{L}_f(x) &= \bar{\psi}(x) \left(i\not{\partial} - m \right) \psi(x), \\ \mathcal{L}_\gamma(x) &= -\frac{1}{2\zeta} \left(\partial_\mu a^\mu(x) \right)^2 - \frac{1}{4} f_{\mu\nu}(x) f^{\mu\nu}(x), \\ \mathcal{L}_{\text{int}}(x) &= -e\bar{\psi}(x) \not{a}(x) \psi(x), \end{aligned} \tag{2.2}$$

which are the starting points for description of the free photon and fermionic fields as well as their interaction.

2.1 Interaction

In the interaction representation of QED, the interplay between particles is described via scattering matrix (S-matrix) elements of the form

$$\langle out | \hat{S}[\hat{\psi}, \hat{\bar{\psi}}, \hat{a}] | in \rangle \tag{2.3}$$

with the scattering operator

$$\hat{S}[\hat{\psi},\hat{\bar{\psi}},\hat{a}] = \mathcal{T}\left[\mathrm{e}^{i\int d^4x\hat{\mathcal{L}}_{\mathrm{int}}}\right], \tag{2.4}$$

where $\mathcal{T}[...]$ stands for the time ordering operator and $\hat{\psi},\hat{\bar{\psi}},\hat{a}$ denote quantised fermion and photon field operators, correspondingly. Since the coupling between electrons and positrons with electromagnetic field is dictated by the fine-structure constant $\alpha = |e|^2/(4\pi) \approx 1/137 \ll 1$, perturbation theory can be applied[1]. In the present thesis, the expansion of the scattering operator up to the third order is of interest

$$\hat{S}[\hat{\psi},\hat{\bar{\psi}},\hat{a}] \approx 1 + \hat{S}^{(1)}[\hat{\psi},\hat{\bar{\psi}},\hat{a}] + \hat{S}^{(2)}[\hat{\psi},\hat{\bar{\psi}},\hat{a}] + \hat{S}^{(3)}[\hat{\psi},\hat{\bar{\psi}},\hat{a}] + \mathcal{O}\left(e^4\right), \tag{2.5}$$

where

$$\begin{aligned}
\hat{S}^{(1)}[\hat{\psi},\hat{\bar{\psi}},\hat{a}] &= -ie\mathcal{T}\left[\int d^4x\ \hat{\bar{\psi}}(x)\hat{\not{a}}(x)\hat{\psi}(x)\right],\\
\hat{S}^{(2)}[\hat{\psi},\hat{\bar{\psi}},\hat{a}] &= \frac{i^2e^2}{2!}\mathcal{T}\left[\int d^4x\int d^4y\ \hat{\bar{\psi}}(x)\hat{\not{a}}(x)\hat{\psi}(x)\hat{\bar{\psi}}(y)\hat{\not{a}}(y)\hat{\psi}(y)\right],\\
\hat{S}^{(3)}[\hat{\psi},\hat{\bar{\psi}},\hat{a}] &= -\frac{i^3e^3}{3!}\mathcal{T}\left[\int d^4x\int d^4y\int d^4z\ \hat{\bar{\psi}}(x)\hat{\not{a}}(x)\hat{\psi}(x)\hat{\bar{\psi}}(y)\hat{\not{a}}(y)\hat{\psi}(y)\hat{\bar{\psi}}(z)\hat{\not{a}}(z)\hat{\psi}(z)\right].
\end{aligned} \tag{2.6}$$

The states $|in\rangle$ and $|out\rangle$ represent the asymptotic states of the system at $t\to-\infty$ and $t\to\infty$, respectively, when no interaction is present.

2.2 Radiation sector

2.2.1 Quantised radiation field and number states

When setting the gauge fixing parameter $\zeta = 1$ (so-called Feynman gauge) and carrying out the quantisation of the gauge field within Gupta-Bleuler formalism [35, 36], the quantised electromagnetic field reads

$$\hat{a}_\mu(x) = \hat{a}^+_\mu(x) + \hat{a}^-_\mu(x) = \sum_{\lambda,k}\frac{1}{\sqrt{2\omega V_\gamma}}\left(\epsilon_{\mu,\lambda}\hat{a}_{k,\lambda}\mathrm{e}^{-ikx} + \epsilon^*_{\mu,\lambda}\hat{a}^\dagger_{k,\lambda}\mathrm{e}^{ikx}\right) \tag{2.7}$$

with the normalisation volume V_γ, four-momentum $k=(\omega,\boldsymbol{k})$, $k^2=0$, polarisation vectors $\epsilon_{\mu,\lambda}$ and creation and annihilation operators $\hat{a}^{(\dagger)}_{k,\lambda}$ obeying the canonical equal time commutation relations

$$[\hat{a}_{k,\lambda},\hat{a}^\dagger_{k',\lambda'}] = -g_{\lambda\lambda'}\delta_{\boldsymbol{k},\boldsymbol{k}'} \tag{2.8}$$

[1] Later on it will be shown that this condition needs to be modified in strong fields.

and zero otherwise. In general, there exist four polarisation vectors with $\lambda = 0, ...3$. Here, however, only two physical degrees of freedom for transversal polarisation will be taken into account with $\lambda = 1, 2$ (for further details see Refs. [35, 36]) and $\epsilon^{\mu}_{\lambda}\epsilon_{\mu,\lambda'} = -\delta_{\lambda\lambda'}$. Thus, the orthogonality condition $\epsilon k = 0$ and the completeness relation

$$\sum_{\lambda=1,2} \epsilon^{\mu}_{\lambda}\epsilon^{\nu}_{\lambda} = -g^{\mu\nu} - \frac{k^{\mu}k^{\nu} - nk(k^{\mu}n^{\nu} + k^{\nu}n^{\mu})}{(nk)^2} \tag{2.9}$$

with $n^{\mu} = (1, 0, 0, 0)$ hold. Lastly, quantisation of the field requires introduction of the vacuum state of minimal energy $|0\rangle$ with $\hat{a}_{k,\lambda}|0\rangle = 0$ and $\langle 0|0\rangle = 1$, while the quantised field itself describes quantum fluctuations around it. In general, a quantum state with well defined number of photons $n_{k,\lambda}$ is represented by a Fock number state

$$|n_{k,\lambda}\rangle = \frac{(\hat{a}^{\dagger}_{k,\lambda})^{n_{k,\lambda}}}{\sqrt{n_{k,\lambda}!}}|0\rangle. \tag{2.10}$$

2.2.2 Classical fields and coherent states

In this thesis the main source of photons is a laser, which produces coherent light and, thus, can be most accurately described by a coherent state $|\alpha_k\rangle$ in a mode k with normalisation $\langle\alpha_k|\alpha_k\rangle = 1$ [37, 38]

$$|\alpha_k\rangle = \mathrm{e}^{-\frac{1}{2}|\alpha_k|^2} \sum_{n_{k,\lambda}=0}^{\infty} \frac{\alpha^{n_{k,\lambda}}}{\sqrt{n_{k,\lambda}!}}|n_{k,\lambda}\rangle = \hat{D}(\alpha_k)|0\rangle, \tag{2.11}$$

where α_k is a complex number and $\hat{D}(\alpha_k)$ is a unitary displacement operator. Following Ref. [39], a relation

$$\hat{D}^{-1}(\alpha_k)\hat{a}_{\mu}(x)\hat{D}(\alpha_k) = \mathcal{A}_{\mu}(x) + \hat{a}_{\mu}(x) \tag{2.12}$$

holds. Here, $\mathcal{A}_{\mu}(x)$ stands for an "external" classical electromagnetic field potential describing the laser.

When the number of laser photons that participate in the pair creation is small compared to the total photon number in the laser field (which will be the case for the present thesis, for further details see Refs. [40, 41, 42]), the depletion effects of the laser may be ignored. In such a scenario the same coherent state would be present in both final and initial states of the S-matrix element. Then, a transition

$$\langle\alpha_k, n|\hat{S}[\hat{\psi}, \hat{\bar{\psi}}, \hat{a}]|\alpha_k, n\rangle \to \langle n|\hat{S}[\hat{\psi}, \hat{\bar{\psi}}, \hat{a} + \mathcal{A}]|n\rangle \tag{2.13}$$

is allowed to be made, where $|n\rangle$ denotes the Fock number state of charged particles involved in the process. Thus, the interaction with the laser is incorporated by the classical field and the S-matrix elements can be calculated as usual with number states.

2.3 Fermionic sector

From the first line in Eq. (2.2) an equation of motion for free Dirac fermions can be derived

$$(i\partial\!\!\!/ - m)\psi(x) = 0, \tag{2.14}$$

which is solved by a four-component spinor $\psi(x)$ invariant under $Sl(2,\mathbb{C})$ transformation [34]. For an electron, the latter reads

$$\psi_{p,s}(x) = \sqrt{\frac{m}{p_0 V}} u_{p,s} \mathrm{e}^{-ipx} \tag{2.15}$$

with a spinor $u_{p,s}$ and when normalised to one particle in a normalisation volume V. This condition is equivalent to setting the $0-$th component of the current $j^\mu = \bar{\psi}_{p,s}\gamma^\mu\psi_{p,s}$ to $\langle j^0\rangle = 1/V$. Moreover, a solution for an antiparticle (positron) is obtained from $\psi_{p,s}(x)$ when substituting $p \to -p$ and $u_{p,s} \to v_{p,s}$. Further details on spinors $u_{p,s}$ and $v_{p,s}$ are presented in appendix A.2.1.

When quantised, the plane-wave expansions of the fermionic field operators result

$$\begin{aligned}
\hat{\psi}(x) &= \sum_{p,s} \sqrt{\frac{m}{p_0 V}} \left(u_{p,s}\hat{b}_{p,s}\mathrm{e}^{-ipx} + v_{p,s}\hat{d}^\dagger_{p,s}\mathrm{e}^{ipx} \right), \\
\hat{\bar{\psi}}(x) &= \sum_{p,s} \sqrt{\frac{m}{p_0 V}} \left(\bar{v}_{p,s}\hat{d}_{p,s}\mathrm{e}^{-ipx} + \bar{u}_{p,s}\hat{b}^\dagger_{p,s}\mathrm{e}^{ipx} \right)
\end{aligned} \tag{2.16}$$

with the nonvanishing equal time anticommutation relations for particle and antiparticle creation and annihilation operators

$$\{\hat{b}_{p,s}, \hat{b}^\dagger_{p',s'}\} = \{\hat{d}_{p,s}, \hat{d}^\dagger_{p',s'}\} = \delta_{s,s'}\delta_{\boldsymbol{p},\boldsymbol{p}'} \tag{2.17}$$

and zero otherwise. Lastly, the fermionic Fock number states are defined as

$$|n_{p^-,s^-}\rangle = \frac{(\hat{b}^\dagger_{p^-,s^-})^{n_{p^-,s^-}}}{\sqrt{n_{p^-,s^-}!}}|0\rangle, \quad |n_{p^+,s^+}\rangle = \frac{(\hat{d}^\dagger_{p^+,s^+})^{n_{p^+,s^+}}}{\sqrt{n_{p^+,s^+}!}}|0\rangle \tag{2.18}$$

for electron and positron, correspondingly, with the fermion vacuum $|0\rangle$ satisfying $\hat{b}_{p^-,s^-}|0\rangle = \hat{d}_{p^+,s^+}|0\rangle = 0$. Moreover, the fermionic Feynman propagator

$$S_F(x-y) = \langle 0|\mathcal{T}\left[\hat{\psi}(x)\hat{\bar{\psi}}(y)\right]|0\rangle \tag{2.19}$$

in its Fourier representation reads

$$S_F(x-y) = \int \frac{d^4p}{(2\pi)^4} \frac{i\mathrm{e}^{-ip(x-y)}}{p\!\!\!/ - m + i0^+}. \tag{2.20}$$

2.4 QED in strong laser fields

2.4.1 Furry picture

When only few photons participate in the process, the corresponding electromagnetic field is considered to be weak and the perturbation theory may be applied. However, in the case of strong fields, where a large number of photons is involved, an alternative treatment is in order. To that end, a transition to the special case of interaction picture, which is called Furry picture [39, 43], is made, where the interaction of charged particles with the strong field is taken into account exactly[2]. This is done by dividing the gauge field in Eq. (2.1) into perturbative weak field $a_\mu(x)$, which is further quantised, and strong background field $\mathcal{A}_\mu(x)$, which is treated classically and absorbed in the fermionic Lagrangian density. Thus, the single particle states related to fermions follow from solutions of Dirac equation in external electromagnetic field and incorporate the interaction with background field in full glory.

Of special interest for this thesis is a plane-wave external field $\mathcal{A}_\mu(\phi)$, which depends on coordinates only through a phase $\phi = kx$ with k denoting the field wave vector. Since the Dirac equation for this field configuration can be solved analytically (see next section), the Fock space for the resulting field dressed states can be constructed and the scattering operator reads

$$\hat{S}[\hat{\Psi}, \hat{\bar{\Psi}}, \hat{a}] = \mathcal{T}\left[\mathrm{e}^{-ie\int d^4x \hat{\bar{\Psi}}(x)\hat{\not{a}}(x)\hat{\Psi}(x)}\right], \tag{2.21}$$

where $\hat{\Psi}(x)$ stands for the fermionic field operator in Furry picture, which can be expanded in dressed Volkov states, as discussed below.

2.4.2 Volkov states

Volkov states, which are also called dressed states, are the solutions of the Dirac equation in a classical plane-wave electromagnetic field $\mathcal{A}_\mu(\phi)$ with a phase $\phi = kx$ in a Lorentz gauge ($\partial^\mu \mathcal{A}_\mu = 0$)

$$(i\not{\partial} - e\not{\mathcal{A}} - m)\Psi = 0. \tag{2.22}$$

When exploiting an ansatz $\Psi_{p,s}(x) = NF_p(\phi)u_{p,s}\mathrm{e}^{-ipx}$ [2, 44, 45], where $F_p(\phi)$ represents the modification in the solution caused by the gauge field and converges to $F_p(\phi)u_{p,s} \to u_{p,s}$ for $\mathcal{A}_\mu(\phi) = 0$, one obtains an electron solution

$$\Psi_{p,s}(x) = N(1 + \frac{e}{2kp}\not{k}\not{\mathcal{A}}(\phi))u_{p,s}\mathrm{e}^{iS_p(x)} \tag{2.23}$$

[2]The wave functions in interaction representation and Furry picture are related by a canonical transformation.

with the classical action

$$S_p(x) = -px - \int_0^\phi d\varphi \left(\frac{ep\mathcal{A}(\varphi)}{kp} - \frac{e^2\mathcal{A}^2(\varphi)}{2kp} \right) \tag{2.24}$$

in the exponent. For the derivation of Eq. (2.23) the following relation was employed

$$f_{\mu\nu} = k_\mu \frac{d\mathcal{A}_\nu(\phi)}{d\phi} - k_\nu \frac{d\mathcal{A}_\mu(\phi)}{d\phi}. \tag{2.25}$$

In order to obtain a Volkov solution for a positron one substitutes $p \to -p$ and the spinor $u_{p,s}$ through $v_{p,s}$ (see Eq.(A.4)). Furthermore, the normalization constant N is set similarly to the case of free fermions demanding $\langle j^0 \rangle = \langle \bar{\Psi}_{p,s} \gamma^0 \Psi_{p,s} \rangle = 1/V$, which implies $N = \sqrt{\frac{m}{q^0 V}}$. Here, q^0 stands for the $0-$th component of the effective particle momentum in the electromagnetic field, which is defined as a phase averaged kinetic momentum

$$q^\mu = p^\mu - e\langle \mathcal{A}^\mu \rangle + \left(e\frac{p\langle \mathcal{A} \rangle}{kp} - e^2 \frac{\langle \mathcal{A}^2 \rangle}{2kp} \right) k^\mu \tag{2.26}$$

with effective squared mass $q^2 = m^{*2} = m^2(1 + e^2\langle \mathcal{A} \rangle^2/m^2 - e^2\langle \mathcal{A}^2 \rangle/m^2)$.

Since the vacuum in the presence of a plane-wave field is stable, i.e. no creation of electron-positron pairs via the Schwinger mechanism occurs [46], the quantisation of fermionic fields is done similarly to the case of free fermions and the field operators in the dressed state expansion read[3]

$$\hat{\Psi}(x) = \sum_{p,s} \sqrt{\frac{m}{q_0 V}} \left(\left[1 + \frac{e}{2kp} \not{k} \not{\mathcal{A}}(\phi) \right] u_{p,s} \mathrm{e}^{iS_p(x)} \hat{b}_{p,s} \right. \\ \left. + \left[1 - \frac{e}{2kp} \not{k} \not{\mathcal{A}}(\phi) \right] v_{p,s} \mathrm{e}^{iS_{-p}(x)} \hat{d}^\dagger_{p,s} \right), \tag{2.27}$$

$$\hat{\bar{\Psi}}(x) = \sum_{p,s} \sqrt{\frac{m}{q_0 V}} \left(\bar{u}_{p,s} \left[1 + \frac{e}{2kp} \not{\mathcal{A}}(\phi) \not{k} \right] \mathrm{e}^{-iS_p(x)} \hat{b}^\dagger_{p,s} \right. \\ \left. + \bar{v}_{p,s} \left[1 - \frac{e}{2kp} \not{\mathcal{A}}(\phi) \not{k} \right] \mathrm{e}^{-iS_{-p}(x)} \hat{d}_{p,s} \right). \tag{2.28}$$

In the next section a linearly polarised plane-wave potential of the form $\mathcal{A}^\mu(\phi) = \mathfrak{a}_0 \epsilon^\mu \cos(kx)$ with a maximal amplitude $\mathfrak{a}_0$ and polarisation ϵ^μ is incorporated. In

[3] It can be shown that Volkov states form a complete orthogonal basis of the solutions to Eq. (2.22) (for proof of completeness see e.g. Refs. [47, 48] and Refs. [3, 49] for orthogonality).

such a scenario Volkov solutions for an electron and a positron read correspondingly

$$\Psi_{q_-,s_-} = \sqrt{\frac{m}{q_-^0 V}}(1 + \frac{e}{2kq_-}\not{k}\not{\mathcal{A}})u_{p_-,s_-}\mathrm{e}^{-iq_-x - i\frac{e\mathfrak{a}_0 q_-\epsilon}{kq_-}\sin(kx) - i\frac{e^2\mathfrak{a}_0^2}{8kq_-}\sin(2kx)}, \tag{2.29}$$

$$\Psi_{q_+,s_+} = \sqrt{\frac{m}{q_+^0 V}}(1 - \frac{e}{2kq_+}\not{k}\not{\mathcal{A}})v_{p_+,s_+}\mathrm{e}^{iq_+x - i\frac{e\mathfrak{a}_0 q_+\epsilon}{kq_+}\sin(kx) + i\frac{e^2\mathfrak{a}_0^2}{8kq_+}\sin(2kx)}. \tag{2.30}$$

Here, the effective momentum and mass can be simplified to

$$q_\mp^\mu = p_\mp^\mu + \frac{e^2\mathfrak{a}_0^2}{4kq_\mp}k^\mu, \quad m^{*2} = m^2\left(1 + \frac{e^2\mathfrak{a}_0^2}{2m^2}\right) \tag{2.31}$$

and $kp_\mp = kq_\mp$ holds. In line, the field operators need to be adjusted accordingly.

Chapter 3

Breit-Wheeler pair creation in monochromatic plane wave

In this section the Breit-Wheeler pair creation process in a linearly polarised plane-wave electromagnetic field $\mathcal{A}^\mu = \epsilon^\mu \mathfrak{a}_\mathfrak{o} \cos(kx)$ with polarisation ϵ^μ and wave vector $k = (\omega, \boldsymbol{k})$ is considered[1]. Here, an electron and a positron with momenta and spin $p^\pm, s^\pm$ are created when a photon with a wave vector k' and polarisation ϵ', which originates from a weak electromagnetic field that is seen as a perturbation, interacts with a strong field $\mathcal{A}^\mu$. In such a scenario, the only nonvanishing contribution to the transition amplitude stems from the first order scattering operator in the Furry picture $\hat{S}[\hat{\Psi}, \hat{\bar{\Psi}}, \hat{a}]$ (see Eq. (2.21))

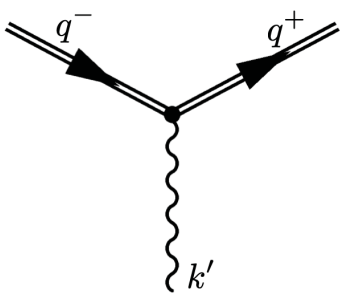

Figure 3.1: Feynman diagram of Breit-Wheeler pair creation in a monochromatic plane-wave field.

$$S_{fi} = \langle 1_{p^+,s^+}; 1_{p^-,s^-} | \hat{S}^{(1)}[\hat{\Psi}, \hat{\bar{\Psi}}, \hat{a}] | 1_{k',\epsilon'} \rangle. \tag{3.1}$$

Observe that the interaction with the monochromatic plane wave is accounted for in full glory by the fermion field operators which contain Volkov solutions introduced in Sec. 2.4.2. The corresponding Feynman diagram is depicted in Fig. 3.1, where a wavy line indicates a quantised photon and double lines represent dressed states for electron and positron. Next, when employing the anticommutation relations for fermions and commutation relations for the photonic creation and annihilation operators the transition amplitude reads

$$S_{fi} = -ie \sqrt{\frac{1}{2\omega' V_\gamma}} \int d^4x \bar{\Psi}_{q^-,s^-}(x) \not{\epsilon}' \mathrm{e}^{-ik'x} \Psi_{q^+,s^+}(x). \tag{3.2}$$

[1] This subject war thoroughly investigated in Refs. [2, 3, 4], by which the presentation of this section is guided.

After inserting the Volkov solutions from section 2.4.2 into the equation above and using the identities with $\gamma-$matrices displayed in appendix A.1.1 as well as the transversal condition $\epsilon k = 0$, S_{fi} results to

$$S_{fi} = -ie\sqrt{\frac{1}{2\omega' V_\gamma}\frac{m^2}{q_0^+ q_0^- V^2}}\int d^4x \bar{u}_{p^-,s^-} M v_{p^+,s^+} \mathrm{e}^{-i(k'-q_+-q_-)x - iz_-\sin(kx) - iz_+\sin(2kx)} \tag{3.3}$$

with a matrix

$$M = \not{\epsilon}' + \frac{e\mathfrak{a}_0}{2}\left(\frac{\not{\epsilon}\not{k}\not{\epsilon}'}{kp_-} - \frac{\not{\epsilon}'\not{k}\not{\epsilon}}{kp_+}\right)\cos(kx) - \frac{e^2\mathfrak{a}_0^2}{2kp_-kp_+}\not{k}\epsilon'^\mu k_\mu \cos^2(kx) \tag{3.4}$$

and arguments $z_- = e\mathfrak{a}_0(\frac{q^+\epsilon}{q^+k} - \frac{q^-\epsilon}{q^-k})$, $z_+ = -\frac{e^2\mathfrak{a}_0^2}{8}\frac{kk'}{kq^+kq^-}$ in the exponential function. In order to solve the integral in Eq. (3.3), the generalised Bessel function $\tilde{J}_n(z_-, z_+)$ and $\tilde{\mathcal{J}}_n^1$, $\tilde{\mathcal{J}}_n^2$ are introduced in Eqs. (B.5) and (B.6) (see appendix B), correspondingly. Following these definitions Eq. (3.3) can be simplified to

$$S_{fi} = -ie\sqrt{\frac{1}{2\omega' V_\gamma}\frac{m^2}{q_0^+ q_0^- V^2}}\sum_{n=-\infty}^{\infty}(2\pi)^4\delta^4(nk + k' - q^+ - q^-)\bar{u}_{p^-} M_n v_{p^+}, \tag{3.5}$$

where the delta function encodes the law of energy-momentum conservation in the process and M_n is of the following form

$$M_n = \not{\epsilon}'\tilde{J}_n(z_-, z_+) + \frac{e\mathfrak{a}_0}{2}\tilde{\mathcal{J}}_n^1\Big(\frac{\not{\epsilon}\not{k}\not{\epsilon}'}{kq^-} - \frac{\not{\epsilon}'\not{k}\not{\epsilon}}{kq^+}\Big) - \frac{e^2\mathfrak{a}_0^2}{2kq^+kq^-}\epsilon'^\mu k_\mu \tilde{\mathcal{J}}_n^2 \not{k}. \tag{3.6}$$

Notice that the matrix above is dependent on the relative directions of field polarisations ϵ, ϵ' and wave vector k. Here, two polarisation options of the weak field will be considered: the case, where weak and strong fields are parallelly polarised (i.e. propagate in one plane) and a case with unpolarised incident photon.

The quantity of primary interest in this thesis is the differential rate of pair creation per volume, which is defined as

$$dR = \frac{|S_{fi}|^2}{TV}V^2\frac{d^3q^-}{(2\pi)^3}\frac{d^3q^+}{(2\pi)^3}. \tag{3.7}$$

Since $d^3p^-d^3p^+/p_0^-p_0^+ = d^3q^-d^3q^+/q_0^-q_0^+$ holds, the phase space in the expression above is written in terms of the effective particle momenta q^+, q^- in order to be consistent with the normalisation in Eqs. (2.29), (2.30). When inserting the squared transition amplitude into the equation above one ends up with

$$dR = \frac{e^2m^2}{8\pi^2\omega' V_\gamma}\sum_{n=-\infty}^{\infty}|\bar{u}_{p^-} M_n v_{p^+}|^2\delta^4(nk + k' - q^+ - q^-)\frac{d^3q^-}{q_0^-}\frac{d^3q^+}{q_0^+}, \tag{3.8}$$

where the sum over n can be interpreted as a sum over a number of absorbed

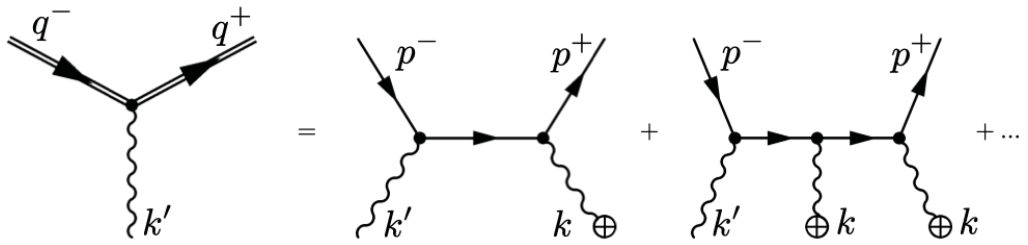

Figure 3.2: Feynman diagram depicting Breit-Wheeler pair creation in strong field as an infinite sum of tree level contributions, where wavy lines with crosses stand for absorbed field photons.

photons from the classical field $\mathcal{A}^\mu(kx)$. Here, positive indices stand for photon absorption, whereas negative n denote emission. As it will be seen later on, the energy-momentum balance of the process will rule out negative contributions. Thus, the interaction with the strong field is considered in full glory. The corresponding Feynman diagram is shown in Fig. 3.2, where double lines stand for dressed states, single lines denote free fermions and wavy lines represent perturbative and strong field photons. The latter are marked with cross.

Firstly, the case of an unpolarised incident photon is considered. In such a scenario the square of the amplitude is obtained by averaging over possible photon polarisations[2] $\epsilon'_{\lambda'}$ and summing over lepton spins $s^\pm$, i.e. $|\overline{\mathcal{M}}_n|^2 = \frac{1}{2}\sum_{\lambda',s^\pm} |\bar{u}_{p^-} M_n v_{p^+}|^2$, and can be written as

$$|\overline{\mathcal{M}}_n|^2 = \frac{1}{2}\sum_{\lambda'} \mathrm{Tr}\left[\frac{\not{p}^- + m}{2m} M_n \frac{\not{p}^+ - m}{2m} \bar{M}_n\right] \tag{3.9}$$

with $\bar{M}_n = \gamma^0 M_n^\dagger \gamma^0$. The sum over polarisations is managed with help of the completeness relation in Eq. (2.9). It is worth emphasising that, owing to the Ward identity, only the term containing $-g^{\mu\nu}$ will contribute to the squared amplitude. Exploiting the completeness relation as well as the energy-momentum balance and transversal condition ($k\epsilon = 0$) provides

$$|\overline{\mathcal{M}}_n|^2 = \tilde{J}_n^2(z_-, z_+) - \frac{e^2\mathfrak{a}_0^2}{m^2}\left(1 - \frac{(kk')^2}{2kq^+kq^-}\right)\left[(\tilde{\mathcal{J}}_n^1)^2 - \tilde{J}_n(z_-, z_+)\tilde{\mathcal{J}}_n^2\right]. \tag{3.10}$$

Additionally, when deriving the equation above the following relation between generalised Bessel functions [2, 50]

$$(n + 2z_+)\tilde{J}_n(z_-, z_+) - z_-\tilde{\mathcal{J}}_n^1 - 4z_+\tilde{\mathcal{J}}_n^2 = 0 \tag{3.11}$$

has been used. Next, a particular polarisation of the incident photon is considered:

[2]Here, the considered transverse polarisations $\epsilon'_{\lambda'}$ are $\epsilon'_\parallel$ and $\epsilon'_\perp$ with the subscripts $\parallel, \perp$ denoting the parallel and perpendicular polarisations of the quantised photon, respectively, when compared to the polarisation of the strong field.

$\epsilon' = \epsilon'_{\parallel} = \epsilon$. Hence, the term proportional to $\cos^2(kx)$ in Eq. (3.6) will no longer contribute and when using enenrgy-momentum conservation, transversality condition and Eq. (3.11) the squared amplitude reads

$$|\mathcal{M}^{\parallel}{}_n|^2 = \frac{1}{2}\mathrm{Tr}\left[\frac{\not{p}^- + m}{2m} M_n \frac{\not{p}^+ - m}{2m} \bar{M}_n\right] = \sigma \tilde{J}_n^2(z_-, z_+) - \frac{e^2\mathfrak{a}_0^2}{m^2}\left(1 - \frac{(kk')^2}{4kq^+kq^-}\right)\left[(\tilde{\mathcal{J}}_n^1)^2 - \tilde{J}_n(z_-, z_+)\tilde{\mathcal{J}}_n^2\right] \quad (3.12)$$

with $\sigma = -\frac{e^2\mathfrak{a}_0^2}{m^2}\left(\frac{z_-^2}{64z_+^2} + \frac{1}{2} + \frac{n}{4z_+}\right)$. Moreover, since $|\overline{\mathcal{M}}_n|^2 = \left(|\mathcal{M}^{\parallel}{}_n|^2 + |\mathcal{M}^{\perp}{}_n|^2\right)$ holds, an expression for the transition amplitude of an incident photon, which is polarised perpendicularly to the strong filed can be provided

$$|\mathcal{M}^{\perp}{}_n|^2 = (1-\sigma)\tilde{J}_n^2(z_-, z_+) + \frac{e^2\mathfrak{a}_0^2}{m^2}\frac{(kk')^2}{4kq^+kq^-}\left[(\tilde{\mathcal{J}}_n^1)^2 - \tilde{J}_n(z_-, z_+)\tilde{\mathcal{J}}_n^2\right]. \quad (3.13)$$

Followingly, the pair production rates per volume for a linearly polarised strong laser field interacting with an incident photon with parallel and perpendicular polarisation read

$$R_{\perp,\parallel} = \frac{e^2m^2}{(2\pi)^2\omega' V_\gamma}\sum_{n\geq n_0}^{\infty}\int \delta^4(nk + k' - q^+ - q^-)\frac{d^3q^-}{q_0^-}\frac{d^3q^+}{q_0^+}|\mathcal{M}^{\perp,\parallel}{}_n|^2, \quad (3.14)$$

while the rate per volume for an unpolarised photon can be obtained via

$$R = \frac{1}{2}\left(R_\perp + R_\parallel\right) = \frac{e^2m^2}{8\pi^2\omega' V_\gamma}\sum_{n\geq n_0}^{\infty}\int \delta^4(nk + k' - q^+ - q^-)\frac{d^3q^-}{q_0^-}\frac{d^3q^+}{q_0^+}|\overline{\mathcal{M}}_n|^2. \quad (3.15)$$

The fact that the summation index starts at $n_0 = 2m_*^2/(kk')$ results as a consequence of the energy-momentum balance.

3.1 Asymptotic study

In this section the asymptotes of the particle creation rate for the Breit-Wheeler process in monochromatic plane wave will be derived. The behaviour of the latter is mainly governed by two dimensionless parameters: the intensity parameter $\xi = |e|\sqrt{-\mathcal{A}^\mu\mathcal{A}_\mu}/m = |e|\mathfrak{a}_0/m > 0$, which encodes the strength of the external field, and the quantum nonlinearity parameter $\kappa = |e|\sqrt{-(f_{\mu\nu}k'^\mu)^2}/m^3 = kk'\xi/m^2$ providing insights on the importance of quantum effects. Depending on the intensity parameter ξ, one distinguishes between perturbative $\xi \ll 1$ and nonperturbative $\xi \gg 1$ regimes.

3.1.1 Small ξ behaviour

In the limit of small intensities, the rate in its most distinctive form is written as an infinite sum of contributions resulting from interaction of the incident photon with n strong field photons

$$R = \sum_{n \geq n_0} R_n, \quad R_n \propto \xi^{2n}. \tag{3.16}$$

As the summands are proportional to ξ^{2n} and $\xi \ll 1$ holds, from the equation above it can be read off that the leading contribution to the pair creation rate is provided, when energetically allowed, by the interaction of two photons. Hence, the terms with $n = 1$ and $n = 2$ are considered in more detail.

The behaviour of the summands in Eq. (3.16) is dictated by the small arguments asymptote of the generalised Bessel functions $\tilde{J}_n(z-, z+)$ as $z_- \propto \xi \ll 1$ and $z_+ \propto \xi^2 \ll 1$ (see appendix B.1). Additionally, the effective electron mass and momenta can be simplified to $m^* \approx m$ and $q_\mu^\pm \approx p_\mu^\pm$. Thus, when employing Eq. (B.8) up to the order $\mathcal{O}(\xi^2)$ for $n = 1$ one obtains

$$|\mathcal{M}^{\parallel}{}_{n=1}|^2 = \frac{\xi^4}{4}\left(\frac{(kk')^2}{4kp^+kp^-} - 1 + \sigma m^2\left[\frac{\epsilon p^+}{kp^+} - \frac{\epsilon p^-}{kp^-}\right]^2\right), \tag{3.17}$$

$$|\overline{\mathcal{M}}_{n=1}|^2 = \frac{\xi^4}{4}\left(\frac{(kk')^2}{2kp^+kp^-} - 1 + m^2\left[\frac{\epsilon p^+}{kp^+} - \frac{\epsilon p^-}{kp^-}\right]^2\right). \tag{3.18}$$

Now, for calculation of the rates per volume a transition to the center of momentum frame is made, where $\boldsymbol{p}^+ = -\boldsymbol{p}^- = \boldsymbol{p} = \sqrt{\omega'^2 - m^2}$ and $p_0^+ = p_0^- = \omega' = \omega$ hold, while the integration over $\boldsymbol{p}^-$ is conducted with help of Dirac delta functions. Moreover, the remaining integrals in spherical coordinates can be written as

$$\int_0^{2\pi} d\varphi \int_{-1}^{1} d\cos(\vartheta) \int \frac{d|\boldsymbol{p}||\boldsymbol{p}|^2}{p_0^2}\delta(2p_0 - 2\omega')... = \frac{1}{2}\int_0^{2\pi} d\varphi \int_1^{u_n} \frac{du}{u\sqrt{u(u-1)}}... \tag{3.19}$$

with $\vartheta = \angle(\boldsymbol{k}, \boldsymbol{p})$ and φ denoting an angle between $(\boldsymbol{k}, \boldsymbol{p})$ and $(\boldsymbol{k}, \boldsymbol{\epsilon})$ planes, i.e. $\epsilon p^+ = -|\boldsymbol{p}|\cos(\varphi)\sin(\vartheta)$. In order to obtain the right hand side of the equation above a substitution

$$\cos(\vartheta) = \frac{p_0}{|\boldsymbol{p}|}\sqrt{1 - \frac{1}{u}} \text{ with } u = \frac{(kk')^2}{4kp^+kp^-} \tag{3.20}$$

was performed and $u_n = n/n_0 = \omega\omega'/m^2$ for $n = 1$. Thus, with the normalised Mandelstam variable $s^2 = kk'/2m^2$ and $\sigma = 1 + \left(\frac{ns^2}{u} - 1\right)\sin(\varphi)$ the rates read

$$R^{\parallel}_{n=1} = \frac{e^2m^2\xi^2}{32\pi^2\omega' V_\gamma}\int_0^{2\pi} d\varphi \int_1^{s^2} \frac{du}{u\sqrt{u(u-1)}}\left(u - 1 + \sigma\left(\frac{2}{s^2}\sqrt{u(s^2-u)}\cos(\varphi)\right)^2\right), \tag{3.21}$$

$$R_{n=1} = \frac{e^2 m^2 \xi^2}{64\pi^2 \omega' V_\gamma} \int_0^{2\pi} d\varphi \int_1^{s^2} \frac{du}{u\sqrt{u(u-1)}} \left(2u - 1 + \left(\frac{2}{s^2} \sqrt{u(s^2-u)} \cos(\varphi) \right)^2 \right) \tag{3.22}$$

and when the integrations are carried out one ends up with

$$R^{\parallel}_{n=1} = \frac{e^2 m^2 \xi^2}{16\pi\omega' V_\gamma} \frac{(3+2s^2)\left[s(1-s^2) - \sqrt{1-s^2}(2s^2-1)\arccos(s)\right]}{2s^4\sqrt{s^2-1}}, \tag{3.23}$$

$$R_{n=1} = \frac{e^2 m^2 \xi^2}{16\pi\omega' V_\gamma} \left[\frac{-s\sqrt{s^2-1}(1+s^2)}{s^4} + \frac{(-1+2(s^2+s^4))\ln(s+\sqrt{s^2-1})}{s^4} \right]. \tag{3.24}$$

Similarly, the expressions for $n = 2$, when taking into account terms up to the order $\mathcal{O}(\xi^4)$, are derived with help of Eq. (B.9) where the relevant contributions involving generalised Bessel were obtained. Hence, the squared transition amplitudes result to

$$|\mathcal{M}^{\parallel}{}_{n=2}|^2 = \left(\sigma \left(\frac{z_-^2}{8} + \frac{z_+}{2} \right)^2 - \xi^2 (1-u) \left(\frac{z_-^2}{32} - \frac{z_+}{8} \right) \right), \tag{3.25}$$

$$|\overline{\mathcal{M}}_{n=2}|^2 = \left(\left(\frac{z_-^2}{8} + \frac{z_+}{2} \right)^2 - \xi^2 (1-2u) \left(\frac{z_-^2}{32} - \frac{z_+}{8} \right) \right) \tag{3.26}$$

and, when integrated in the center of momentum frame where for $n = 2$ the relation $\omega' = 2\omega$ holds, the particle rates per volume approximate

$$R^{\parallel}_{n=2} = \frac{e^2 m^2 \xi^4}{4\pi\omega' V_\gamma} \left(\frac{s\sqrt{4s^2-2}(75 - 170s^2 + 28s^4 + 144s^6)}{1536 s^8} + \frac{3(25 - 90s^2 + 76s^4)\mathrm{arcsinh}(\sqrt{2s^2-1})}{1536 s^8} \right), \tag{3.27}$$

$$R_{n=2} = \frac{e^2 m^2 \xi^4}{8\pi\omega' V_\gamma} \left(\frac{s\sqrt{4s^2-2}(15 - 40s^2 + 12s^4 + 48s^6)}{256 s^8} + \frac{15(1-2s^2)^2 \mathrm{arcsinh}(\sqrt{2s^2-1})}{256 s^8} \right). \tag{3.28}$$

3.1.2 Large ξ behaviour

The calculation of the pair production rates for $\xi \gg 1$ presented in this subsection draws on Ref. [2]. In this limit, a large number of laser photons participates in the particle creation. Hence, many summands from Eqs. (3.14) and (3.15) provide similar contributions to the particle rate and a transition to the continuum limit $\sum_n ... \to \int dn$ can be performed. Afterwards, the integrations over $\boldsymbol{q}^+$ and n are

successively solved with help of the Dirac delta functions with

$$\boldsymbol{q}^+ = n\boldsymbol{k} + \boldsymbol{k}' - \boldsymbol{q}^-,\ q_0^+ = n\omega + \omega' - q_0^- \tag{3.29}$$

and

$$\delta(n\omega + \omega' - q_0^+ - q_0^-) = \left|\frac{q_0^+}{kq^+}\right| \delta(n - n^*),\ n^* = \frac{k'q^-}{k(k' - q^-)}. \tag{3.30}$$

In such a scenario the rates from Eq. (3.14) read

$$R_{\perp,\parallel}^{\xi\gg1} = \frac{e^2m^2}{(2\pi)^2\omega' V_\gamma} \int_{-\infty}^{\infty} dq_1^- \int_{-\infty}^{\infty} dq_2^- \int_{-\infty}^{\infty} \frac{dq_3^-}{q_0^- kq^+} |\mathcal{M}^{\perp,\parallel}{}_{n^*}|^2. \tag{3.31}$$

Next, without loss of generality it is assumed that the strong field propagates in x_3-direction and its polarisation vector is $\boldsymbol{\epsilon} = (1, 0, 0)$. Then, the new variables

$$\begin{aligned}
&\chi^+ = \frac{kq^+}{m^2}\xi, \chi^- = \frac{kq^-}{m^2}\xi,\\
&\lambda = \omega' - k_3',\ \gamma^+ = q_0^+ - q_3^+,\ \gamma^- = q_0^- - q_3^-,\\
&\cos(x_0) = -\frac{z_-}{8z_+} = \frac{q^+\epsilon\ q^-k - q^-\epsilon\ q^+k}{m\xi kk'} = \frac{q_1^-\gamma^+ - q_1^+\gamma^-}{m\xi\lambda},\\
&\mathfrak{t} = \frac{q_2^-\gamma^+ - q_2^+\gamma^-}{m\lambda} \text{ with } \sigma = 1 + \mathfrak{t}^2
\end{aligned} \tag{3.32}$$

are introduced and substitutions in the integration variables are performed, so that one arrives at

$$R_{\perp,\parallel}^{\xi\gg1} = \frac{e^2m^2}{(2\pi)^2\omega' V_\gamma} \int_0^{\pi/2} dx_0 \int_0^{\infty} d\mathfrak{t} \int_0^{\kappa/2} d\chi^- \frac{8\xi^2 \sin(x_0)}{\chi^+\chi^-} |\mathcal{M}^{\perp,\parallel}{}_{n^*}|^2, \tag{3.33}$$

since the integrand is an even function in $\cos(x_0)$ and $\mathfrak{t}$. In order to define the integration region in χ' the energy-momentum conservation and symmetry of the integrand in χ^- and χ^+ with $\chi^- + \chi^+ = \kappa$ were taken into account (the latter results in $\chi^- \in [0, \kappa/2]$). Further, the substitutions $\mathfrak{t} = \sinh(u)$ and $\chi^- = \kappa(1 + \tanh(v))/2$ are made and large argument asymptotes of generalised Bessel functions from Eq. (B.30) are employed in the equations above resulting in

$$\begin{aligned}
R_{\parallel}^{\xi\gg1} \approx \frac{4e^2m^2}{\pi^3\omega' V_\gamma} \int_0^{\pi/2} dx_0 \int_0^{\infty} du \int_0^{\infty} dv \frac{\sqrt{z}\cosh^2(u)}{\cosh^2(v)} \big(\Phi^2(z) + \\
\sinh^2(v)\left[\Phi^2(z) + \frac{\Phi'^2(z)}{z}\right]\Big)
\end{aligned} \tag{3.34}$$

and

$$R_{\perp}^{\xi\gg1} \approx \frac{4e^2m^2}{\pi^3\omega' V_\gamma}\int_0^{\pi/2} dx_0 \int_0^\infty du \int_0^\infty dv \frac{\sqrt{z}\cosh^2(u)}{\cosh^2(v)}\left(-\tanh^2(u)\Phi^2(z)+ \cosh^2(v)\left[\Phi^2(z)+\frac{\Phi'^2(z)}{z}\right]\right) \quad (3.35)$$

with the Airy function $\Phi(z) = \frac{1}{\sqrt{\pi}}\int_0^\infty \cos(t^3/3+zt)dt$ and its derivative $\Phi'(z)$ of argument $z = \left(\frac{2\cosh^2(v)}{\kappa\sin(x_0)}\right)^{2/3}\cosh^2(u)$. Finally, one evaluates the integrals above asymptotically for different values of κ and arrives at (compare Eqs. (36') and (36") in Ref. [2]) for $\kappa \ll 1$

$$R_\parallel = \frac{3e^2m^2}{32\omega' V_\gamma}\left(\frac{\kappa}{2\pi}\right)^{3/2} \mathrm{e}^{-8/(3\kappa)},\ R_\perp = 2R_\parallel \quad (3.36)$$

and

$$R_\parallel = \frac{27\Gamma^7\left(\frac{2}{3}\right)e^2m^2}{56\pi^5\omega' V_\gamma}\left(\frac{3\kappa}{2}\right)^{2/3},\ R_\perp = \frac{3}{2}R_\parallel \quad (3.37)$$

for $\kappa \gg 1$.

3.2 Constant crossed fields

When writing $\xi = |e|\mathcal{E}_0/(m\omega)$ with the amplitude of the electromagnetic field $\mathcal{E}_0$ it can be realised that the limit $\xi \gg 1$ can be seen as a limit to decreasing frequency ω at constant intensity. Hence, following Ref. [2], a connection between a probability of a process $F(\mathcal{E}_0)$ in a constant field, whose magnetic and electric field strengths are equal and orthogonal with amplitude $\mathcal{E}_0$ (constant crossed field), and probability of the same process $R(\mathcal{E}_0\sin(x_0))$ in an alternating field of plane wave exists, if the latter varies slowly enough

$$R(\mathcal{E}_0) = \frac{2}{\pi}\int_0^{\pi/2} dx_0\ F(\mathcal{E}_0\sin(x_0)). \quad (3.38)$$

To that end, the rates of the Breit-Wheeler pair creation in a constant crossed field can be read off from Eqs. (3.34) and (3.35). Moreover, in Refs. [3, 4, 5] it is shown that the rates per volume with fixed polarisation for the process in question can be written as

$$F_{\parallel,\perp} = -\frac{\alpha m^2}{6\sqrt{\pi}\omega' V_\gamma}\int_1^\infty \frac{du(8u+1\mp3)}{u\sqrt{u(u-1)}}\frac{\Phi'(z)}{z} \quad (3.39)$$

with argument $z = (4u/\kappa)^{2/3}$ and $F = \frac{1}{2}(F_\parallel + F_\perp)$.

3.2.1 Limits for small and large κ

Depending on the quantum nonlinearity parameter, Eqs. (3.39) can be evaluated asymptotically resulting in

$$F_{\parallel} = \sqrt{\frac{3}{2}} \frac{e^2 m^2}{32\pi\omega' V_\gamma} \kappa \mathrm{e}^{-8/(3\kappa)}, \; F_{\perp} = 2R_{\parallel} \tag{3.40}$$

for $\kappa \ll 1$ and

$$F_{\parallel} = \frac{3\Gamma^4\left(\frac{2}{3}\right) e^2 m^2}{28\pi^3 \omega' V_\gamma} (3\kappa)^{2/3}, \; F_{\perp} = \frac{3}{2} R_{\parallel} \tag{3.41}$$

for $\kappa \gg 1$. Thus, for small κ the rate shows exponential suppression, which is typical for tunnelling processes and Schwinger pair production. For large nonlinearity parameters some remarks are in order. Firstly, the expressions for $\kappa \gg 1$ apply as long as $\xi \gg \max\{1, \kappa^{1/3}\}$ holds (see appendix B.2). Moreover, Eq. (3.41) combined with the optical theorem provides insights on the validity of the perturbation theory introduced in Sec. 2.1: The perturbative expansion is valid as long as radiative corrections to the quantised radiation field remain negligible, i.e. if the condition $\alpha\kappa^{2/3} \ll 1$ is fulfilled. Hence, for strong electromagnetic fields the condition $\alpha \ll 1$ should be modified to $\alpha\kappa^{2/3} \ll 1$ [5].

3.2.2 Limit for $\xi \gg 1$, $\kappa \approx 1$

This subsection is based on section II C of Ref. [51], where the asymptote of the crossed constant field Breit-Wheeler rate per volume in the strong field regime ($\xi \gg 1, \; \kappa \sim 1$) was derived. This parameter configuration is of high relevance as it is planned to be studied experimentally at CALA in the near future [33].

In order to establish the behaviour of F in this limit, one starts with the relation

$$\Phi'(z) = -\frac{z}{\sqrt{3\pi}} K_{2/3}\left(\frac{2}{3} z^{3/2}\right), \tag{3.42}$$

where $K_\nu(x)$ stands for the modified Bessel function of the second kind [52]. As a consequence, the unpolarised rate resulting from Eq. (3.39)

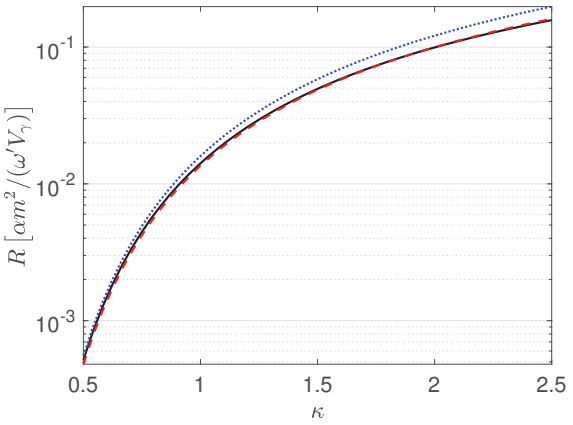

Figure 3.3: Comparison of the rate given in Eq. (3.43) (black solid) with the analytical asymptotes for $\kappa \approx 1$ from Eq. (3.44) (red dashed) and $\kappa \ll 1$ (blue dotted). This figure was originally published in Ref. [51].

can be written as

$$F = \frac{\alpha m^2}{6\pi\omega' V_\gamma}\frac{8}{3^{3/2}\kappa}\int_{\frac{8}{3\kappa}}^{\infty} dp \frac{3\kappa p + 1}{p^{3/2}\sqrt{p-\frac{8}{3\kappa}}} K_{2/3}(p), \tag{3.43}$$

where the change of variable $p = 8u/(3\kappa)$ has been carried out. Since $p \in [\frac{8}{3\kappa}, \infty)$ holds, the first contribution in the numerator is always substantially larger than 1 and the latter can be ignored. Moreover, for $\kappa \sim 1$ the main contribution in the integral results from the region $p \sim 8/(3\kappa)$, which is substituted in the integrand and one ends up with

$$F_{\kappa\approx 1} \approx \frac{\alpha m^2}{6\pi\omega' V_\gamma}\sqrt{8\kappa}\int_{\frac{8}{3\kappa}}^{\infty} dp \frac{K_{2/3}(p)}{\sqrt{p-\frac{8}{3\kappa}}} = \frac{\alpha m^2}{\pi\omega' V_\gamma}\left(\frac{2}{3}\right)^{3/2} K_{7/12}\left(\frac{4}{3\kappa}\right) K_{1/12}\left(\frac{4}{3\kappa}\right). \tag{3.44}$$

Note that the restrictions provided below Eq. (3.37) apply also in the present case.

The behaviour of the numerically evaluated rate given in Eq. (3.43) as a function of κ is shown as black solid line in Fig. 3.3. It is compared with the asymptotic rate from Eq. (3.44) (red dashed) and the one corresponding to the case $\kappa \ll 1$ (blue dotted). In the region of interest for this section the black solid and red dashed curves overlap. Indeed, for $\kappa \in [1.5, 2.5]$ the error introduced by Eq. (3.44) lies below 2% and grows to approximately 10% for $\kappa \ll 1$. This analysis reveals that $F_{\kappa\approx 1}$ provides a good description of the pair production in the considered limit.

Chapter 4

Pair production from bremsstrahlung in a focused field

In this chapter a theoretical study of an approach for detection of Breit-Wheeler pairs is presented. The latter combines a perturbative photon generated via bremsstrahlung with a laser field, this way providing the needed high energy to the system and allowing the process to take place. The scheme relies on the proposal of Reiss [53], where an idea to probe the Breit-Wheeler pair creation via bremsstrahlung-laser interaction was presented initially[1]. Here, the emphasis lies on a realistic description of the involved fields: on the one hand, bremsstrahlung is incorporated via a photon distribution function, which is characterised by a photon energy spectrum and not a sharp energy value. On the other hand, focusing of the laser is integrated in the calculation as the needed intensities are solely provided in tightly focused laser fields.

The scheme of the proposed setup is depicted in Fig. 4.1. Here, bremsstrahlung photons are supposed to be generated by ultrarelativistic few-GeV electrons that penetrate a high-Z target material producing in this way a broad spectrum of bremsstrahlung radiation reaching energies up to several GeV. For acceleration of electrons the laser wake-field acceleration (LWFA) method [33, 56, 57] is recommended as it provides highly collimated and intense beams, which are required for such endeavours. At the envisaged electron energies, in the high-Z target alongside with the emission of bremsstrahlung Bethe-Heitler pairs can also be created, since atomic Coulomb fields may lead to a photon decay [58, 59]. Thus, in order to keep the interaction point free from particles not related to the process of interest (i.e. Bethe-Heitler pairs and incident electrons), a strong magnet needs to be introduced, which can sidetrack noise particles over a distance L. In the present context, $L \propto \mathcal{O}(1)$ m is needed.

Next, depending on the employed laser class, an experimental observation of both linear and highly nonlinear nonperturbative regimes of Breit-Wheller pair production is possible. To that end, if an x-ray free-electron laser (XFEL) emitting keV photons is incorporated, the energy of the system would be sufficient for production of an electron positron pair from two photons. Such scenario, where $\xi \ll 1$

[1] Similar configurations were also considered in Refs. [19, 32, 33, 54, 55].

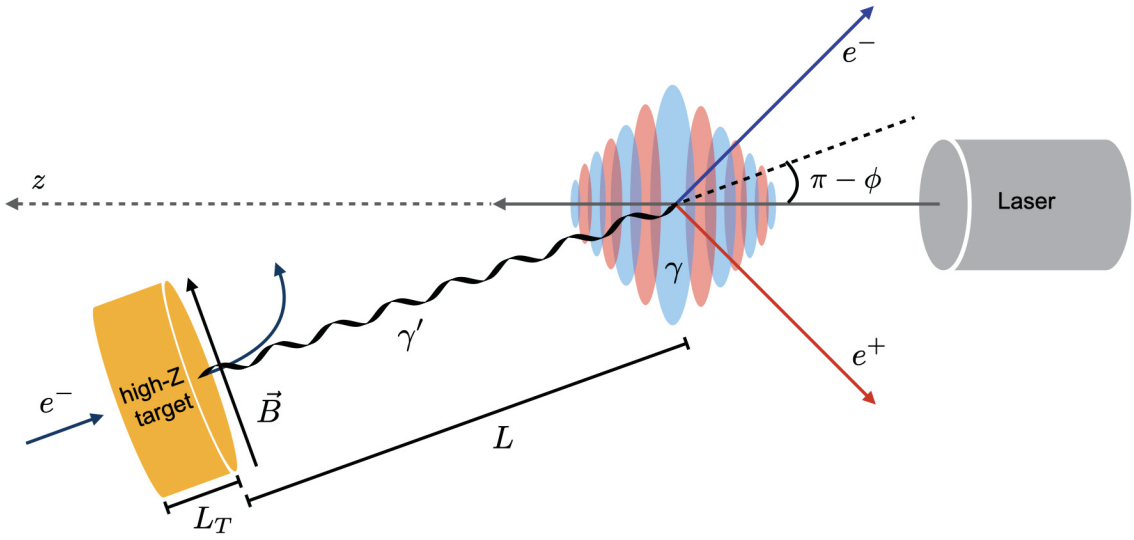

Figure 4.1: Scheme of the setup envisaged to experimentally observe Breit-Wheeler pair creation as a result of collisions of bremsstrahlung γ quanta with a laser pulse.

holds, is investigated in section 4.2, which is based on Ref. [60]. Alternatively, an optical laser of high intensity can be used that allows for reaching the $\xi \gg 1$, $\kappa \approx 1$ regime. The corresponding experimental setup is put forward by a group at CALA and is described in Ref. [33]. A thorough theoretical study of the latter scenario is discussed in detail in section 4.3, where, in particular, effects of longitudinal and transversal focusing when modelling the laser field as a focussed paraxial Gaussian pulse are displayed, limits of the paraxial approximation are discussed and super-Gaussian envelopes are incorporated. This section relies on results published initially in Ref. [51].

4.1 General aspects

As described above, the main constituents of the proposed setup for creation of Breit-Wheeler pairs are bremsstrahlung photons and a high intensity laser (see Fig. 4.1). Thus, in this section the theoretical description of the latter is provided starting with the laser field.

4.1.1 Focused laser

Unless stated otherwise, the focused laser in this chapter is modelled as a linearly polarised Gaussian pulse in paraxial approximation propagating in $z-$direction[2] with polarisation $\boldsymbol{\epsilon} = (1, 0, 0)$. Consequently, the only nonvanishing electric and

[2]The focal point of the Gaussian pulse is set to define the origin.

magnetic field components $\mathcal{E}_x = \mathcal{B}_y$ read (see Ref. [61])

$$\mathcal{E}_x = \mathcal{E}_0 \frac{\mathrm{e}^{-\left(\sqrt{2\ln(2)}\frac{(t-z)}{\tau}\right)^2}}{\sqrt{1+\zeta^2(z)}} \mathrm{e}^{-\left(\frac{r}{w(z)}\right)^2} \sin(\Phi), \tag{4.1}$$

with the pulse phase

$$\Phi = \Phi_0 + \omega(t-z) - \zeta(z)\frac{r^2}{w^2(z)} + \arctan(\zeta), \tag{4.2}$$

where Φ_0 stands for the constant phase and $w(z) = w_0\sqrt{1+\zeta^2(z)}$ denotes the beam width. The latter depends on the longitudinal coordinate z via the factor $\zeta(z) = z/z_R$ with the Rayleigh length $z_R = \pi w_0^2/\lambda$ and the beam waist size w_0 at the focal point ($z = 0$). The transversal focusing of the pulse is accounted for by the nontrivial dependence on $r^2 = x^2 + y^2$, whereas its temporal envelope is governed by τ, which is taken at FWHM from the intensity distribution.

4.1.2 Bremsstrahlung photons

In order to incorporate bremsstrahlung radiation into the process of Breit-Wheeler pair production, the corresponding pair creation rate R is weighted by the distribution function $W(\boldsymbol{k}')$ of the bremsstrahlung photons and integrated over the photon momentum $\boldsymbol{k}'$

$$R_\gamma = \int \frac{d^3k'}{(2\pi)^3} W(\boldsymbol{k}')\ R(\boldsymbol{k}'). \tag{4.3}$$

Since the incident electrons form a highly collimated beam with energies E_0 exceeding the GeV scale, the spreading angle of bremsstrahlung photons can be approximated by the inverse electron Lorentz factor $\theta_\gamma \approx 1/\gamma_e = m/E_0 \sim \mathcal{O}(1)$ mrad. Under such circumstances, the vast majority of the bremsstrahlung photons is emitted tangentially to the direction of propagation of the initial electron beam and its spectral distribution in spherical coordinates can be approximated by ($\omega' = |\boldsymbol{k}'|$)

$$W(\boldsymbol{k}') \approx \frac{(2\pi)^3 I_\gamma(f,\ell)}{\omega'^2 \sin(\theta_{\boldsymbol{k}'}) E_0} \Theta(E_0 - \omega')\delta(\theta_{\boldsymbol{k}'} - \phi)\delta(\phi_{\boldsymbol{k}'}), \tag{4.4}$$

where $\Theta(x)$ denotes the unit step function. Here, $I_\gamma(f,\ell)$ is the energy spectrum of bremsstrahlung photons with $f = \omega'/E_0$ being the normalised photon energy and $\ell = L_T/L_{\mathrm{rad}}$ the normalised target thickness. In this formula L_{rad} is the radiation length of the target material ($L_{\mathrm{rad}} = 3.5$ mm for tungsten and $L_{\mathrm{rad}} = 5.6$ mm for lead) and L_T stands for the target thickness. Moreover, the collision angle (see Fig. 4.1) is denoted as ϕ. After integrating out the angular variables, one ends up with the following expression for the rate of produced electron-positron pairs per

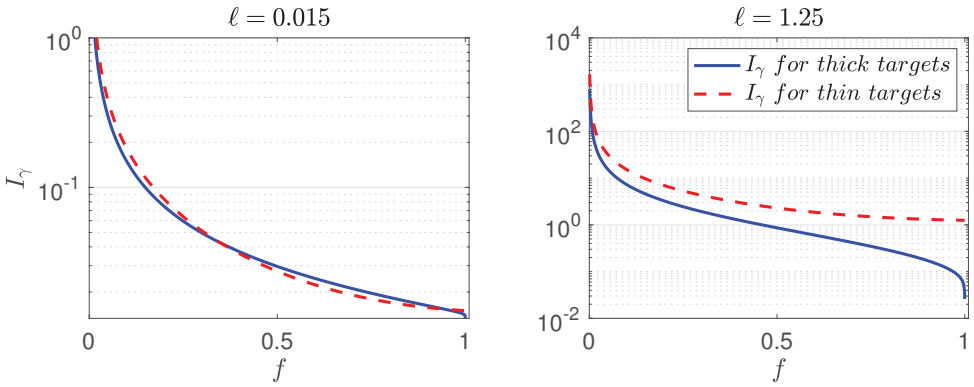

Figure 4.2: Bremsstrahlung spectra according to Eqs. (4.6) (red dashed) and (4.7) (blue solid). The figure on the left was originally published in Ref. [51].

incident radiating electron

$$R_\gamma \approx \int_0^1 df I_\gamma(f,\ell)\ R \tag{4.5}$$

once a change of variable $\omega' = fE_0$ has been carried out. When the solid high-Z target is thin, i.e. $\ell \ll 1$, the energy spectrum of bremsstrahlung photons in the full screening approximation[3] is given by [62, 63]

$$I_\gamma(f,\ell) \approx \frac{\ell}{f}(\frac{4}{3} - \frac{4f}{3} + f^2), \tag{4.6}$$

whereas for thicker targets with $\ell < 2$ the bremsstrahlung spectrum approximates [63]

$$I_\gamma(f,\ell) \approx \frac{(1-f)^{4\ell/3} - \mathrm{e}^{-7\ell/9}}{f\left(\frac{7}{9} + \frac{4}{3}\ln(1-f)\right)}. \tag{4.7}$$

The outcomes from Eqs. (4.6) (dased red) and (4.7) (blue solid) are compared in Fig. 4.2. In the left panel a very thin target ($\ell = 0.015$) is chosen, whereas a thick target is considered on the right. For $\ell \ll 1$ both models (4.6) and (4.7) describe the spectrum of bremsstrahlung photons well (as it is demonstrated by comparison with numerical GEANT4 simulations in, for example, Refs. [32, 33]). However, both spectra show an unrealistic divergence in the infrared limit $f \to 0$, which will be taken into account by limiting the impact of the lower energetic photons in the further study. Thus, the negative impact of this part of the spectrum will not harm the precision of the calculations. Moreover, even for thin targets Eq. (4.6) does not manifest the characteristic steep decrease at the point $f \approx 1$, which represents

[3]Commonly, the bremsstrahlung spectrum depends on the target material via the atomic number Z, which is included in Eq. (4.6) in terms of the radiation length L_{rad}. Additional Z-dependent terms have been ignored, which introduces a minor error of maximal 2.5% [62, 63]. Moreover, the term "complete screening" refers to screening of nuclear Coulomb potentials by atomic electrons, which is particularly effective at high energies E_0 and small emission angles θ_γ.

the fact that no photons with energies exceeding E_0 can be created. To that end, in Sec. 4.3, where thin targets will be of main interest, the rates resulting from Eqs. (4.6) and (4.7) will be studied separately. Lastly, for thick targets (which will be considered in Sec. 4.2), Eq. (4.7) will be employed as it was shown to have good precision when compared to GEANT4 simulations in Ref. [32].

4.1.3 Volume of bremsstrahlung radiation

In the discussed type of experiments, the spatial extensions of the interacting laser and bremsstrahlung beams play a very important role. As it can be seen from the scheme provided for a counterpropagating geometry in Fig. 4.3, the interaction volume is mainly defined by the area around the focal point of the laser and, due to the spreading, only a small number of bremsstrahlung photons is able to participate in the process, which has a huge negative impact on the number of created Breit-Wheeler pairs. Here, an estimation of the volume covered by bremsstrahlung radiation (dark blue in Fig. 4.3) is provided

$$V_\gamma \approx \pi \sigma_z \bar{r}^2 \quad \text{with} \quad \bar{r} = \frac{r_{\min} + r_{\max}}{2} \tag{4.8}$$

denoting the average radius of the truncated cone formed by the bremsstrahlung burst. In the expression above, the maximal and minimal radii $r_{\max} \approx \theta_{\text{rms}}\sigma_z + r_{\min}$ and $r_{\min} = \sigma_r + L_{e^-}\theta_{e^-} + L\theta_{\text{rms}}$, respectively, depend on the transversal σ_r and longitudinal σ_z extensions of the witness electron beam[4]. Moreover, the root-mean squared of the spreading angle of the bremsstrahlung photons reads $\theta_{\text{rms}} = (\theta_{e^-}^2 + \theta_\gamma^2)^{\frac{1}{2}}$. In this chapter, the electron beam spreading is characterized by parameters provided in Ref. [33]: the spreading angle is set to $\theta_{e^-} \approx 0.5$ mrad, while the distance travelled by the electrons towards the high-Z target equals $L_{e^-} = 10$ cm. Further, as $L \propto \mathcal{O}(1)$ m and $\sigma_r \propto \mathcal{O}(1)$ μm in general hold, the averaged radius approximates $\bar{r} \approx r_{\min} \approx L_{e^-}\theta_{e^-} + L\theta_{\text{rms}}$. Finally, ideal collisions characterised by perfect synchronisations of the colliding beams will be considered and, in order to minimise the longitudinal mismatching, the axial bremsstrahlung extension σ_z will be chosen in a way that at $t = 0$ it covers the focal region of the laser pulse. Thus, unless stated otherwise, $\sigma_z \approx 2z_R$.

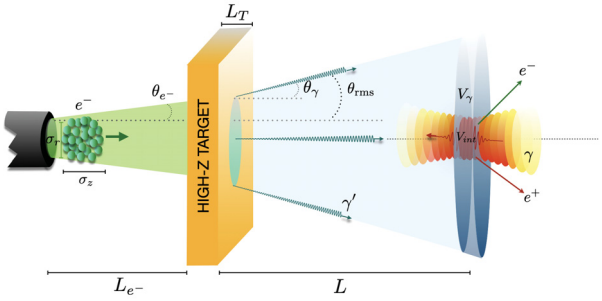

Figure 4.3: Scheme of the proposed experiment elucidating spreading of the bremsstrahlung beam (blue). A variation of this figure was originally published in Ref. [51].

[4] In general, the beam parameters for LWFA depend on the density of plasma, in which the wake-field is generated [64, 65, 66].

4.2 Linear Breit-Wheeler pair production

In this section a theoretical perturbative development of linear electron-positron pair creation in context of the setup proposed above with an x-ray laser pulse and highly energetic bremsstrahlung is shown. Here, in contrast to the well established procedure where both photons are quantised, the ansatz introduced in subsection 2.2.2 is pursued allowing for modelling the laser as a focused pulse. To that end, firstly, the theoretical framework describing an interaction between a classical laser field and a quantised photon is presented. Next, laser focusing is taken into account by particularising the laser field model to a Gaussian pulse and the bremsstrahlung energy distribution is incorporated as it was shown in subsection 4.1.2. Consequently, estimations of the number of created Breit-Wheeler pairs are provided and results are discussed. Note that this section draws on Ref. [60].

4.2.1 Pair production in an arbitrary laser field

As usual, the linear Breit-Wheeler process is described by the second-order S-matrix element S_{fi} with $\hat{S}^{(2)}[\hat{\psi}, \hat{\bar{\psi}}, \hat{a}]$ given in the second line of Eq. (2.6). However, while the electron-positron pair and incident quantised photon are treated as Fock number states, the laser field is included via a coherent state $|\alpha_k\rangle$ in the mode k [5]. Thus, for an electron and positron with spins and four-momenta $p_{\mp}, s_{\mp}$ and a quantised photon with wave four-vector k' and polarisation ϵ' the S-matrix element reads

$$S_{fi} = \langle 1_{p_+,s_+}; 1_{p_-,s_-}; \alpha_k | \hat{S}^{(2)}[\hat{\psi}, \hat{\bar{\psi}}, \hat{a}] | 1_{k',\epsilon'}; \alpha_k \rangle \rightarrow \\ \langle 1_{p_+,s_+}; 1_{p_-,s_-} | \hat{S}^{(2)}[\hat{\psi}, \hat{\bar{\psi}}, \hat{a} + \mathcal{A}] | 1_{k',\epsilon'} \rangle, \quad (4.9)$$

where the transition involving a classical laser field $\mathcal{A}^\mu(x)$ from Eq. (2.13) was performed. Based on the equation above, the Breit-Wheeler process for a field of arbitrary shape can be calculated, since the latter may be written as a linear superposition of wave modes. To that end, using the expressions for field operators as well as applying Eqs. (2.8), (2.17) and (2.19) leads to

$$S_{fi} = i^2 e^2 \sqrt{\frac{1}{2\omega' V_\gamma} \frac{m^2}{p_0^+ p_0^- V^2}} \left(\int d^4x \; d^4y \; \bar{u}_{p^-,s^-} \not{\mathcal{A}}(x) S_F(x-y) \not{\epsilon}' v_{p^+,s^+} \mathrm{e}^{i(p_+ - k')y + ip_- x} \right. \\ \left. \int d^4x \; d^4y \; \bar{u}_{p^-,s^-} \not{\epsilon}' S_F(x-y) \not{\mathcal{A}}(y) v_{p^+,s^+} \mathrm{e}^{i(p_- - k')x + ip_+ y} \right). \quad (4.10)$$

When inserting the Feynman propagator in its Fourier representation from Eq. (2.20) into the two terms in the equation above, the integrations in y and x, respectively,

[5] In the further discussion a free electron laser is assumed as a possible source of x-ray radiation. Even though the latter possesses a high degree of transverse coherence and an improved longitudinal coherence when compared to synchrotron radiation sources [67, 68, 69], it is not fully coherent. However, as long as only one FEL photon participates in the reaction, the precise photon statistics in the FEL pulse will not affect the rate of the process.

can be performed resulting in Dirac delta functions, which make the integrations over p stemming from $S_F(x-y)$ trivial. Next, the four-potential of the form $\mathcal{A}^\mu(x) = \epsilon^\mu \mathfrak{a}(k,x)$, where ϵ^μ stands for the field polarisation, will be considered. Thus, the remaining integrals can be absorbed into the Fourier transformed of the vector potential amplitude

$$\tilde{\mathfrak{a}}(\tilde{k},k) = \int d^4x\, \mathrm{e}^{i\tilde{k}x}\mathfrak{a}(x,k), \tag{4.11}$$

which allows for writing the S-matrix element as

$$\begin{aligned} S_{fi} = i^3 e^2 \sqrt{\frac{1}{2\omega' V_\gamma}\frac{m^2}{p_0^+ p_0^- V^2}}\tilde{\mathfrak{a}}(p_- + p_+ - k', k) \\ \times \bar{u}_{p^-,s^-}\left(\not{\epsilon}'\frac{1}{(\not{p}_- - \not{k}') - m + i0^+}\not{\epsilon} + \not{\epsilon}\frac{1}{(\not{k}' - \not{p}_+) - m + i0^+}\not{\epsilon}'\right) v_{p^+,s^+}. \end{aligned} \tag{4.12}$$

Similarly to Eq. (3.7), the unpolarised rate per volume of the process is obtained after averaging over the polarisations of the quantised photon (which is suitable since the bremsstrahlung photons considered next are unpolarised) as well as summation over the fermions spins

$$R = \frac{1}{2}\sum_{\lambda'}\sum_{s^+,s^-}\int \frac{V d^3p_+}{(2\pi)^3}\frac{V d^3p_-}{(2\pi)^3}\frac{|S_{fi}|^2}{TV}, \tag{4.13}$$

where the squared S-matrix element, while divided over the interaction time T and volume V, is integrated over the phase space of the created particles. Thus, with Eq. (2.9) and properties of elementary spinors from Eq. A.5 the transition amplitude can be written as

$$\begin{aligned} \frac{1}{2}\sum_{\lambda'}\sum_{s^+,s^-}|S_{fi}|^2 = -\frac{e^4}{2}\frac{1}{2\omega' V_\gamma}\frac{m^2}{p_0^+ p_0^- V^2}\int d^4\tilde{k}|\tilde{\mathfrak{a}}(\tilde{k},k)|^2\delta^4(\tilde{k} - (p_- + p_+ - k')) \\ \times \frac{1}{4m^2}\mathrm{Tr}\left[\left(\gamma^\mu\frac{1}{(\not{\tilde{k}} - \not{p}_+) - m + i0^+}\not{\epsilon} + \not{\epsilon}\frac{1}{(\not{k}' - \not{p}_+) - m + i0^+}\gamma^\mu\right)\left(\not{p}_+ - m\right)\right. \\ \left.\left(\not{\epsilon}\frac{1}{(\not{\tilde{k}} - \not{p}_+) - m + i0^+}\gamma_\mu + \gamma_\mu\frac{1}{(\not{k}' - \not{p}_+) - m + i0^+}\not{\epsilon}\right)\left(\not{p}_- + m\right)\right]. \end{aligned} \tag{4.14}$$

After calculating the traces using the properties of the Dirac $\gamma-$matrices from appendix A.1.1, energy-momentum balance as well as $\tilde{k}^2 = 0$ [6] and integrating the rate in the center of momentum frame (as it was shown in subsection 3.1.1 for the

[6] The condition for on-shell photons will be provided later on by the field models for all considered field configurations.

asymptotic expression for $n = 1$) the rate per volume is equal to

$$R = \frac{1}{TV} \int \frac{d^4\tilde{k}}{(2\pi)^4} |\tilde{\mathfrak{a}}(\tilde{k}, k)|^2 \frac{R_{n=1}}{N^2} \tag{4.15}$$

with $R_{n=1}$ from Eq. (3.22) and $N^2 = \mathfrak{a}_0^2/4$. In general, N stands for the photon normalisation associated with the strong field. Thus, if the latter is quantised as it was shown in subsection 2.2.1, the corresponding expression would read $N = 1/\sqrt{2\omega V_\gamma}$. However, when no normalisation to one particle in the volume is performed, which was the case in subsection 3.1.1, the relation $1/\sqrt{2\omega V_\gamma} \equiv \mathfrak{a}_0/2$ holds and the equation below Eq. (4.15) is valid.

4.2.2 Pair production in the field of a Gaussian pulse

In this section the laser field is modelled as a linearly polarised Gaussian pulse in paraxial approximation, which was described in subsection 4.1.1. Thus, following the expression above the absolute value squared of the Fourier transformed amplitude $\tilde{\mathfrak{a}}(\tilde{k}, k)$ is required for further proceeding, which is provided in appendix C.1. To that end, inserting the latter into Eq. (4.15) the rate per volume in cylindrical coordinates reads

$$\begin{aligned} R = \frac{\mathcal{E}_0^2}{32N^2} \frac{(\tau/\sqrt{2\ln(2)})^2 w_0^4}{TA} \int_0^{2\pi} d\phi_{\tilde{k}} \int_{-\infty}^{\infty} d\tilde{k}_z \\ \times \int_0^{|\tilde{k}_0|} d\tilde{k}_\perp \; \tilde{k}_\perp \mathrm{e}^{-\frac{\tilde{k}_\perp^2 w_0^2}{2}} \int_{-\infty}^{\infty} \frac{d\tilde{k}_0}{\tilde{k}_0^2} \mathrm{e}^{-\frac{(\tau/\sqrt{2\ln(2)})^2}{2}(\omega - \tilde{k}_0)^2} \delta(\tilde{k}_z - \tilde{k}_0 + \frac{\tilde{k}_\perp^2}{2\omega}) R_{n=1}, \end{aligned} \tag{4.16}$$

where the contribution responsible for the negative frequency was not taken into account and the integration limit in $\tilde{k}_\perp$ was modified in accordance with the fact, that $\tilde{k}_\perp$ can not exceed the photon energy $|\tilde{k}_0|$. Moreover, the factor A arises from the division of the integration volume V by a length factor which stems from squaring the Dirac δ-function. Next, the integration over $\tilde{k}_z$ is carried out by exploiting the latter and, afterwards, integration over $\tilde{k}_0$ is performed asymptotically by evaluating all components of the integrand except the exponential function at $\tilde{k}_0 = \omega$ as it provides the biggest contribution to the integral. From Eq. (3.22) it can be seen that the two-photon rate $R_{n=1}$ depends mainly on the Mandelstam variable $s^2 \propto k'\tilde{k}$. In the scenario discussed here it can be approached by

$$\tilde{k}k' \approx \omega\omega' \left(1 - \cos(\phi_{\tilde{k}}) \sqrt{1 + \frac{\tilde{k}_\perp^4}{4\omega^4}}\right) \tag{4.17}$$

and when substituting $v = \frac{\tilde{k}_\perp w_0}{\sqrt{2}}$ one obtains

$$R(k,k') \approx \frac{\mathcal{E}_0^2}{4\omega^2 N^2} \frac{(\tau/\sqrt{2\ln(2)})}{TA} \sqrt{\frac{\pi}{2}} \frac{w_0^2}{2} \int_0^{\frac{\omega w_0}{2}} dv\ v\mathrm{e}^{-v^2} \times \int_0^{2\pi} d\phi_{\tilde{k}} R_{n=1} \left[\omega\omega' \left(1 - \cos(\phi) \sqrt{1 + \frac{v^4}{w_0^4 \omega^4}} \right) \right]. \quad (4.18)$$

Here, the angle ϕ in the argument of the two-photon rate is treated as an external parameter dictated by the experimental setup in Fig. 4.1 and, thus, is not dependent on the integration variables. Its value is chosen in a way to allow for a practicable geometry of the experimental setup which avoids damage of technical devices by high intensity beams. In the paraxial approximation, which is assumed to be valid for the modelled Gaussian pulse (see Eq. (4.1)), the relation $\tilde{k}_\perp \ll \omega$ holds and the square root in the argument of $R_{n=1}$ approximates to 1. Thus, consequently, the rate of the process becomes

$$R(\omega, \omega', \cos(\phi)) \approx (1 - \mathrm{e}^{-\frac{w_0^2 \omega^2}{4}}) R_{n=1} \left[\omega\omega'(1 - \cos(\phi)) \right], \quad (4.19)$$

where $\mathcal{E}_0/\omega = \mathfrak{a}_0$ was used. Moreover, the relation

$$TA = \frac{\tau}{2} \sqrt{\frac{\pi}{\ln(2)}} \frac{\pi w_0^2}{2} \quad (4.20)$$

resulting from the energy consideration of the Gaussian pulse given in appendix C.2 was incorporated in order to derive the expression above. Lastly, as for an x-ray laser, which belongs to the laser class that produce photons with sufficiently high energy and is proposed as a photon source in the discussed setup, the wave length is much smaller than the beam waist $w_0 \gg 1/\omega$, the exponential factor in the expression above may be ignored.

4.2.3 Estimated number of created pairs

In this subsection an average number of created linear Breit-Wheeler pairs per incident bremsstrahlung electron will be provided applying the procedure outlined above. To that end, one multiplies the particle rate per volume that combines Eqs. (4.5) and (4.19) with the laser pulse duration τ and interaction volume V

$$\mathcal{N} = \tau V R_\gamma. \quad (4.21)$$

While the pulse duration can be read of straightforwardly from the experimental parameters, the interaction volume would be approximated by the focal area of the laser beam in the focal plane $A = w_0^2 \pi$ multiplied with the effective longitudinal extension of the pulse. The latter is taken as doubled Rayleigh length $2z_R$. Next, the wide spreading of the bremsstrahlung beam from Eq. (4.8) needs to be taken into

account. In the considered framework it coincides with the photon quantisation volume V_γ from Eq. (3.22). For the scheme of overlapping volumes the reader is referred to Fig. 4.3. Thus, the number of created pairs per incident electron with the Mandelstam variable $s = \sqrt{\frac{\omega E_0 f(1-\cos(\phi))}{2m^2}}$ reads

$$\mathcal{N} \approx \frac{\tau w_0^2}{(L_{e^-}\theta_{e^-} + L\theta_{\rm rms})^2} \frac{\alpha\xi^2 m^2}{4E_0} \int_0^1 \frac{df}{f} I_\gamma(f,l) \times \left[\frac{-s\sqrt{s^2-1}(1+s^2)}{s^4} + \frac{(-1+2(s^2+s^4))\ln(s+\sqrt{s^2-1})}{s^4} \right]. \quad (4.22)$$

Before proceeding with the numerical results, a discussion on possible experimental parameters is needed. As it was indicated at the beginning of this chapter, a suitable approach for electron acceleration is represented by the rapidly evolving field of LWFA, which enables production of several-GeV electrons in relatively compact experimental setups when using a sub-petawatt-class laser [70]. The latter can be provided, for example, within the HiBEF project at the European XFEL [71]. In this subsection electron energies in the range of 40 MeV to 4 GeV will be covered.

Moreover, the laser frequencies considered here will lie in the domain from soft to hard x-rays ($0.3-10$ keV). This choice in combination with the selected incident electron energies ensures that bremsstrahlung photons with energies falling below 20% of E_0, i.e. $f \lesssim 0.2$, will not be able to participate in the process. Indeed, the lower bound of integration for such scenario reads $f_{\rm min} = \frac{2m^2}{\omega E_0(1-\cos(\phi))}$ and the inaccuracy of Eqs. (4.6) and (4.7) at small f is mitigated. A possible source of soft x-ray laser pulses of 0.3 keV photon energy could be the FLASH facility at DESY in Hamburg, where photons with wavelength between $4.2-52$ nm can be generated. Additionally, hard x-ray laser pulses with photon energies of 10 keV and higher can

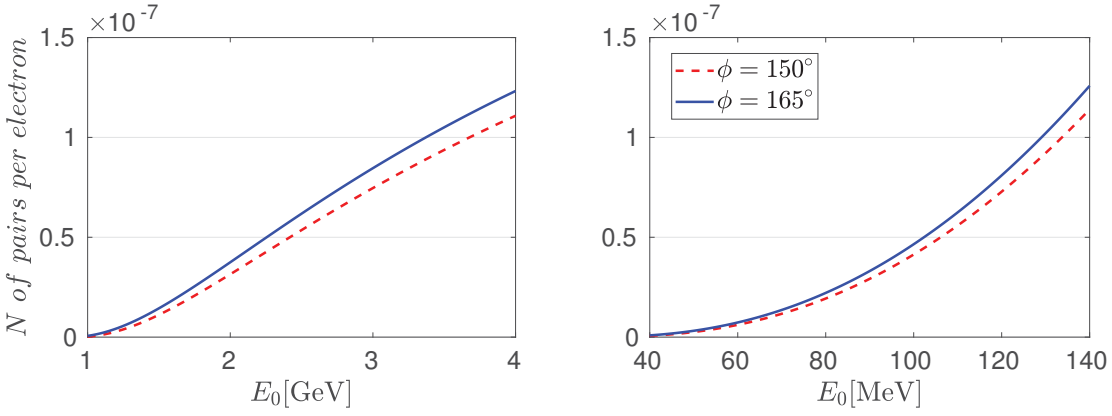

Figure 4.4: Number of pairs in dependence on the initial electron energy for $\xi = 0.001$, $\tau = 100$ fs, $w_0 = 20$ μm, $L = 0.5$ m and $\ell = 1.25$ (corresponding to $L_T = 7$ mm for lead target) and different collision angles ϕ. Here, the laser frequencies are set to $\omega = 0.3$ keV(left panel) and $\omega = 10$ keV (right panel).

be currently found at the European XFEL at DESY and the LCLS at Stanford [72]. Thus, all experimental constituents needed for the proposed setup are, in principle, available at DESY in Hamburg.

Next, numerical estimations of the number of created pairs are provided. To that end, the value of the laser field strength parameter is set to $\xi = 0.001$ throughout this section. It corresponds to an intensity of $I \approx 8 \times 10^{16}$ W/cm^2 at $\omega = 0.3$ keV and $I \approx 9 \times 10^{19}$ W/cm^2 at $\omega = 10$ keV.

In Fig. 4.4 it is shown how the number of created Breit-Wheeler pairs per incident bremsstrahlung electron depends on the beam energy E_0. Here, two different configurations are considered. Firstly, in the left panel a collision of a soft x-ray laser pulse ($\omega = 300$ eV) with bremsstrahlung emitted from $1 - 4$ GeV electrons is studied. Secondly, in the right panel it is assumed that the pairs are created as a result of a collision between an XFEL pulse of 10 keV photon energy and bremsstrahlung from $40 - 140$ MeV incident electrons. Moreover, in order to avoid damage of experimental equipment which could result from head-on geometry two collision angles $\phi = 150°$ (depicted in red dashed) and $\phi = 165°$ (blue solid) are employed (see Fig. 4.1). It can be seen that in the considered energy ranges the number of pairs for both setups is similar and grows with increasing E_0. A comparable particle yield for the two parameter sets rests on the fact that the product $E_0\omega$ is about the same for both configurations. Since lower energetic photon beam can be produced at smaller intensity when keeping ξ constant, the values $E_0 = 4$ GeV and $\omega = 0.3$ keV will be taken in the further discussion. For the chosen parameters electron bunches accelerated in the framework of LWFA can contain charges of several 100 pico-Coulomb up to a nano-Coulomb [56, 57]. When taking a moderate value of 10 pico-Coulomb and assuming that every electron emits a bremsstrahlung photon (which is realistic since thick targets with $\ell > 1$ are considered) up to 8 pairs can be generated per shot with experimental equipment available today or in the near future.

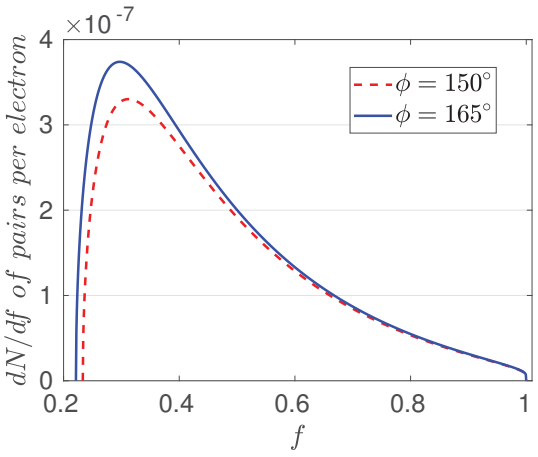

Figure 4.5: Differential number of pairs resulting from different bremsstrahlung photon frequencies for $\ell = 1.25$, $E_0 = 4$ GeV, $\xi = 0.001$, $\omega = 0.3$ keV, $\tau = 100$ fs, $w_0 = 20$ μm, $L = 0.5$ m.

The impact of different bremsstrahlung frequencies on the number of created pairs is examined with incident electron energy of $E_0 = 4$ GeV for $\phi = 165°$ (blue solid) and $\phi = 150°$ (red dashed) in Fig. 4.5. Both curves quickly grow at small f, manifest a maximum at the spectral region around $\omega' \approx 0.3E_0$ and fall afterwards. This behaviour is a result of an interplay of the monotonically growing part of

the integrand in Eq. (4.22) that solely depends on s, the factor $1/(E_0 f)$ and the fact that the number of bremsstrahlung photons falls when their energy rises (see Fig. 4.2). Moreover, the maximum of the red curve is slightly shifted to the right when compared to the blue curve. This misalignment represents a manifestation of the ϕ-dependence of the threshold energy $\sim [1-\cos(\phi)]^{-1}$ as, with smaller ϕ, a photon must posses a higher ω' in order to overcome this barrier and participate in the pair production.

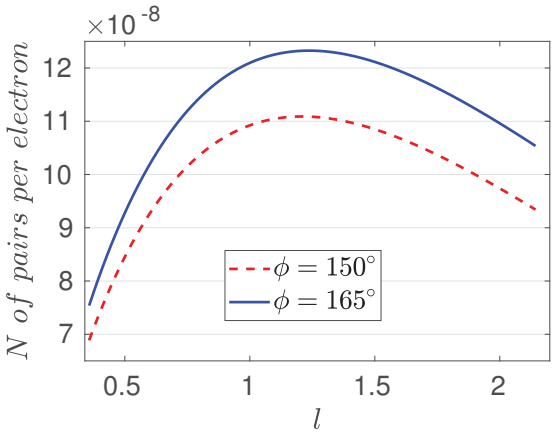

Figure 4.6: Number of created pairs in dependence on the normalised target thickness ℓ for $E_0 = 4$ GeV, $\xi = 0.001$, $\omega = 0.3$ keV, $\tau = 100$ fs, $w_0 = 20$ μm, $L = 0.5$ m.

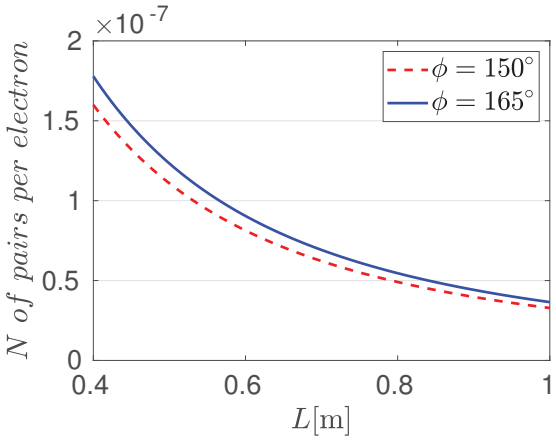

Figure 4.7: Number of created pairs in dependence on the distance L between the solid target and the laser focus. Here, the parameters are set to $E_0 = 4$ GeV, $\xi = 0.001$, $\omega = 0.3$ keV, $\tau = 100$ fs, $w_0 = 20$ μm and $\ell = 1.25$.

Further, the relation between the thickness of the chosen target and the expected number of created positrons is illustrated in Fig. 4.6. A proposed material can be, for example, lead with Z= 82 and $L_{\text{rad}} = 5.6$ mm. Similarly to the figures above, the red dashed curve stands for $\phi = 165°$ geometry and the blue one denotes $\phi = 150°$. The latter show upward tendencies for $\ell \lesssim 1.25$ ($L_T \lesssim 7$ mm for lead), reach their maximum and decline afterwards. This behaviour reflects a growing probability for the bremsstrahlung emission when the incident electrons travel longer through the target on the one side, and the fact that the emitted photons can be scattered or reabsorbed on the other. The probability of these disruptive processes increases with target thickness as well. Thus, before photon losses start to dominate, a maximum occurs.

When the optimal parameters $E_0 = 4$ GeV and $\ell = 1.25$ are chosen, Fig. 4.7 elucidates the importance of keeping the distance between the laser focus and the solid target as small as possible since the number of pairs decreases with growing L. The trend of the depicted curves coincides with the L^{-2} factor in Eq. (4.22) and represents the effect of decreasing bremsstrahlung photon density in the interaction volume as it was discussed in subsection 4.1.3 (see

Fig. 4.3).

From Eq. (4.19) and the discussion below it a conclusion was drawn that the effect of laser focusing is negligible for an x-ray laser. This statement is also supported when a closer look at Eq. (4.22) is taken: the number of created pairs is quadratic in both the beam waist w_0 and the parameter ξ. Thus, the process depends linearly on the laser intensity and, following Eq. (C.7), only on the total laser energy.

Lastly, let us put the found results in context of predicted pair yields provided by similar setups. As it was indicated earlier, for optimal parameters of the present study and electron bunches of 100 pC to ≈ 1 nC a detection of $\approx 80 - 800$ Breit-Wheeler pairs per shot is possible. This number is comparable with the total amount of positrons detected in the pioneering SLAC experiment [6, 7]. In the study of linear Breit-Wheeler pair production in Ref. [12], where bremsstrahlung photons collide with the hohlraum radiation, up to 10^5 pairs were obtained for 10^9 incident electrons (approximately 150 pC). The higher pair yield may be attributed to the larger interaction volume as it was not restricted to the focal area of the laser beam but rather dictated by the radiation-filled hohlraum. In Refs. [19, 73] investigations of the weakly nonlinear regime $\xi \gtrapprox 1$ of Breit-Wheeler pair creation occurring as a result of bremsstrahlung-laser interaction were presented. Both studies take into account highly energetic electron bunches of $E_0 = 17.5$ GeV consisting of 1.5×10^9 and 6×10^9 particles that produce bremsstrahlung, correspondingly. In Ref. [19], where the focus was put on a realistic description of the experimental conditions at LUXE, the pair yields of 10^{-2} for $\xi = 1.2$ and up to 350 for $\xi = 6.5$ per shot with an optical laser ($\omega = 1.55$ eV) were predicted (see Table 5 in Ref. [19]). Additionally, the expected number of created pairs in Ref. [73], which relies on an asymptotic formula for the pair production in the considered regime, amounts to approximately $[10^{-2}, 10^6]$ for $\xi \in [0.7, 7]$ per laser shot.

4.3 Highly nonlinear nonperturbative regime

The present section is devoted to the calculation of the predicted number of created Breit-Wheeler pairs in the highly nonlinear nonperturbative regime in a setup, where an optical laser interacts with highly energetic bremsstrahlung photons (see Fig. 4.1). This experimental endeavour was introduced in Ref. [33], where a proposal to test the Breit-Wheeler process in the $\xi \gg 1$, $\kappa \gtrsim 1$ regime at CALA was put forward and first estimations of the particle yield based on a plane wave pulse modelling of the laser field were given. Here, special interest lies on the effect of transversal and longitudinal laser focusing as high intensities, which are characteristic for the studied parameters, can be achieved solely in tightly focused laser beams. Due to the considered parameters ($\xi \gg 1$) and incorporation of focusing into the field description neither a perturbative treatment nor an approach involving Volkov solutions comes into question. Hence, a locally constant field approximation (LCFA) framework is applied, which is introduced in the following subsection, and resulting estimations for parameters envisaged in Ref. [33] are presented. The results shown in this section were initially published in Ref. [51].

4.3.1 Locally constant field approximation

Under the condition $\xi \gg 1$ [7] the characteristic length of Breit-Wheeler pair formation $l \sim \lambda/(\xi\pi)$ is much smaller than the laser wave length $\lambda = 2\pi/\omega$. Hence, particles when being created do not feel the field oscillations and the laser background can be treated locally as a constant crossed field introduced in the section 3.2. Following Ref. [74], this approximation is applicable for low laser frequencies $\omega \ll m$ and values of ξ starting from $\xi \gtrsim 5$. Consequently, the number of created electron-positron pairs per unit of volume and time produced by an incident bremsstrahlung electron is approximated by (see Refs.[75, 76] combined with Eq (4.5)):

$$\left.\frac{dN}{dtdV}\right|_{\xi(\boldsymbol{x},t)\gg 1} \approx F_\gamma(\kappa)|_{\xi\to\xi(\boldsymbol{x},t)}\,. \tag{4.23}$$

In general, $F_\gamma(\kappa)$ is the unpolarised transition rate per volume of the pair production process in a constant crossed field from Eq. (3.39) averaged over the energy of the bremssstrahlung photon as it was shown in Eq. (4.5). For the context of the present section, a parameter region $\xi \gg 1$, $\kappa \approx 1$ is relevant. Thus, instead of the rate from Eq. (3.39) the approximative expression $F_{\kappa\approx 1}$ from Eq. (3.44) will be used hereafter.

[7] As the electromagnetic field of the laser is oscillating, alongside with $\xi \gg 1$ regions there are contributions to the particle creation stemming from small and moderate intensity parameters. In Fig. 4.8 the osillating values of ξ are presented. However, following Eq. (3.16) and Ref. [55], the latter have much smaller impact than the high intensity domain. Thus, an assumption is made that the production process is dominated by the spacetime regions, in which the strong field condition $\xi(\boldsymbol{x},t) \gg 1$ holds.

To that end, an estimated number of pairs reads

$$N \approx \int_\Gamma dtdV \int_0^1 df \; I_\gamma F_{\kappa\approx 1}(\kappa)|_{\xi\to\xi(\boldsymbol{x},t)} \tag{4.24}$$

with the bremsstrahlung photon spectrum I_γ from Eqs. (4.6) and (4.7) and Γ denoting the spacetime integration volume.

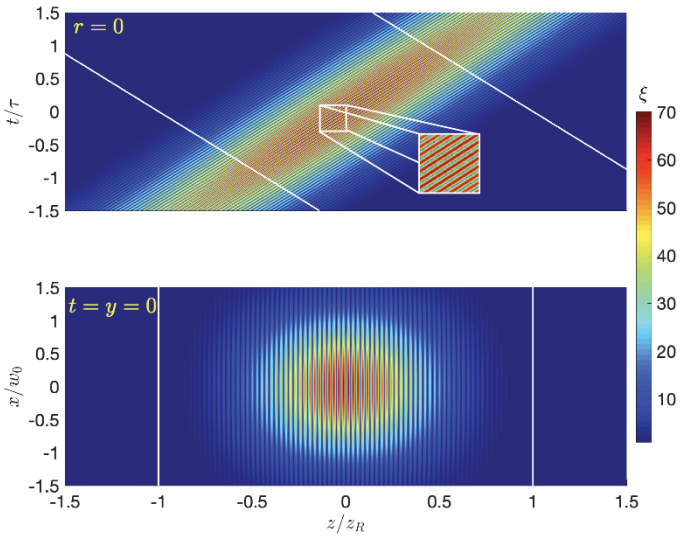

Figure 4.8: Laser intensity parameter for a Gaussian pulse with $\omega = 1.55$ eV and maximal intensity of $I_0 = 10^{22}$ W/cm^2. The region between white lines corresponds to the area, where bremsstrahlung with longitudinal extension $2z_R$ exists.

Strictly speaking, Γ is dictated by the regions where $\xi(\boldsymbol{x},t) \gg 1$ holds and where the bremsstrahlung photons are propagating. However, as it was pointed out in the footnote 7, due to the oscillating nature of the electromagnetic field and the fact that the contributions stemming from moderate and small intensity parameters are negligible, the integration region may be extended to the part of the spacetime where the laser and the bremsstrahlung pulses overlap. For a counter-propagating geometry, i.e. $\phi = 180°$, the longitudinal extension of the bremsstrahlung bunch is given by [8]

$$\frac{1}{2}\omega'\sigma_z \leq k'x \leq \frac{1}{2}\omega'\sigma_z, \tag{4.25}$$

which translates to

$$z_\pm = -t \pm \frac{1}{2}\sigma_z. \tag{4.26}$$

For a Gaussian pulse in a paraxial approximation from Eq. (4.1), the color scheme in Fig. 4.8 shows the values of $\xi(t,\boldsymbol{x})$ for $\omega = 1.55$ eV and maximal intensity of $I_0 = 10^{22}$ W/cm^2, which will be used as benchmark parameters hereafter. In this context, the region where the bremsstrahlung with longitudinal extension $\sigma_z = 2z_R$ propagates is enclosed between the white solid lines. Thus, it can be seen that the high intensity zones, which provide the major contribution to the pair creation process, are located almost completely within the bremsstrahlung area for the chosen parameter set. Moreover, transversal bremsstrahlung boundaries may be extended

[8] For geometries other than head-on the longitudinal extension of the bremsstrahlung will depend on the collision angle and r (see comment on this issue in the last paragraph on page 38 and Eq. (4.36)). However, the majority of the results relevant for this section will rely on $\phi = 180°$.

to $\pm\infty$ as the field strength decays fast for $r/w_0 \gtrsim 1$. Having these details in mind, the expected number of created pairs for a paraxial Gaussian pulse in cylindrical coordinates can be expressed as

$$N \approx 2\pi \int_{-\infty}^{\infty} dt \int_0^{\infty} r dr \int_{-t-\frac{1}{2}\sigma_z}^{-t+\frac{1}{2}\sigma_z} dz \int_0^1 df \; I_\gamma \; F_{\kappa\approx 1}(\kappa)|_{\kappa\to\kappa(\boldsymbol{x},t)}. \tag{4.27}$$

Hence, effectively, a transition from a constant to a space dependent quantum nonlinearity parameter is made, which is discussed in detail in the next subsection for all considered field models. Additionally, when the Gaussian pulse beyond the paraxial approximation is taken into account, the cylindrical symmetry of the laser pulse is broken through nontrivial dependences on the azimuthal angle (see Eqs. (C.11) and (C.12) in appendix C.3) and the factor 2π in the expression above has to be replaced by a corresponding integration.

Next, a pulsed plane wave with a Gaussian envelope depending only on the phase φ (see Eq. (C.8) in appendix C.2) is considered. This model is formulated conveniently via light-cone coordinates [77, 78]

$$x_\pm = \frac{1}{\sqrt{2}}(t \pm z), \; \boldsymbol{x}_\perp = (x, y). \tag{4.28}$$

For the present thesis only a head-on collision with $\phi = 180°$ is relevant for this field model. In this framework the laser phase reads

$$\varphi = k_+ x_- \text{ with } k_+ = \frac{1}{\sqrt{2}}(k^0 + k^3) = \sqrt{2}k_0 \tag{4.29}$$

and $kk' = k_+k'_-$ holds, whereas the phase of the gamma quantum is equal to $\varphi' = k'x = k'_-x_+$. Then, a substitution $t \to \varphi'$, $z \to \varphi$ is performed

$$\lim_{T\to\infty} \int_{-T/2}^{T/2} dt \int_{-t-\frac{1}{2}\sigma_z}^{-t+\frac{1}{2}\sigma_z} dz \int_{A_{\text{int}}} d\boldsymbol{x}_\perp \; ... = \lim_{T\to\infty} \frac{A_{\text{int}}}{k_+k'_-} \Delta\varphi' \int_{-\Delta\varphi/2}^{\Delta\varphi/2} d\varphi \; ... \tag{4.30}$$

and with $\Delta\varphi' = \omega'\sigma_z$, $\Delta\varphi = 2\omega T$ one obtains

$$N \approx \frac{\omega'}{k_+k'_-} V_{\text{int}} \int_{-\infty}^{\infty} d\varphi \int_0^1 df \; I_\gamma \; F_{\kappa\approx 1}(\kappa)|_{\kappa\to\kappa(\varphi)}. \tag{4.31}$$

Here, in order to provide a fair comparison between different schemes for describing the laser, the pulse energy in every model will be kept equal. To that end, the interaction volume turns out to be[9] $V_{\text{int}} = A_{\text{int}}\sigma_z$ with A_{int} given below Eq. (C.9). Now, since $F_{\kappa\approx 1}$ depends inversely on the spreading volume of the bremsstrahlung from Eq. (4.8), a factor $V_{\text{int}}/V_\gamma \approx w_0^2/(2\bar{r}^2)$ occurs. This ratio stands for the fraction of the bremsstrahlung photons interacting with the laser pulse and for the parameters

[9] When a setup geometry other than counterpropagating is considered, the interaction volume will depend on the collision angle ϕ.

assumed in the numerical calculation of the number of pairs shown in the next subsections it amounts to $\approx 2\times10^{-5}$. Thus, similarly to the previous section, spreading of the bremsstrahlung beam represents a crucial problem for the discussed class of experiments.

A comment is in order: when $V_{\rm int}$ and V_γ coincide, no averaging over the spectrum of bremsstrahlung is performed and Eq. (3.39) is used instead of the approximative rate, the expression in Eq. (4.31) agrees with the probability for particle creation resulting from Eq. (33) of Ref. [79]. The latter was derived from the imaginary part of the vacuum polarisation tensor in a plane-wave background via the optical theorem.

Finally, a constant crossed field $\mathcal{E}_x(\varphi)=\mathcal{E}_0\Theta(\frac{1}{2}\Delta\varphi-\varphi)\Theta(\varphi+\frac{1}{2}\Delta\varphi)$ in a finite spacetime volume is considered. For this model, when keeping the laser field energy equal to the cases described previously, the expected number of particles reads

$$N\approx T_{\rm int}V_{\rm int}\int_0^1 df\ I_\gamma\ F_{\kappa\approx1}(\kappa) \tag{4.32}$$

with $\Delta\varphi=2\omega T_{\rm int}$ and $T_{\rm int}=\frac{\tau}{2}\sqrt{\frac{\pi}{\ln(2)}}$ given below Eq. (C.10).

4.3.2 Time and space dependent κ

In order to provide the spacetime dependent quantum nonlinearity parameter as needed for LCFA, the former is expressed in terms of the electromagnetic field tensor $f_{\mu\nu}$ as $\kappa=|e|\sqrt{-(f_{\mu\nu}k'^\nu)^2}/m^3$. To that end, when no particular choice of the laser field description is made, one generally obtains

$$\begin{aligned}\kappa=\frac{|e|\omega'\mathcal{E}_0}{m^3}\Bigg[&\left(\frac{\mathcal{B}_z}{\mathcal{E}_0}\sin(\phi)+\frac{\mathcal{B}_y}{\mathcal{E}_0}\cos(\phi)\right)^2+\left(\frac{\mathcal{E}_x}{\mathcal{E}_0}\right)^2+\left(\frac{\mathcal{E}_y}{\mathcal{E}_0}\right)^2+\left(\frac{\mathcal{E}_z}{\mathcal{E}_0}\right)^2\\&-\left(\frac{\mathcal{E}_y}{\mathcal{E}_0}\sin(\phi)+\frac{\mathcal{E}_z}{\mathcal{E}_0}\cos(\phi)\right)^2+2\frac{\mathcal{B}_x}{\mathcal{E}_0}\left(\frac{\mathcal{E}_y}{\mathcal{E}_0}\cos(\phi)-\frac{\mathcal{E}_z}{\mathcal{E}_0}\sin(\phi)\right)\\&+\left(\frac{\mathcal{B}_x}{\mathcal{E}_0}\right)^2+2\frac{\mathcal{E}_x}{\mathcal{E}_0}\left(\frac{\mathcal{B}_z}{\mathcal{E}_0}\sin(\phi)-\frac{\mathcal{B}_y}{\mathcal{E}_0}\cos(\phi)\right)\Bigg]^{1/2}\end{aligned} \tag{4.33}$$

with the electric and magnetic field components $\mathcal{E}_i$ and $\mathcal{B}_i$, respectively, and an assumed geometry, where strong laser pulse propagates with the wave vector $\boldsymbol{k}=\omega\boldsymbol{e}_z$ as well as ϕ denotes the collision angle (see Fig. 4.1). Thus, in order to calculate the particle number from Eq. (4.27) for a paraxial Gaussian pulse, the nonvanishing field components $\mathcal{E}_x=\mathcal{B}_y$ from Eq. (4.1) are to insert in the expression above and one ends up with

$$\kappa(t,\boldsymbol{x})=\frac{|e|\omega'\left[1-\cos(\phi)\right]}{m^3}|\mathcal{E}_x(t,\boldsymbol{x})|. \tag{4.34}$$

The black solid curve in Fig. 4.9 shows the local values of κ in dependence on the longitudinal coordinate z for such a scenario, whereas the red dashed one accounts

for the case where the terms describing longitudinal laser focusing are neglected. Moreover, $r = 0$ and $t = 0$ were set and parameters from the table 4.1 were used. Thus, it can be seen that the values of κ relevant for the present section encompass the interval between 0 and roughly 2 providing a justification for the usage of the approximated rate $F_{\kappa\approx1}$ given in Eq. (3.44).

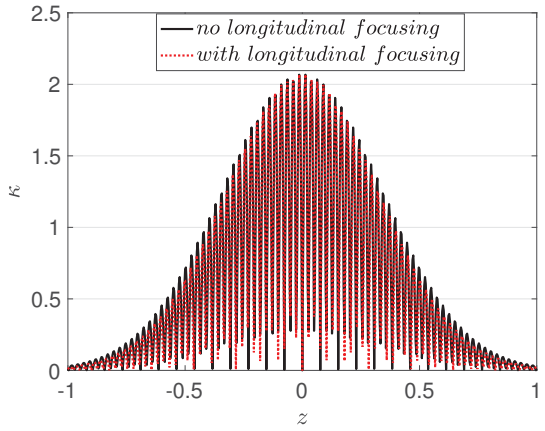

Figure 4.9: Quantum nonlinearity parameter κ for Gaussian pulses with (red dotted) and without (black solid) longitudinal focusing at $t = 0$, $r = 0$. This figure was initially published in Ref. [51].

Additionally, in a pulsed plane-wave background from Eq. (C.8) the phase dependent quantum nonlinearity parameter reads

$$\kappa(\varphi) = \kappa|\psi(\varphi)| \tag{4.35}$$

with the monochromatic plane-wave value $\kappa = \omega\omega'[1 - \cos(\phi)]\xi/m^2$ and the function $\psi(\varphi)$ from Eq. (C.8).

4.3.3 Comparison of different field models

In this and the following subsections numerically evaluated estimations for the number of created pairs by an incident radiating bremsstrahlung electron based on the LCFA framework are presented. Unless stated otherwise, the benchmark parameters from Ref. [33], which are listed in the table 4.1, counterpropagating geometry ($\phi = 180°$) and a conservative value of $\sigma_z = 2z_R$ are taken. The latter facilitates good synchronisation between the interacting laser and bremsstrahlung beams. Moreover, a very thin tungsten target ($L_{\text{rad}} = 3.5$ mm) with $\ell = 0.015$ is utilised in order to optimise the signal to noise ratio (for further details see section 5 in Ref. [33]).

The starting point is a comparison between the different laser models, which were presented above. To that end, in Fig. 4.10 the dependence of the number of created pairs on the bremsstrahlung photon energy is analysed. The green dotted curve represents a description of a laser, where a constant crossed field (CCF) is contained in the finite spacetime volume $V_{\text{int}}T_{\text{int}}$ and has the same energy as the paraxial Gaussian laser pulse, combined with the asymptotic formula for the creation rate $F_{\kappa\approx1}$, i.e. Eq. (4.32) is implemented. For generation of the blue dashed curve the exact rate F from Eq. (3.39) was taken instead. As both curves lie tightly by each other, applicability of the approximative expression is supported and, thus, the latter is used in other models as well. Next, the black curve provides estimations for dN/df when modelling the laser field as a pulsed plane wave with a Gaussian envelope enclosed in a spatial volume V_{int} following Eq. (4.31). This description

Incident electron energy E_0	2.5 GeV
Distance travelled by the bunch L_{e^-}	0.1 m
Incident electrons collimation angle θ_{e^-}	0.5 mrad
Normalised target thickness ℓ	0.015
Distance travelled by bremsstrahlung L	0.5 m
Wavelength of the strong pulse λ	0.8 μm
Pulse waist size w_0	2 μm
Pulse length τ	30 fs
Laser intensity parameter ξ	70
Laser repetition rate	0.1 Hz

Table 4.1: Parameters envisaged in the experiment planned at CALA, which were provided in Ref. [33]. These values are adopted hereafter.

was also implemented in Ref. [33]. Lastly, the red curves were generated under the assumption that paraxial Gaussian pulses describe the laser fields and rely on Eq. (4.27). From Fig. 4.10 it can be seen that all curves show an upward trend meaning that the particle yield increases as the energy of bremsstrahlung photons grows. Whereas the most optimistic prediction is provided by CCF, the more realistic descriptions incorporating finite laser duration and laser focusing reduce the expected pair number by factors of about 5 and 10, correspondingly.

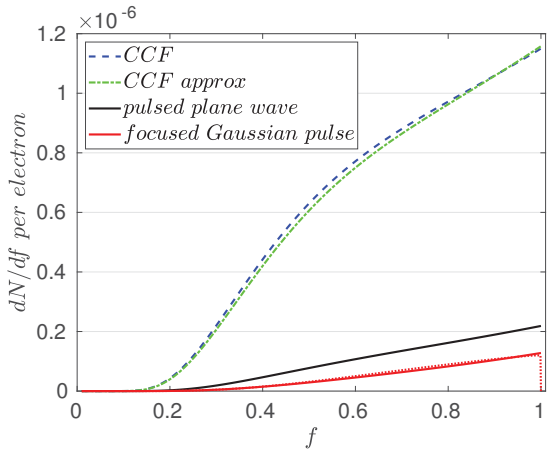

Figure 4.10: Differential number of pairs in dependence on the normalised bremsstrahlung energy $f = \omega'/E_0$ for $\xi = 70$. This figure relies on the benchmark parameters from table 4.1 and was initially published in Ref. [51].

Following the fact that the energy of γ photons, which were emitted by bremsstrahlung electrons, can not exceed E_0 and, accordingly, no pairs can be created at $f \geq 1$, all curves should fall sharply to zero after a maximum at $f \approx 1$ (see Fig. 4.2 and Refs. [32] and [62]). The decay is absent owing to implementation of the bremsstrahlung spectra from Eq. (4.6) for I_γ for generation of all curves except the red dotted one, which results when the thick target approximation in Eq. (4.7) is applied and a focused Gaussian pulse model is adopted. In this section very thin targets with $\ell = 0.015$ are considered. Thus, due to the close overlapping of red curves and negligible contribution from the low energy range $f \in [0, 0.2]$, the approximation in Eq. (4.6) represents a good description of the bremsstrahlung spectrum and will be used in the following calculations.

Further, the estimated number of created pairs per incident electron depending on the underlying field description (blue dashed for CCF, black solid for pulsed plane wave and red for focused Gaussian pulse) is presented in Fig. 4.11 as a function of the intensity parameter ξ. Here, a red dotted curve has been included, which results from a collision geometry planned in the experiment described in Ref. [33] with $\phi = 162°$. In order to describe geometries other than head-on a rotation of the integration region depicted in Fig. 4.8 needs to be performed. To that end, the longitudinal extension of the bremsstrahlung radiation translates into the following limits in z:

$$z_\pm = -(t \mp \frac{1}{2}\sigma_z)\frac{1}{|\cos(\phi)|} + r|\tan(\phi)|, \tag{4.36}$$

where the last term may be neglected as long as the longitudinal extension of the bremsstrahlung beam is larger than the laser pulse length. However, the outlined procedure represents a good approximation only whenever a collision geometry close to a counterpropagating one is considered.

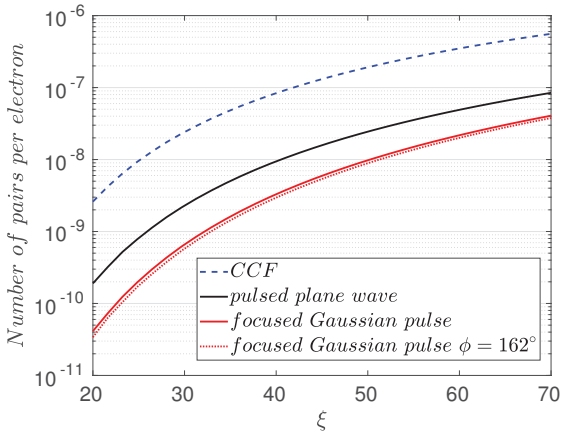

Figure 4.11: Number of created pairs depending on the modelling of the strong field and the intensity parameter ξ. This figure relies on the benchmark parameters from table 4.1 and was initially published in Ref. [51].

Similarly to Fig. 4.10, Fig. 4.11 shows that realistic description of the laser pulse modifies the expected yield by lowering it. As the pulse energy is kept equal for all models, this reduction is grounded solely on the underlying laser field configuration. While for CCF the intensity is kept high and constant within the whole interaction spacetime volume $V_{\text{int}}T_{\text{int}}$, the field intensity linked to a Gaussian profile changes from its maximum at the center of the interaction volume to the minimal values at its edges as it is shown in Fig. 4.8. Evidently, this intensity gradient has a significant impact on the pair creation yield and, thus, will be closely studied in the subsequent subsections.

Next, the predicted number of pairs for $\xi = 70$ (corresponding to the intensity of $I \approx 10^{22}$ W/cm^2) when modelling the laser as a focused Gaussian pulse will be analysed. In this scenario the yield of created positrons per incident radiating electron in a single laser shot is 4×10^{-8}. As it was already pointed out in section 4.2, the currently available experimental techniques (such as laser wakefield acceleration) can generate electron bunches with up to ≈ 1 nC of total charge [56, 57]. In Ref. [33] a production of several pC accelerated electron bunches with $E_0 = 2.5$ GeV is expected. Thus, an estimation for a 10 pC electron appears realistic providing ≈ 0.03 pairs per laser shot, when an assumption relying on GEANT4 simulations

in Ref. [33] is made that only 1% of incident electrons will emit a bremsstrahlung photon. Hence, when taking into account a laser repetition rate of 0.1 Hz, a creation of 10 Breit-Wheeler pairs is expected per hour. It appears less than the 80 pairs per hour estimated in Ref. [33], a prediction made when describing the laser field as a pulsed plane wave. Thus, the more realistic modelling of the strong field by incorporation of focusing leads to significant changes in the predicted pair yields. Besides, in comparison to a particle yield reported in Ref. [32], where a similar setup was studied and for $\xi = 30$ up to 10^4 pairs per laser shot and a pC of 2 GeV incident electrons were estimated, the outcome of the present study turns out to be quite small. This mismatch is presumably based on the fact that in Ref. [32] the divergence of the bremsstrahlung ray was not taken into account as an assumption was made that the latter can be counteracted by focusing the incident electron bunch. Here, however, as it was pointed out previously, the bremsstrahlung spreading plays a crucial role and reduces the particle yield by a factor $V_{\text{int}}/V_\gamma \sim 10^{-5}$.

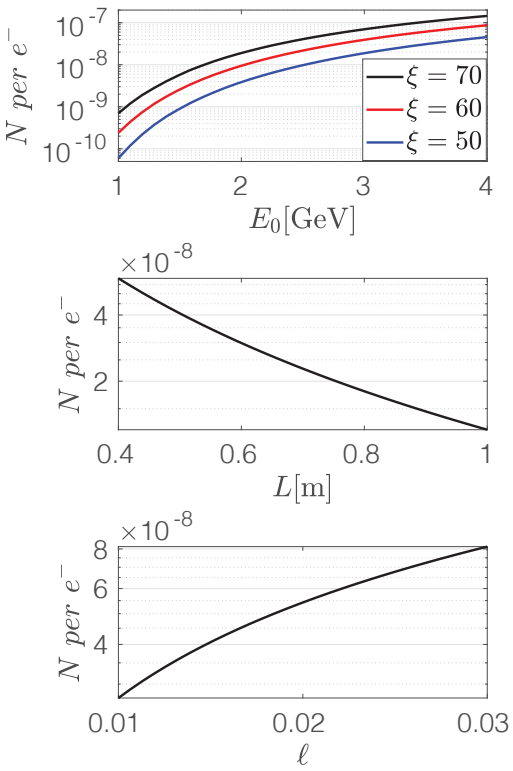

Figure 4.12: Number of created pairs per incident electron in dependence on incident electron energy (upper panel), distance between the bremsstrahlung target and focal point (middle panel) and target thickness (lower panel). The other parameters are taken from table 4.1.

Before going over to the thorough study of the focusing effects, an outlook on setup parameters beyond the scope of Ref. [33] is provided. Here, the laser field is modelled as a focused Gaussian pulse in paraxial approximation. To that end, in the upper panel of Fig. 4.12 the dependence of the pair yield on the energy of the incident electrons and the intensity parameters $\xi = 70$, $\xi = 60$, $\xi = 50$ is presented in black, red and blue colors, respectively. As the curves show a strong positive trend, when possible, the parameter E_0 should be maximised. Moreover, observe that the increase in the number of created particles is the fastest in the region of low energy and for the lowest intensity. Next, in the middle panel the dependence on the distance L between the high-Z target and the interaction point (see setup scheme in Figs. 4.1 and 4.3) is studied. Since the spreading of the bremsstrahlung beam is more pronounced for larger L, the curve has an expected falling behaviour. Despite this trend, L should be chosen sufficiently large to provide enough distance for the effi-

cient deflection of the incident electrons. Lastly, the expected number of created pairs as a function of the normalised target thickness ℓ is depicted in the lower panel of Fig. 4.12. The rising tendency of the curve can be explained by the fact that the probability of electrons to emit a bremsstrahlung photon increases when its path through the high-Z material is prolonged. Here, a special attention needs to be paid to the fact that the probability of noise processes in the bremsstrahlung target will grow as well and, thus, an optimal combination in the value ensemble of all three parameters E_0, L and ℓ is required (see discussion on this topic in Ref. [33]).

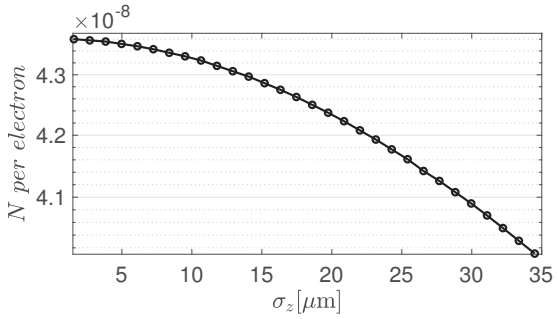

Figure 4.13: Dependence of the pair yield on the thickness of the bremsstrahlung bunch σ_z when the number of gamma photons in the pulse is kept constant. This figure relies on the benchmark parameters from table 4.1 and was initially published in Ref. [51].

In addition, when describing the laser as a focused Gaussian pulse from Eq. (4.1), Fig. 4.13 shows the dependence of the number of created pairs on the thickness of the bremsstrahlung burst σ_z. The negative trend of the curve is caused by the longitudinal focusing, which is incorporated in the laser description. It can be explained by the fact that, provided a good synchronisation between laser and bremsstrahlung beams is achieved, when the bremsstrahlung bunch is shorter than the laser focal region $2z_R$ more γ photons can experience the high intensity domain. Inversely, in broader γ bunches the photon density is diluted and fewer photons can interact with high intensity regions, which provide the most significant contribution to the pair creation process. Instead, they interact with the low intensity regions at the edges of the interaction volume, which do not have a sizeable impact on the particle production.

4.3.4 Contributions from different focal regions

Our approach to the Breit-Wheeler effect via the LCFA has a particular advantage: It allows us to gain spatially resolved insights into the production process. For this purpose, contributions to the number of pairs stemming from different focal regions are examined and exhibited in Fig. 4.14. The curves have been obtained when modelling the laser field as a paraxial Gaussian pulse and reordering the integrations from Eq. (4.27) in a way that the time integral is taken prior to the $z-$integration and runs in the limits

$$t_\pm = -z \pm \frac{1}{2}\sigma_z \tag{4.37}$$

for $z \in [-0.75, 0.75]z_R$, $z \in [-0.5, 0.5]z_R$, $z \in [-0.25, 0.25]z_R$, respectively, and the integration in f is not carried out. Thus, the fractions of the pair yield stemming

from these integration regions are denoted by the patterns in red filled circles, blue open boxes and green open circles, correspondingly. Fig. 4.14 shows that low energetic bremsstrahlung quanta provide the highest relative contribution from the innermost region. It happens because these γ photons can only provide a significant impact on the pair creation when they interact with the strong field domains with very high intensity. As it was revealed in Fig. 4.10, in general, the major contribution to the total number of pairs stems from high bremsstrahlung energies. Thus, the value $f \approx 1$ is discussed in more detail: while 52% of the created particles result from $|z| \leq 0.25 z_R$, the doubled region with $|z| \leq 0.5 z_R$ gives 94%, and practically 100% of the pair production is contained in $|z| \leq 0.75 z_R$.

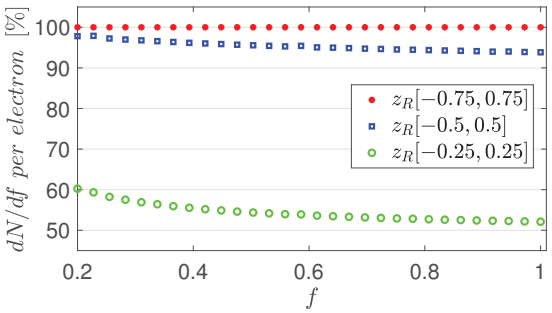

Figure 4.14: Differential number of pairs as a function of the bremsstrahlung photon energy for different focal regions with $\xi = 70$. This figure also relies on the benchmark parameters from table 4.1 and was initially published in Ref. [51].

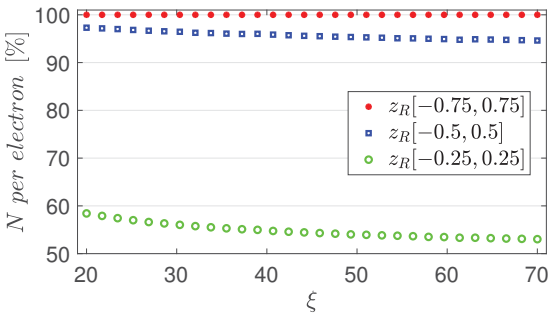

Figure 4.15: Percentage of created particles from different focal regions for a focused Gaussian pulse. This figure relies on the benchmark parameters from table 4.1 and was initially published in Ref. [51].

When in addition to the procedure described above an integration over the bremsstrahlung energy is performed, the percentage of the particles produced in different focal regions can be elucidated. Fig. 4.15 shows how the latter varies with changing laser intensity parameter ξ. The trend exhibited by the curves indicates that with the growing of ξ the importance of the outer zones increases as the high intensity region that facilitates the pair production is extended to the whole Rayleigh length. To be more precise, while the innermost region (green open circles) accounts for about 53% of created pairs for $\xi = 70$, its impact increases to about 58% when the intensity parameter is lowered to 20. This tendency results from the fact that, for rather low ξ, the local quantum nonlinearity parameter κ reaches values close to 1, which are required for a sizeable pair production, only in the inner focal region. Outside the latter, κ quickly falls far below unity and, accordingly, the pair production is suppressed. In contrast, when ξ is large, the local value of κ reaches sufficient level over a broader region, where the pair production can occur with significant probability. Note that the slope of the curves in Fig. 4.11 decreases with increasing ξ, so that local changes of the

field strength in a Gaussian pulse become less crucial when ξ is large.

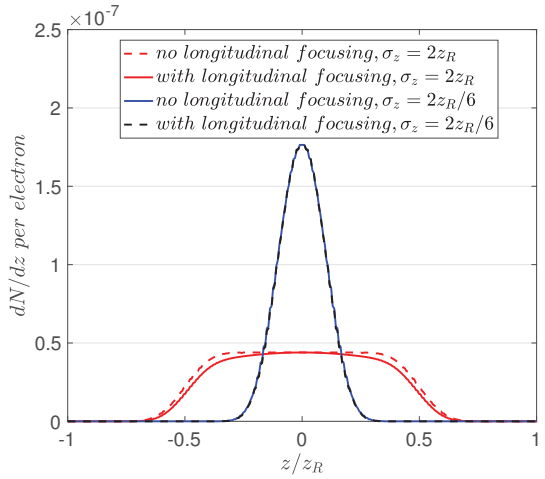

Figure 4.16: Distribution of created pairs in the longitudinal direction for $\xi = 70$. This figure also relies on the benchmark parameters from table 4.1 and was initially published in Ref. [51].

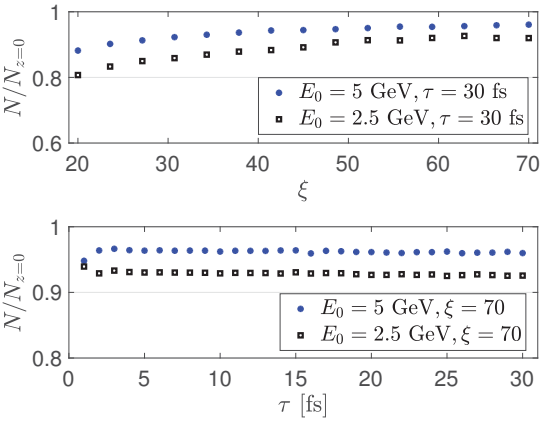

Figure 4.17: Dependence of the ratio between the number of produced pairs with (N) and without ($N_{z=0}$) longitudinal focusing on the intensity parameter ξ (upper panel) and the pulse length τ (lower panel). This figure relies on the benchmark parameters from table 4.1 and was initially published in Ref. [51].

Furthermore, in Fig. 4.16 a comparison of the distribution of created pairs along the longitudinal direction z with $\sigma_z = 2z_R$, which is depicted in red, and a shorter beam with $\sigma_z = 2z_R/6$ corresponding to black dashed and blue solid lines is shown. In both cases for the generation of the dashed curves the longitudinal focusing in the description of the laser field was ignored. It was achieved by omitting the dependences on $\zeta(z)$ in the paraxial field model in Eq. (4.1). Conversely, the solid curves incorporate this effect. Also here, the integration in t was limited as in Eq. (4.37). Observe that the deviations between corresponding curves can be seen solely for the case of broader bremsstrahlung bunches denoted by red curves and occur mainly outside the inner focal zone $z \in [-0.25, 0.25]z_R$. For shorter beams of bremsstrahlung the effect of the longitudinal focusing is absent as the interaction takes place almost exclusively in the innermost focal region, where the intensity gradient is comparably small (see Fig. 4.8). Moreover, the higher maximum of the blue curve as compared to the red one at $z = 0$ can be understood as a direct consequence of the smaller bremsstrahlung extension: due to the higher density the number of γ quanta that experiences the region of highest field strength is larger than in the case of a broader bunch.

4.3.5 Focusing effects

The importance of the incorporation of longitudinal focusing in the field description is presented in Fig. 4.17. The curves show the ratios between the number of produced pairs linked to the models with (N) and without ($N_{z=0}$) longitudinal focusing as functions of the intensity parameter in the upper panel and the pulse duration in the lower panel. The field description without longitudinal focusing is achieved, similarly to the case described above, when neglecting the field dependence on $\zeta(z)$ in Eq. (4.1). Here, the black and blue dotted patterns have been generated with $E_0 = 2.5$ GeV and $E_0 = 5$ GeV, correspondingly, while setting $\tau = 30$ fs in the upper panel and $\xi = 70$ in the lower panel. From the upper panel it can be seen that longitudinal focusing can be ignored when the laser intensity and electron energy are high: for $\xi = 70$ the relative error $1 - N/N_{z=0}$ amounts to $\sim 8\%$ for the lower energetic case and $\sim 4\%$ when the electron energy is 5 GeV. This fact can be explained by the dependence of the quantum nonlinearity parameter κ on the mentioned quantities. In the regions, where values of E_0 and ξ are large enough for κ to approach unity, the rate of pair production in CCF from Eq. (3.39) reaches a regime with less pronounced slope than in the case of exponential damping for $\kappa \ll 1$ (see Fig. 3.3). Thus, the rate is less sensitive to the gradient in κ caused by longitudinal focusing. Conversely, the curves in the lower panel of Fig. 4.17 show almost no variation for $\tau \gtrsim 3$ fs.

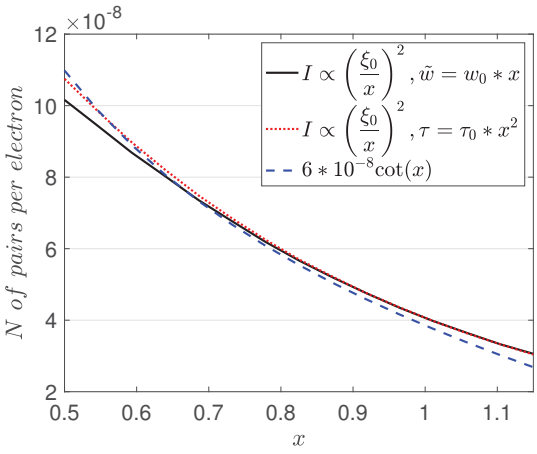

Figure 4.18: Number of created pairs when pulse energy is kept constant, while varying beam waist size and intensity. The reference values read $\xi_0 = 70$, $w_0 = 2$ μm and $\tau_0 = 30$ fs corresponding to $x = 1$. The remaining parameters are given in table 4.1. This figure was initially published in Ref. [51].

Further, an impact of tighter transversal focusing when keeping the laser pulse energy, which is given in Eq. (C.7) and is proportional to the laser intensity and beam waist $W_{\mathrm{G}} \propto I w_0^2$, constant is examined. Here, $I = \mathcal{E}_0^2/2$ stands for the average laser intensity. Thus, in this scenario a higher intensity I would demand proportionally stronger focusing, i.e. narrower beam and smaller w_0. This proportionality is achieved by introduction of a scaling factor x:

$$W_{\mathrm{G}} \propto \left(\frac{\xi_0}{x}\right)^2 (w_0 x)^2 = const. \tag{4.38}$$

Thus, if x grows, one obtains a beam with the same energy, but decreased intensity and broader focal point. Having this in mind and by figuring out the dependence of the number of created pairs on x an optimisation of the particle production can be achieved. Similarly, since $W_{\mathrm{G}} \propto I\tau$ the field ampli-

tude can be varied simultaneously with the pulse duration while keeping the pulse energy fixed.

The outcome of the discussion above while taking into account parameters $w_0 \in [1, 2.3]$ μm, $\tau \in [7.5, 40]$ fs and $I \in [0.86, 4.2] \times 10^{22}$ W/cm^2 is shown as black solid (altering transverse focusing) and red dotted (varying pulse duration) curves in Fig. 4.18. The smallest values of the beam waist and τ correspond to the highest intensity. Both graphs manifest a declining tendency with $N \propto \cot(x)$, a dependence found by curve fitting and depicted as blue dashed curve, with the maximal pair yield at the smallest considered value $x = 0.5$. Hence, in the present context achieving the highest possible intensity would benefit the pair creation more than increasing the spacetime volume of interaction and the volume quotient V_{int}/V_γ, which is associated with a huge negative impact, should be controlled by, for example, collimating the incident electron beam with a quadrupole magnet (decreasing θ_{e^-}) or via a faster deflection of electrons which have passed the high-Z target (decreasing L) and not by loose focusing. This result extends the outcome shown in Fig. 4 in Ref. [33], where laser focusing has not been considered and pair production was driven by a monoenergetic γ beam. The optimal intensity established there amounts to approximately $I \approx 10^{22}$ W/cm^2 for $\omega' = 2.5$ GeV and $\tilde{w} = 2$ μm. Finally, from Fig. 4.18 it can be seen that a consideration of longer pulses at the cost of smaller intensity does not benefit the production of pairs either.

Next, a similar procedure is applied on a setup where the energy of incident electrons is increased to $E_0 = 10$ GeV leading to a pronounced optimal combination of laser intensity and focal spot radius. The results of this study are exhibited in Fig. 4.19, where a maximum at $x \approx 0.9$ corresponding to $\xi \approx 120$ ($I \approx 3 \times 10^{22}$ W/cm^2) and $\tilde{w} \approx 0.9$ μm can be seen. Interestingly, in the region $x \lesssim 0.9$, where the laser field is more tightly focused and has increased intensity when compared to $x = 0.9$, the pair yield decreases. It appears that the effect of shrinking interaction volume outweighs the advantage stemming from the growing intensity.

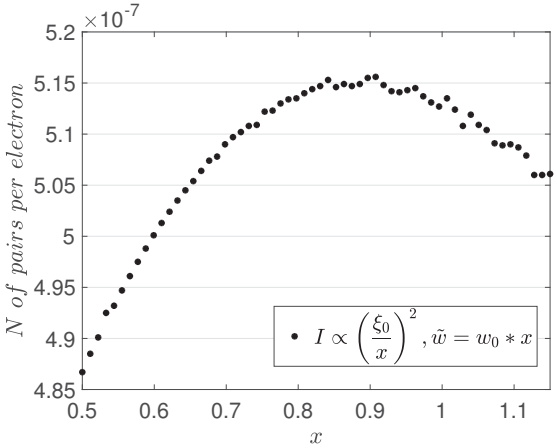

Figure 4.19: Number of produced pairs as a function of the laser intensity and the beam waist while keeping the pulse energy constant. The comparison is made for the reference values $\xi_0 = 110$, $w_0 = 1$ μm corresponding to $x = 1$ and $E_0 = 10$ GeV, while the remaining parameters are provided in the table 4.1. This figure was originally published in Ref. [51].

Not taking into account the results based on CCF or pulsed plane wave models, the fields so far were considered in paraxial approximation, which is well established as long

as the diffraction angle is small

$$\epsilon = \frac{2}{w_0 \omega} \ll 1. \tag{4.39}$$

Yet in the discussions above the values $\epsilon \approx 0.255$ and $\epsilon \approx 0.51$ were reached at $w_0 = 1$ μm and $w_0 = 0.5$ μm for $\lambda = 0.8$ μm (see Figs. 4.18 and 4.19), which are close to the diffraction limit. Thus, in order to assess the deviations existing in the presented calculations, the electromagnetic fields including higher order terms in ϵ have been incorporated (see appendix C.3) while generating Fig. 4.20. Here, the number of created pairs for two selected sharp energy values 500 MeV (left panel, $f = 0.2$) and 2375 MeV (right panel, $f = 0.95$) from the bremsstrahlung spectrum is exposed, i.e. no averaging is performed.

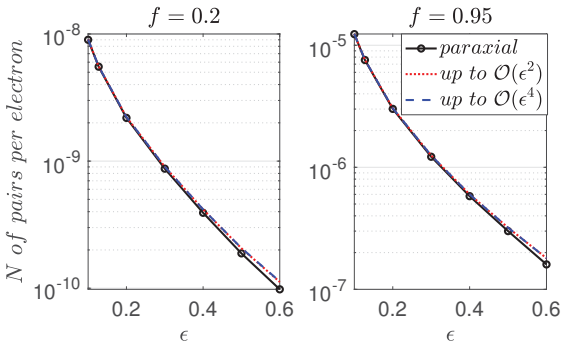

Figure 4.20: Deviations from Gaussian pulse in paraxial approximation (black solid) and beyond paraxial pulses (dotted red and dashed blue) for different diffraction angles ϵ and $\xi = 70$, while the energies of incident photons are fixed to $\omega' = 500$ MeV (left panel) and $\omega' = 2.357$ GeV (right panel). This figure was originally published in Ref. [51].

In both panels black patterns stand for paraxial Gaussian pulses, whereas red dotted and blue dashed curves incorporate additional terms in the series expansion in ϵ up to the orders $\mathcal{O}(\epsilon^2)$ and $\mathcal{O}(\epsilon^4)$, correspondingly. From Fig. 4.20 it can be seen that for both additional accuracy levels tiny deviations when compared to the paraxial pulse start to appear at $\epsilon \gtrsim 0.4$. This behaviour agrees well with the results presented in Ref. [61], where the electric and magnetic fields beyond paraxial approximation were initially introduced. Due to the rather small modification resulting from the higher-order terms, a conclusion is drawn that the paraxial approximation is applicable for the laser parameters utilised in this section.

4.3.6 Super-Gaussian profiles

In addition to focused Gaussian pulses, here, the results provided so far are extended to a field description by a super-Gaussian profile in both time and spatial envelopes. Firstly, the sensitivity of provided results to the chosen time envelope is studied. To that end, super-Gaussian time profiles are characterised by higher powers within

the time-dependent exponent of Eq. (4.1), i.e. when $2 \to n$ with $n = 4, 8, \ldots$

$$\mathcal{E}_x = \mathcal{E}_0 \frac{\mathrm{e}^{-\left(\sqrt{2\ln(2)}\frac{(t-z)}{\tau}\right)^n}}{\sqrt{1+\zeta(z)^2}} \mathrm{e}^{-\left(\frac{r}{w(z)}\right)^2} \sin(\Phi). \tag{4.40}$$

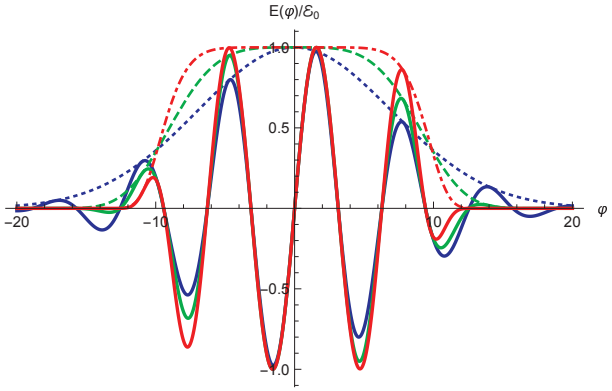

Figure 4.21: Pulses with Gaussian (blue dotted) and super-Gaussian time profiles with $n = 4$ (green dashed) and $n = 8$ (red dot-dashed). This picture has been generated by setting $\tau = 5$ fs and $\omega = 1.55$ eV and was originally published in Ref. [51].

The field configurations for $n = 2, 4, 8$ are depicted in Fig. 4.21. Thus, as n increases, the field profiles show broader plateaus around the origin and steeper decay at the edges: the fact that enables one to reach higher intensities when compared to the standard Gaussian model. Moreover, the corresponding pulse energies for $n = 4$ and $n = 8$ read

$$\begin{aligned} W_{n=4} &\approx \frac{\mathcal{E}_0^2}{2}\frac{\pi w_0^2}{2}\frac{\tau 2^{1/4}\Gamma\left(\frac{5}{4}\right)}{\sqrt{\ln(2)}}, \\ W_{n=8} &\approx \frac{\mathcal{E}_0^2}{2}\frac{\pi w_0^2}{2}\frac{\tau 2^{3/8}\Gamma\left(\frac{9}{8}\right)}{\sqrt{\ln(2)}} \end{aligned} \tag{4.41}$$

with $\Gamma(x)$ denoting the Gamma function [52].

Now, the outcomes resulting from a standard Gaussian pulse and super-Gaussian configurations with $n = 4$ and $n = 8$ are compared while keeping their energy at the same level. Thus, if the energy is fixed at the value of the paraxial Gaussian pulse, $W_{\mathrm{G}} = W_{n=2} = W_{n=4}$ must hold and the intensities of the super-Gaussian models have to be adjusted followingly

$$I_{n=4} = I\frac{\sqrt{\pi}}{2^{5/4}\Gamma(5/4)} \approx 0.82I, \quad I_{n=8} = I\frac{\sqrt{\pi}}{2^{11/8}\Gamma(9/8)} \approx 0.73I, \tag{4.42}$$

where I stands for the standard paraxial intensity.

To that end, Fig. 4.22 depicts the investigation, where a number of pairs associated with a standard Gaussian (blue solid) at a particular ξ is checked against a corresponding N stemming from super-Gaussian time envelopes (red dashed for $n = 4$ and blue dashed for $n = 8$) with lower effective intensity parameters (as $\xi = \frac{|e|}{m\omega}\sqrt{2I}$). Here, the $x-$axis is provided by the ξ parameter of the standard Gaussian. While all the three curves show an upward trend, the super-Gaussians overpass the standard Gaussian yield at $\xi \approx 40$. This behaviour supports the reasoning from the previous subsections stating that, for relatively low values of ξ, pair production is driven by the regions with highest intensity around the origin.

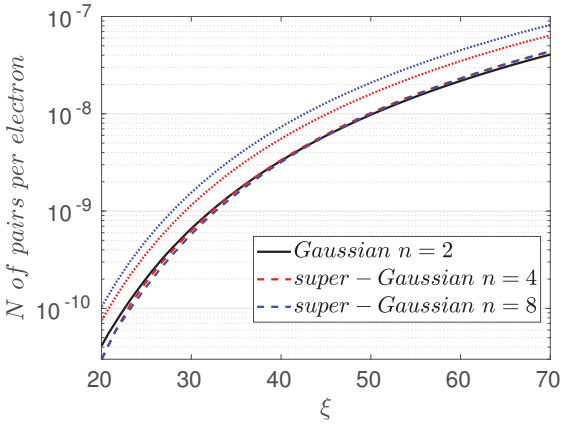

Figure 4.22: Number of produced pairs for laser pulses described with super-Gaussian time envelopes (red, blue dashed) and standard Gaussian with intensity parameter $\xi = 70$ (black solid) when keeping the laser energy for all pulses at the standard Gaussian level. Dotted curves result when the value of ξ is kept the same for all pulse shapes. This figure was originally published in Ref. [51].

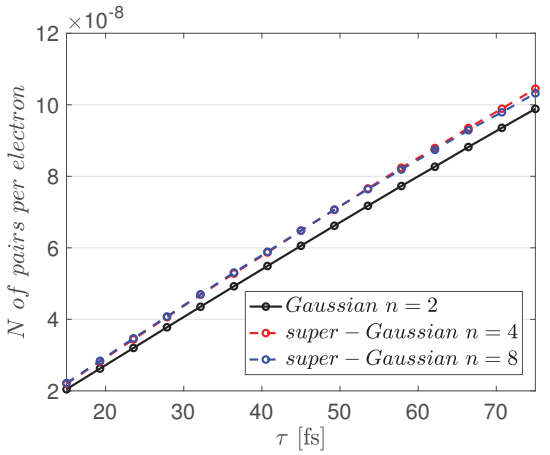

Figure 4.23: Number of produced pairs for laser pulses with super-Gaussian time envelopes (red, blue dashed) compared to standard Gaussian (black solid) when keeping the laser energy at the standard Gaussian level. This figure was originally published in Ref. [51].

Conversely, at larger ξ values a broader intensity range contributes substantially and the super-Gaussian plateaus may benefit the process more strongly. Additionally, when no modification of the intensity is undertaken, one obtains estimated particle yields depicted by the dotted lines in Fig. 4.22. As in this scenario the energy in super-Gaussian pulses exceeds the one of the standard Gaussian pulse, the former lead to more created pairs in the whole intensity range, with the outcome for $n = 8$ exceeding the one for $n = 4$.

The super-Gaussian time envelopes are studied also in Fig. 4.23, where the focus lies on the dependence of the pair yield on the pulse duration. Analogously to the previous paragraph, here, the laser pulse energy is kept constant for all three considered profiles denoted by black (standard Gaussian), red ($n = 4$ super-Gaussian) and blue ($n = 8$ super-Gaussian) patterns. Hence, the intensity is varied correspondingly to $\xi = 70$ for $n = 2$, $\xi = 63.5$ for $n = 4$ and $\xi = 59.6$ for $n = 8$. Following Fig. 4.23 all three curves posses positive trends. However, the broader envelopes lead to a higher pair production yield in the considered range. Thus, at the given energy the intensity decrease can be compensated by increasing the effective interaction time T_{int} (see Eq. (4.41)).

Next, super-Gaussian profiles modelling the transverse shape of the wave are considered. The latter are defined through their intensity in the focal plane $z = 0$ [80, 81]

$$I(r) = I_0 \mathrm{e}^{-2\left(\frac{r}{w_0}\right)^m} \tag{4.43}$$

with $m \geq 2$ and peak intensity $I_0 = \mathcal{E}_0^2$. Thus, the corresponding nonvanishing electromagnetic field component reads

$$\mathcal{E}_x = \mathcal{E}_0 \mathrm{e}^{-\left(\sqrt{2\ln(2)}\frac{\varphi}{\omega\tau}\right)^2} \mathrm{e}^{-\left(\frac{r}{w_0}\right)^m} \sin(\varphi)\,. \tag{4.44}$$

For $m = 2$, the expression above describes the leading order term of the paraxial field for $z/z_R \ll 1$ (see Eq. (4.1)) and in the limit of $m \to \infty$ the transversal part converges to a rectangular function.

Here, a comment is in order. An analytical formula for super-Gaussian spatial profiles, which was provided above, is valid only in the focal plane. In order to extend it to the whole transversal area, numeric propagation methods are required, which go beyond the scope of the present study. Thus, the expressions given here are valid only in the regions where the longitudinal focusing of the laser beam can be neglected. With this detail in mind, the pulse energy in the discussed scenario is calculated and for $m = 4$ and $m = 8$ the latter results into

$$W_{m=4} \approx \frac{\mathcal{E}_0^2}{2} \frac{\pi^{3/2} w_0^2}{2^{3/2}} \frac{\tau}{2} \sqrt{\frac{\pi}{\ln(2)}}, \quad W_{m=8} \approx \frac{\mathcal{E}_0^2}{2} \frac{\pi w_0^2 \Gamma\left(\frac{5}{4}\right)}{2^{1/4}} \frac{\tau}{2} \sqrt{\frac{\pi}{\ln(2)}}. \tag{4.45}$$

Similarly to the case of temporal profiles, when proceeding to studying the impact of spatial focusing on transversal super-Gaussian fields, their energy must be kept equal to the reference model. Hence, when comparing the latter to a focused paraxial pulse from Eq. (4.1), the corresponding laser intensity parameters read

$$\xi_{n=4} = \xi \left(\frac{2}{\pi}\right)^{1/4} \approx 0.89\xi,$$
$$\xi_{n=8} = \xi \left(2^{3/4}\Gamma\left(\frac{5}{4}\right)\right)^{-1/2} \approx 0.81\xi. \tag{4.46}$$

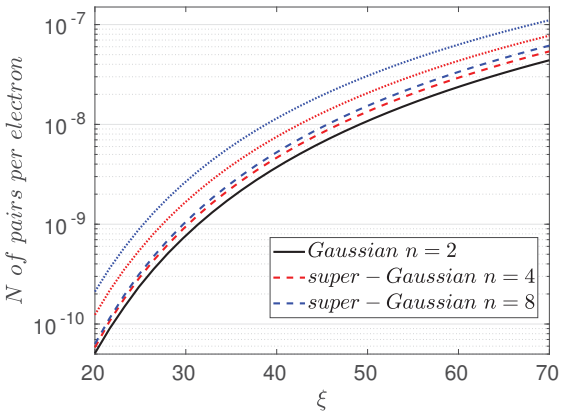

Figure 4.24: Dependance of the number of produced pairs on the spatial profile of laser pulse. Here, super-Gaussian envelopes (red, blue dashed) in the transverse plane are compared to standard Gaussian. This figure was initially published in Ref. [51].

Omitting the effect of longitudinal focusing (as the expressions above apply solely in the $z = 0$ plane), in Fig. 4.24 the number of created pairs per incident bremsstrahlung electron is elucidated when varying the reference value of the standard Gaussian ξ. The black solid curve stands for the unaltered paraxial pulse outcome, whereas $n = 4$ and $n = 8$ super-Gaussians are

marked by dashed red and blue styles. It is noteworthy to point out that, as it has been indicated previously in Fig. (4.16), for the chosen parameter range neglecting the longitudinal focusing in the current discussion will not lead to a sizeable error. From the graphs in Fig. 4.24, it can be seen that both super-Gaussian curves lie above the paraxial result. This effect, although small, provides an indication regarding the importance of optimising the interaction area: the effect of decreasing the intensity from $I = 10^{22}$ W/cm^2 to $I_{n=4} = 8.4 \times 10^{21}$ W/cm^2 and $I_{n=8} = 6.9 \times 10^{22}$ W/cm^2 may be cancelled out by extending the region of maximal intensity, i.e. broadening the laser beam. Finally, the dotted curves in Fig. 4.24 represent particle yields with unadjusted intensities which are kept constant at the level of the $x-$axis value. In this scenario the results associated with the super-Gaussian profiles are higher than the standard Gaussian case throughout the whole range with the largest estimated particle number for $n = 8$.

4.4 Summary

Summing up, in the present chapter a theoretical consideration of an approach for experimental observation of Breit-Wheeler electron-positron pair creation in the linear and highly nonlinear nonperturbative regimes was presented. Both studies rely on a setup depicted in Fig. 4.1, where a quantised photon stemming from high energetic GeV bremsstrahlung impinges on a high intensity laser pulse. In the linear case a strong field pulse is produced by an x-ray laser with $\xi \ll 1$, whereas nonlinear process relies on a laser with an optical wavelength and $\xi \gg 1$.

Firstly, in the linear regime described in section 4.2 a strong field QED technique was adopted allowing for exact incorporation of a laser field modelled as a paraxial Gaussian beam. Though, a conclusion was drawn that the field focussing is of minor importance in this case as tight focusing of the beam is not mandatory. Important experimental parameters turned out to be: energy of the incident electrons E_0, thickness of the high-Z target ℓ, in which bremsstrahlung is emitted, and the distance L between the bremsstrahlung production point and the laser focal point, where the interaction takes place. Moreover, an estimated number of created pairs was provided, which when considering $E_0 = 4$ GeV, $\ell = 1.25$, $L = 0.5$ m for a laser with $\omega = 0.3$ keV and $\tau = 100$ fs duration, amounts up to 800 Breit-Wheeler pairs per laser shot.

Next, the nonlinear nonperturbative process in the $\xi \gg 1$, $\kappa \approx 1$ regime was put under theoretical scrutiny in section 4.3. Breit-Wheeler particle production in this parameter range is of special interest as it allows for observation of the Schwinger-like behaviour of the pair creation rate (see subsection 3.2.2). Here, a convenient framework of LCFA was applied in a way that allows for investigation of the role of transverse and longitudinal focusing of the strong field laser pulse as the regime in question is achievable solely in tightly focused laser pulses. Thus, different field models were adopted, where the laser is described as a constant field in a well defined spacetime volume, a pulsed plane wave with a Gaussian time envelope and a focused paraxial Gaussian pulse, while keeping the energy constant. When a field description

by a paraxial Gaussian pulse was pursued, estimations for the created number of pairs for the parameter range envisaged at the experiment planned at CALA (see Ref. [33]) were elucidated: up to 10 pairs per hour could be detected at the facility in question. Moreover, studies were conducted in order to provide the number of pairs created in various focal regions of the laser pulse depending on the field intensity and the energy of bremsstrahlung photons, as well as a general assessment of the role of longitudinal focusing was performed. Further, the importance of tighter focusing while adjusting the intensity was discussed and, lastly, super-Gaussian time and space profiles were incorporated and effects of varying interaction spacetime volume shown.

Chapter 5

Pair production in QED_{2+1}

In the context of high energy physics, low dimensional theories have proven themselves as a powerful tool for providing useful insights to their higher dimensional analogues. For example, some aspects of nonperturbative quantum choromodynamics (see e.g. [82] and references therein) and solvability of the theory of gravity [83] were revealed in that way. Moreover, the discovery of the quantum Hall effect in 2+1 dimensional systems [84] and our understanding of high temperature QED were facilitated by the quantum electrodynamics in 2+1 dimensions (QED_{2+1}) with the Chern-Simons contribution [85]. Regarding the question of pair production, the Schwinger mechanism was extensively studied in various spacetime dimensions in constant uniform electric and magnetic fields [86] and electric fields of finite duration [87]. In addition, Schwinger pair creation was put under theoretical scrutiny in graphene: a solid state system, where excited valence electrons form a quasiparticle-hole pair which behaves relativistically and can be described by a 2+1 dimensional Dirac-like equation. Also Breit-Wheeler pair creation was considered in one spatial dimension, which allowed for higher spacetime resolution [88] and better accuracy of predictions [89] for this process.

Apart from gains in information for the 3+1 dimensional processes, the field of lower dimensional theories is of high relevance for quantum simulations, which are, due to their high complexity, usually designed in reduced dimensionality. The latter are realised via refined placement of ultracold atoms into optical lattices and are able to mimic the behaviour of many-body systems providing hints on the limits and applicability of the underlying theory. For QED, the research so far is concentrated on the 1+1 dimensional systems studying Schwinger pair production [90, 91, 92, 93, 94] and gradually evolves towards QED_{2+1} [95, 96, 97, 98].

Of particular interest in this chapter is the theory of 2+1 dimensional quantum electrodynamics, which is described via the action looking quite similar to Eq. (2.1) [99]

$$S[a,\psi,\bar{\psi}] = \int d^3x \left(\bar{\psi}(x) \left(i\not{D} - m \right) \psi(x) - \frac{1}{4} f_{\mu\nu}(x) f^{\mu\nu}(x) \right), \tag{5.1}$$

where all quantities, however, denote the 2+1 dimensional analogues of their higher dimensional counterparts and $d^3x = dtdxdy$. Thus, the $\gamma-$matrices in the covariant

derivative $D_\mu = \partial_\mu + i\mathfrak{e}a_\mu$, $\mu = 0, 1, 2$ are of the dimension 2×2 and further discussed in appendix A.1.2, whereas the fermion spinors have a form of two-dimensional vectors. Moreover, a reduction of spatial dimensions induces changes in the physical dimensions of the involved fields ψ, a and the electron charge $\mathfrak{e}$

$$[\psi] = \mathbf{E},\ [a] = \mathbf{E}^{1/2} \text{ and } [\mathfrak{e}] = \mathbf{E}^{1/2}, \tag{5.2}$$

where $\mathbf{E}$ stands for the dimension of energy. The fact that the charge in the expression above has a positive energy dimension makes QED_{2+1} a superrenormalisable theory [34]. Hence, a term $|\mathfrak{e}|^2/4\pi$ can no longer be identified with the traditional fine-structure constant $\alpha \approx 1/137$, which prevents one from performing the perturbation theory as explained in section 2.1. To that end, an alternative expansion parameter needs to be found, which in this scenario is chosen as a dimensionless intensity parameters $\eta = |\mathfrak{e}|a_0/m > 0$ with a gauge field amplitude a_0, an analogy to the intensity parameter ξ in QED. This assignment works because in a minimally coupled framework a combination $\mathfrak{e}a_0$ has always a dimension of energy regardless the number of space dimensions d: $[\mathfrak{e}a_0] = \mathbf{E}^{(3-d)/2}\mathbf{E}^{(d-1)/2} = \mathbf{E}$. Then, when assuming that $\eta \ll 1$, the perturbation theory can be applied as it was shown in section 2.1.

In the present chapter, the Breit-Wheeler pair production in the underlying low dimensional theory in various interaction regimes from weak to very strong fields is studied. Starting from the description of the involved fields when highlighting their differences when compared to 3+1 dimensional QED, the linear Breit-Wheeler process is considered. Next, particle creation in a monochromatic plane-wave-like field is discussed with particular focus on the low ($\eta \ll 1$) and high ($\eta \gg 1$) intensity regimes. And, lastly, a comment on the breakdown of perturbation theory and the relevance of the radiative corrections is made. This chapter is based on the results published in Ref. [100].

5.1 General aspects

5.1.1 Radiation field

In the present chapter, depending on the field intensity, two different kinds of electromagnetic fields are involved: a strong field, which will be incorporated in the procedure within the Furry picture (see subsection 2.4.1), and a low-intensity field with $\eta \ll 1$ that is quantised. In 2+1 dimensions both fields are solutions of the Maxwell equations resulting from Eq. (5.1) and their magnetic and electric field components are a pseudo scalar and a two component vector, respectively [101].

The weak field contributes to the Breit-Wheeler pair production in terms of the gauge field operator, which when quantised within a Gupta-Bleuler formalism reads [99]

$$\hat{a}_\mu(x) = \sum_{\lambda,k} \frac{1}{\sqrt{2\omega A_\gamma}} \left(\epsilon_{\mu,\lambda}\hat{a}_{k,\lambda}\mathrm{e}^{-ikx} + \epsilon^*_{\mu,\lambda}\hat{a}^\dagger_{k,\lambda}\mathrm{e}^{ikx} \right), \tag{5.3}$$

where a normalisation area A_γ arises (compare to Eq. (2.7)). When instead no normalisation to one particle in the area is performed, a substitution $a_0/2 \equiv 1/\sqrt{2\omega A_\gamma}$ is made, where a_0 stands for the field amplitude. Moreover, a wave vector related to the expression above reads $k^\mu = (\omega, \boldsymbol{k})$ with $\boldsymbol{k} = (k_1, k_2)$, while the focus here is put only on the transversal polarisation vectors ϵ^μ, which obey $k^\mu \epsilon_\mu = 0$, are normalised to $\epsilon^\mu \epsilon_\mu = -1$ and fulfil the completeness relation

$$\epsilon^\mu \epsilon^\nu = -g^{\mu\nu} - \frac{k^\mu k^\nu - nk(k^\mu n^\nu + k^\nu n^\mu)}{(nk)^2} \tag{5.4}$$

with $n^\mu = (1, 0, 0)$.

Conversely, in this chapter the strong field is represented by a linearly polarised plane-wave-like three-potential of the form

$$a^\mu(kx) = a_0 \epsilon^\mu \cos(kx) \tag{5.5}$$

for $\mu = 0, 1, 2$ and $kx = \omega t - \boldsymbol{kx}$.

5.1.2 Free fermions

Similarly to QED_{3+1}, in 2+1 dimensional space free Dirac fermions represent a solution of the free Dirac equation

$$(i\partial\!\!\!/ - m)\psi = 0, \tag{5.6}$$

which, however, has a different dimensionality and manifests a $\mathrm{SO}(1,2)$ invariance [99, 102]. The solution is found by employing the plane-wave ansatz (see beginning of appendix A.2.1) and resembles Eq. (2.15) with elementary spinors from appendix A.2.2 and normalisation to one particle in an area A instead of volume V. When quantised, the field operators read

$$\begin{aligned} \hat{\psi}(x) &= \sum_p \sqrt{\frac{m}{p_0 A}} \left(u_p \hat{b}_p \mathrm{e}^{-ipx} + v_p \hat{d}_p^\dagger \mathrm{e}^{ipx} \right), \\ \hat{\bar{\psi}}(x) &= \sum_p \sqrt{\frac{m}{p_0 A}} \left(\bar{v}_p \hat{d}_p \mathrm{e}^{-ipx} + \bar{u}_p \hat{b}_p^\dagger \mathrm{e}^{ipx} \right), \end{aligned} \tag{5.7}$$

where u_{p^-} refers to a free electron spinor, whereas v_{p^+} is the free negative-energy solution from appendix A.2.2. Following Eq. (A.6), there is no longer a spin degree of freedom in the system, and, thus, no sum over this quantum number in the equations above is needed. Moreover, the momentum space representation of the fermion propagator in 2+1 dimensions is given by

$$S_F(x-y) = \int \frac{d^3p}{(2\pi)^3} \frac{\mathrm{e}^{ip(x-y)}}{p\!\!\!/ - m + i0}. \tag{5.8}$$

5.1.3 Volkov states in 2+1 dimensions

Following Eq. (5.1), the time evolution of planar relativistic electrons interacting with a strong electromagnetic field $a_\mu(x)$ is described by a Dirac equation

$$\left(i\not{\partial} - m\right)\psi = 0. \tag{5.9}$$

As in 3+1 dimensions, the equation above is solvable only for a certain class of electromagnetic fields. For a field configuration as given in Eq. (5.5), the procedure follows the approach presented in section 2.4.2, despite of the inherent differences caused by the dimensionality, and one obtains

$$\hat{\Psi}_{q^-}(x) = \sqrt{\frac{m}{q_0^- A}}\left(1 + \frac{\mathfrak{e}}{2kq^-}\not{k}\not{a}\right)u_{p^-} \times \exp\left[-iq^-x - i\frac{\mathfrak{e}a_0 q^-\epsilon}{kq^-}\sin(kx) - i\frac{\mathfrak{e}^2 a_0^2}{8kq^-}\sin(2kx)\right]. \tag{5.10}$$

Here, the averaged effective momentum reads $q_\mu^- = p_\mu^- + \frac{\mathfrak{e}^2 a_0^2}{4kp^-}k_\mu$ with the effective electron mass $q^{-2} = m_*^2 = m^2(1+\eta^2/2)$. Analogously, the Volkov solution for a positron $\Psi_{q^+}(x)$ is given by Eq. (5.10) when carrying out the replacements: $p^- \to -p^+$ and $u_{p^-} \to v_{p^+}$.

5.2 Pair creation by two photons in 2+1 dimensions

When energetically allowed, an electron-positron pair with momenta $p_\pm$ can be created from two photons with the wave vectors k and k', which are represented via the Fock number states. To that end, the S-matrix element reads

$$S_{fi} = \langle 1_{p^+}; 1_{p^-}|\hat{S}^{(2)}[\hat{\psi}, \hat{\bar{\psi}}, \hat{a}]|1_{k'}; 1_k\rangle, \tag{5.11}$$

where $\hat{S}^{(2)}[\hat{\psi}, \hat{\bar{\psi}}, \hat{a}]$ stands for the second order scattering operator from the second line in Eq. (2.6). The corresponding Feynman diagrams can be seen in Fig. 5.1. Here, solid external lines denote created electron and positron, internal connecting pieces stand for the fermionic propagator in 2+1 dimensions and wavy lines represent the incident photons. Thus, when using the (anti-)commutation relations for the involved particles and the definition of the Feynman propagator one obtains

$$S_{fi} = -i\mathfrak{e}^2\sqrt{\frac{1}{2^2\omega\omega' A_\gamma^2}\frac{m^2}{p_0^+ p_0^- A^2}}\left(\int d^3x\, d^3y\, \bar{u}_{p^-}\not{\epsilon}S_F(x-y)\not{\epsilon}' v_{p^+}\mathrm{e}^{i(p_+-k')y + i(p_--k)x} + \int d^3x\, d^3y\, \bar{u}_{p^-}\not{\epsilon}' S_F(x-y)\not{\epsilon} v_{p^+}\mathrm{e}^{i(p_--k')x + i(p_+-k)y}\right). \tag{5.12}$$

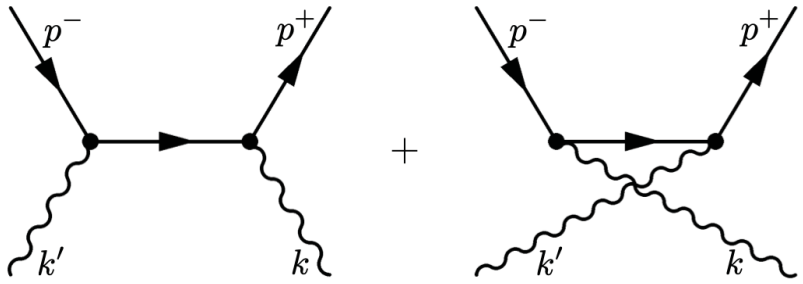

Figure 5.1: Feynman diagrams for linear Breit-Wheeler process.

Here, the Feynman slashed notation regarding the photon polarisations $\not{\epsilon}^{(\prime)} = \epsilon_\mu^{(\prime)}\gamma^\mu$ is restored. Then, the Feynman propagators in their momentum representation are inserted and integrals over the spatial variables are carried out. Making use of the Dirac $\delta-$functions the remaining momentum integrations can be performed, which leads to

$$S_{fi} = -\frac{i\mathfrak{e}^2}{A_\gamma A}\sqrt{\frac{m^2}{p_0^+ p_0^-}}\sqrt{\frac{1}{2^2\omega\omega'}}(2\pi)^3\delta^3(k+k'-p^+-p^-)\mathcal{M}_{\gamma\gamma'} \tag{5.13}$$

with

$$\mathcal{M}_{\gamma\gamma'} = \bar{u}_{p^-}\left(\frac{\not{\epsilon}\not{\epsilon}'}{\not{k}'-\not{p}^+-m+i0}+\frac{\not{\epsilon}'\not{\epsilon}}{\not{k}-\not{p}^+-m+i0}\right)v_{p^+}. \tag{5.14}$$

Similarly to the particle rate per volume in 3+1 dimensions, in this chapter a differential particle rate per area, which is defined as

$$dR^{2+1} = \frac{|S_{fi}|^2}{TA}A^2\frac{d^2p^-}{(2\pi)^2}\frac{d^2p^+}{(2\pi)^2}, \tag{5.15}$$

is integrated over the reduced 4-dimensional phase space of the created particles. Thus, in the present context the quantity in question can be written as

$$R^{2+1}_{\gamma\gamma'} = \frac{\mathfrak{e}^4}{A_\gamma^2}\frac{m^2}{8\pi\omega\omega'}\int\frac{d^2p^-}{p_0^-}\frac{d^2p^+}{p_0^+}\delta^3(k+k'-p^+-p^-)|\mathcal{M}_{\gamma\gamma'}|^2, \tag{5.16}$$

where the square of the amplitude reads

$$|\mathcal{M}_{\gamma\gamma'}|^2 = \frac{1}{16m^2}\mathrm{Tr}\Big[\left(\not{\epsilon}\frac{\not{k}'-\not{p}^+ +m}{k'p^+}\not{\epsilon}'+\not{\epsilon}'\frac{\not{k}-\not{p}^+ +m}{kp^+}\not{\epsilon}\right)(\not{p}^+ -m) \\ \times\left(\not{\epsilon}'\frac{\not{k}'-\not{p}^+ +m}{k'p^+}\not{\epsilon}+\not{\epsilon}\frac{\not{k}-\not{p}^+ +m}{kp^+}\not{\epsilon}'\right)(\not{p}^- +m)\Big]. \tag{5.17}$$

Using the properties of the $\gamma-$matrices from appendix A.1.2 and the energy-momentum conservation, the expression above reduces to

$$|\mathcal{M}_{\gamma\gamma'}|^2 = \frac{1}{m^2}\left[\frac{(kk')^2}{4kp^+kp^-} - 1 + \frac{2m^2kk'}{kp^+kp^-} - \frac{m^4(kk')^2}{(kp^+kp^-)^2}\right] \tag{5.18}$$

and the rate per area reads

$$R^{2+1}_{\gamma\gamma'} = \frac{\mathfrak{e}^4 a_0^2 a_0'^2}{32\pi}\int \frac{d^2p^-}{p_0^-}\frac{d^2p^+}{p_0^+}\delta^3(k+k'-p^+-p^-) \times\left[\frac{(kk')^2}{4kp^+kp^-} - 1 + \frac{2m^2kk'}{kp^+kp^-} - \frac{m^4(kk')^2}{(kp^+kp^-)^2}\right], \tag{5.19}$$

where the relations $a_0^{(\prime)2} \equiv 2/\omega^{(\prime)}A_\gamma$ have been inserted. The integration is conveniently performed in the center of momentum reference frame by adopting polar coordinates. Thus, $\boldsymbol{p} = \boldsymbol{p}^+ = -\boldsymbol{p}^-$, $p_0^+ = p_0^-$, $\omega = \omega'$, $kk' = 2\omega\omega' = 2\omega^2$ with $kp = \omega(p_0 - |\boldsymbol{p}|\cos(\phi))$ and after integrating out p^- and p_0 by employing the corresponding $\delta-$functions one arrives at

$$R^{2+1}_{\gamma\gamma'} = \frac{\mathfrak{e}^2 a_0'^2 m^2}{8\pi}\frac{\eta^2}{4}\frac{1}{2\omega}\int_0^{2\pi} d\phi\Big[-1 - \frac{4u^2}{[1-(1-u)\cos^2(\phi)]^2} + \frac{(1+4u)}{[1-(1-u)\cos^2(\phi)]}\Big] \tag{5.20}$$

with $u = m^2/\omega^2$ and $\eta = |\mathfrak{e}|a_0/m$. The remaining integration is performed by using Eqs. (3.616.8) and (3.642.3) in Ref. [103] and in terms of the Mandelstam variable $s = \sqrt{kk'/2m^2}$ it reads

$$R^{2+1}_{\gamma\gamma'} = \frac{\mathfrak{e}^2 a_0'^2 m}{8\pi}\frac{\pi\eta^2}{4s}\left[-1 - \frac{2(s^2+1)}{s^3} + \frac{(4+s^2)}{s}\right]. \tag{5.21}$$

From the equation above a quantity $\alpha_{2+1} = \mathfrak{e}^2/(4\pi m)$ may be read off, which represents the counterpart of the QED fine-structure constant α. Moreover, when $m \gg \mathfrak{e}^2/(4\pi)$ holds, α_{2+1} plays the role of a perturbative coupling constant. Next, the rate per area displayed in the equation above can be compared with the leading order expression resulting from the consideration of Breit-Wheeler pair creation in a monochromatic wave at low intensities (see Eq. (5.38)). The latter is discussed in detail in the next section.

5.3 Pair creation in a monochromatic plane-wave-like field

In this section the creation of an electron-positron pair with three-momenta $p_\mp$ via the Breit-Wheeler process with a plane-wave-like electromagnetic field from Eq. (5.5) is considered (see Fig. 3.1 for the Feynman diagram). As the classical field is assumed to be strong, the corresponding intensity parameter η is much larger than η', which

stands for the intensity parameter of the weak quantised field. To that end, the Furry picture approach from subsection 2.4.1 is applied and the transition amplitude results, analogously to Eqs. (3.1) and (3.2), from the first order scattering operator with the dressed states

$$S_{fi} = -i\mathfrak{e}\int d^3x \bar{\Psi}_{q^-}(x)\not{a}'(x)\Psi_{q^+}(x), \tag{5.22}$$

where $a'_\mu(x) = \frac{a'_0}{2}\epsilon'_\mu \mathrm{e}^{-ik'x}$ denotes the photon wave function, which refers to the amplitude a'_0 rather than being normalised to one particle in the area, and $\Psi_{q^\pm}$ are the Volkov solutions from subsection 5.1.3. When inserting the latter into the equation above, terms proportional to the exponential $\cos^l(kx)\mathrm{e}^{-iz_-\sin(kx)-iz_+\sin(2kx)}$ with $l = 0, 1, 2$ and

$$z_- = \mathfrak{e}a_0\left(\frac{q^+\epsilon}{q^+k} - \frac{q^-\epsilon}{q^-k}\right), \qquad z_+ = -\frac{\mathfrak{e}^2a_0^2}{8}\frac{kk'}{kq^+kq^-} \tag{5.23}$$

arise. Here, their Fourier expansions from Eqs. (B.5) and (B.6) in appendix B are employed and, afterwards, the transition amplitude reads

$$S_{fi} = -i\frac{\mathfrak{e}a'_0}{2}\sqrt{\frac{m^2}{q_0^+q_0^-A^2}}\sum_{n=-\infty}^{\infty}(2\pi)^3\delta^3(nk+k'-q^+-q^-)\bar{u}_{p^-}M_n v_{p^+}, \tag{5.24}$$

where M_n is of the following form

$$M_n = \not{\epsilon}'\tilde{J}_n(z_-,z_+) + \frac{\mathfrak{e}a_0}{2}\tilde{\mathcal{J}}_n^1\left(\frac{\not{\epsilon}\not{k}\not{\epsilon}'}{kq^-} - \frac{\not{\epsilon}'\not{k}\not{\epsilon}}{kq^+}\right) - \frac{\mathfrak{e}^2a_0^2}{2kq^+kq^-}\epsilon'^\mu k_\mu\tilde{\mathcal{J}}_n^2\not{k}. \tag{5.25}$$

In order to derive the expression above the energy-momentum conservation $q^+ + q^- = nk + k'$ provided by the Dirac $\delta-$functions, anticommutativity of $\gamma-$matrices as well as transversal condition $\epsilon k = 0$ have been used.

Next, the rate of the process as it was defined in Eq. (5.15) is considered. However, similarly to chapter 3, in order to simplify the integrations the relation $d^2p^-d^2p^+/(p_0^-p_0^+) = d^2q^-d^2q^+/(q_0^-q_0^+)$ is used, and the differential rate reads

$$dR^{2+1} = \frac{|S_{fi}|^2}{TA}A^2\frac{d^2q^-}{(2\pi)^2}\frac{d^2q^+}{(2\pi)^2}, \tag{5.26}$$

which results into

$$R^{2+1} = \frac{\mathfrak{e}^2a_0'^2m^2}{8\pi}\sum_{n=-\infty}^{\infty}\int\frac{d^2q^-}{q_0^-}\frac{d^2q^+}{q_0^+}\delta^3(nk+k'-q^+-q^-)|\bar{u}_{p^-}M_nv_{p^+}|^2, \tag{5.27}$$

when Eqs. (5.24) and (5.26) are combined. In the equation above the sum over n can be interpreted as a sum over the number of absorbed photons from the classical field $a^\mu(kx)$.

Further, when taking into account the normalisation and properties of elementary spinors in 2+1 dimensions from and below Eq. (A.7) in appendix A.2.2, the squared transition amplitude $|\mathcal{M}^n|^2 = |\bar{u}_{p^-} M_n v_{p^+}|^2$ can be written as

$$|\mathcal{M}^n|^2 = \mathrm{Tr}\left[\frac{\not{p}^- + m}{2m} M_n \frac{\not{p}^+ - m}{2m} \bar{M}_n\right] \tag{5.28}$$

with $\bar{M}_n = \gamma^0 M_n^\dagger \gamma^0$. At this point it is noteworthy to comment on the trace from the equation above: Although the form of the squared amplitude remains unchanged with respect to 3+1 dimensions as it was given in Eq. (3.9), the trace is no longer taken over a 4×4 matrix, but rather over the one of dimension 2×2. Furthermore, no averaging over the photon polarisations and summing up the lepton spins is necessary. Thus, with the completeness relation from Eq. (5.4) one obtains

$$|\mathcal{M}^n|^2 = \tilde{J}_n^2(z_-, z_+) - \frac{\mathfrak{e}^2 a_0^2}{m^2}\left(1 - \frac{(kk')^2}{4kq^+kq^-}\right)\left[(\tilde{\mathcal{J}}_n^1)^2 - \tilde{J}_n(z_-, z_+)\tilde{\mathcal{J}}_n^2\right], \tag{5.29}$$

where the energy-momentum balance and transversal condition have been used. Here, owing to the Ward identity, only the term containing $-g^{\mu\nu}$ from Eq. (5.4) contributes to the squared amplitude and, similarly to chapter 3, the relation given in Eq. (3.11) was exploited.

With all these details at our disposal, in 2+1 dimensions the rate per area for Breit-Wheeler pair creation in a plane-wave-like field reads

$$\begin{aligned} R^{2+1} = \frac{\mathfrak{e}^2 a_0'^2 m^2}{8\pi} \sum_{n \geq n_0}^{\infty} \int \frac{d^2q^-}{q_0^-} \frac{d^2q^+}{q_0^+} \delta^3(nk + k' - q^+ - q^-) \\ \times \left[\tilde{J}_n^2(z_-, z_+) - \eta^2 \left(1 - \frac{(kk')^2}{4kq^+kq^-}\right)\left[(\tilde{\mathcal{J}}_n^1)^2 - \tilde{J}_n(z_-, z_+)\tilde{\mathcal{J}}_n^2\right]\right] \end{aligned} \tag{5.30}$$

with a summation starting at $n_0 = 2m_*^2/(kk')$ due to the energy-momentum balance. Next, a comparison between the expression above and the corresponding particle rates in 3+1 dimensions (see Eqs. (3.14) and (3.15)) is drawn. Leaving aside the lower dimensionality of the delta functions and the involved integration measures, the main difference between R^{2+1} and the unpolarised rate in 3+1 dimensions from Eq. (3.15) lies in the precise structure of the squared amplitude. The latter rather resembles the squared amplitude of the pair production by a photon with polarisation parallel to the electric field of the wave in Eq. (3.12) when setting $\sigma = 1$. Following the last line of Eq. (3.32), this condition means lowering the dimensionality of the system to a plane by elimination of the axis orthogonal to the polarisations of the quantised photon and the strong field. Thus, it highlights the restriction provided by a lower dimensionality: both photon wave vectors and polarisations are bound to a plane. Hence, when moving the system to a center of momentum frame of created particles, where photons are counterpropagating, their polarisations have to be parallel. In this reference frame the variables read $\boldsymbol{q}^- = -\boldsymbol{q}^+ = -\boldsymbol{q}$, $n\boldsymbol{k} = -\boldsymbol{k}'$,

$n\omega = \omega'$. After integrating out q^- and expressing the remaining integrals in polar coordinates the rate can be written as

$$R^{2+1} = \frac{\mathfrak{e}^2 a_0'^2 m^2}{8\pi} \sum_{n\geq n_0}^{\infty} \int_0^{2\pi} d\phi \int_0^{\infty} \frac{dq}{2q_0} \delta(q - q_n^*) \times \left(\tilde{J}_n^2(z_-, z_+) - \eta^2 \left(1 - \frac{1}{1 - \frac{q^2}{\omega'^2}\cos^2(\phi)} \right) \left[(\tilde{\mathcal{J}}_n^1)^2 - \tilde{J}_n(z_-, z_+) \tilde{\mathcal{J}}_n^2 \right] \right), \quad (5.31)$$

where $|\boldsymbol{q}| \equiv q$, $kq^+ = \omega[\omega' - q\cos(\phi)]$, $kq^- = \omega[\omega' + q\cos(\phi)]$, $\epsilon q^- = -\epsilon q^+ = q\sin(\phi)$ and $q_n^* = \sqrt{\omega'^2 - m_*^2}$, $q_0 = \omega'$ were set. With help of the Mandelstam invariant $s = \sqrt{kk'/2m^2}$ the threshold number of absorbed photons reads $n \geq (1 + \eta^2/2)/s^2$. For every value of n a threshold energy

$$s^2 \geq \frac{1}{n} \left(1 + \frac{\eta^2}{2} \right) = s_n^2 \quad (5.32)$$

can be defined, which must be overpassed in order for the process to occur, and $q_n^* = \omega' \sqrt{1 - (1 + \eta^2/2)/ns^2}$.

5.3.1 Threshold behaviour

Now, let us take a careful look at the behaviour of the rate at the energy threshold, where the particles are created with zero momentum ($q = 0$). In contrast to the higher dimensional case, the rate in Eq. (5.31) does not always vanish at $q = 0$. In 3+1 dimensions the remaining contribution in the rates from Eqs. (3.14) and (3.15) after integrating over q^- in the center of momentum frame

$$\int \frac{d^3q}{q_0^2} \delta(2q_0 - 2\omega') = \int d\Omega \int \frac{qdq}{2q_0} \delta(q - q_n^*) \propto q_n^* \overset{s\to s_n}{\longrightarrow} 0 \quad (5.33)$$

always goes to zero at the threshold. In the present case of 2+1 dimensions, however, the integrations over momenta with the Jacobi determinant will not vanish at all times in the energy regime of interest and the threshold behaviour of the process rate is governed solely by the process amplitude. Therefore, it is studied more in detail starting with the arguments of the generalized Bessel functions

$$z_- = -\frac{2\eta}{ms^2} \frac{q\sin(\phi)}{1 - \frac{q^2}{\omega'^2}\cos^2(\phi)} \overset{s\to s_n}{\to} 0, \quad z_+ = -\frac{\eta^2}{4s^2} \frac{1}{1 - \frac{q^2}{\omega'^2}\cos^2(\phi)} \overset{s\to s_n}{\to} -\frac{\eta^2}{4s_n^2} \equiv z_{+n}. \quad (5.34)$$

As one of the arguments vanishes at $q = 0$, the property of the generalized Bessel function of one argument $\tilde{J}_n(0, z_{+n})$ from Eq. (B.2) is called for, where a distinction between odd and even indices is made. Hence, when an even number of strong field

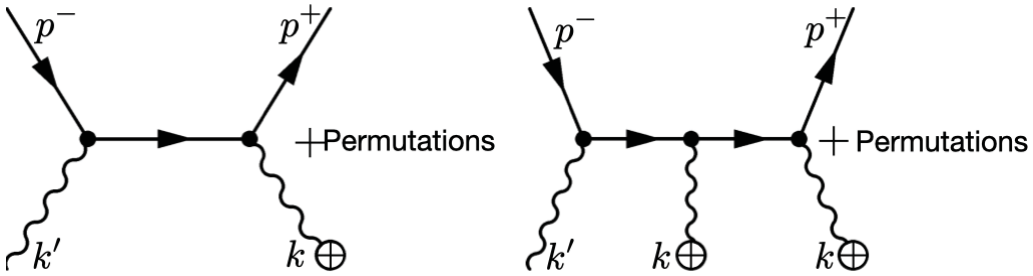

Figure 5.2: Feynman diagrams of two and three photons pair creation processes in external fields can be seen in the left and right panels.

photons $n = 2\ell$ is absorbed, the rate from Eq. (5.31) at the threshold reads

$$R^{2+1}_{s\to s_n} = \frac{\mathfrak{e}^2 a_0'^2 m}{8} \sum_{2\ell\geq n_0}^{\infty} \frac{J_\ell^2\left(-\frac{\eta^2\ell}{2(1+\eta^2/2)}\right)}{1+\eta^2/2}, \tag{5.35}$$

whereas for an odd number of laser photons participating in the reaction, it is equal to zero. Following the formula above, the threshold contribution to the rate vanishes at $\eta \gg 1$, whereas for $\eta \ll 1$ it behaves like

$$R^{2+1}_{s\to s_n} \approx \frac{\mathfrak{e}^2 a_0'^2 m}{8} \sum_{2\ell\geq n_0}^{\infty} \eta^{4\ell} \frac{\ell^{2(\ell-1)}}{2^{4\ell}\Gamma^2(\ell)}, \tag{5.36}$$

where $\Gamma(x)$ stands for the gamma function [52]. Thus, the nonvanishing threshold behaviour of the process rate plays an important role for the low intensity regime and will be studied further in the following subsection, where the small ξ asymptote is established.

5.3.2 Behaviour for $\eta \ll 1$

Similarly to the behaviour of the Breit-Wheeler rate in QED (see Eq. (3.16), the leading contributions to the pair creation in the present context are provided by the $n = 1$ and $n = 2$ terms in Eq. (5.30). The corresponding Feynman diagrams are depicted in Fig. 5.2. In both panels created fermions are denoted by external solid lines, internal pieces represent the free fermion propagators and wavy lines stand for the photons stemming from the quantised and classical (marked by crossed circles) fields.

When energetically feasible, an absorption of one laser photon provides the largest contribution to the process rate. Thus, the $n = 1$ summand in Eq. (5.30) will be studied next. To that end, for $\eta \ll 1$ the effective electron and positron momenta simplify to $q^\pm = p^\pm$. Moreover, the arguments of the generalized Bessel functions are written as $z_- = \eta m(\frac{p^-\epsilon}{p^-k} - \frac{p^+\epsilon}{p^+k})$, $z_+ = -\frac{\eta^2 m^2}{8}\frac{kk'}{kp^+kp^-}$ and their proportionality to

η and η^2 allows for expanding the Bessel functions in small arguments at it is shown in Eq. (B.7) in appendix B.1. Having these in mind the squared amplitude results into

$$|\mathcal{M}^{n=1}_{\eta\ll 1}|^2 = \frac{\eta^2 m^2}{4}\left(\frac{p^-\epsilon}{p^-k} - \frac{p^+\epsilon}{p^+k}\right)^2 - \frac{\eta^2}{4}\left(1 - \frac{(kk')^2}{4kp^+kp^-}\right) \tag{5.37}$$

and after using Eq. (5.4) combined with the energy-momentum conservation $p^+ + p^- = k + k'$ the rate for two photon interaction reads

$$R^{2+1}_{n=1} \approx \frac{\mathfrak{e}^2 a_0'^2 m^2}{8\pi}\frac{\eta^2}{4}\int \frac{d^2p^- d^2p^+}{p_0^- p_0^+}\delta^3(k + k' - p^+ - p^-) \times \left[\frac{(kk')^2}{4kp^+kp^-} - 1 + \frac{2m^2kk'}{kp^+kp^-} - \frac{m^4(kk')^2}{(kp^+kp^-)^2}\right]. \tag{5.38}$$

With $\eta = |\mathfrak{e}|a_0/m$ the equation above resembles the rate in Eq. (5.19), which was calculated within the framework of perturbation theory for a process where interaction of two quantised photons leads to creation of an electron-positron pair. Finally, the phase space integrations are carried out in the center of momentum frame as it was shown in section 5.2 and one arrives at

$$R^{2+1}_{n=1} \approx \frac{\mathfrak{e}^2 a_0'^2 m}{8\pi}\frac{\pi\eta^2}{4s}\left[-1 - \frac{2(s^2+1)}{s^3} + \frac{(4+s^2)}{s}\right]. \tag{5.39}$$

It is worth mentioning that the rate vanishes at the energy threshold, which in the present context corresponds to $s = 1$.

Next, the case where two strong field photons are absorbed (see lower panel of Fig. (5.2) for the corresponding Feynman diagram) is considered. Here, after the expansion of the Bessel functions in small arguments is performed the amplitude of the process up to $\mathcal{O}(\eta^4)$ equals to

$$|\mathcal{M}^{n=2}_{\eta\ll 1}|^2 = \left(\frac{z_+}{2} + \frac{z_-^2}{8}\right)^2 - \frac{\eta^2}{4}\left(1 - \frac{(kk')^2}{4kp^+kp^-}\right)\left(\frac{z_-^2}{8} - \frac{z_+}{2}\right) \tag{5.40}$$

and the corresponding rate reads

$$R^{2+1}_{n=2} \approx \frac{\mathfrak{e}^2 a_0'^2 m^2}{8\pi}\int \frac{d^2p^-}{p_0^-}\frac{d^2p^+}{p_0^+}\delta^3(2k + k' - p^+ - p^-)|\mathcal{M}^{n=2}_{\eta\ll 1}|^2. \tag{5.41}$$

Similarly to the $n = 1$ contribution, after employing the $\delta-$functions for integrations over p^- and a transition to the center of momentum frame, the remaining integrals in the equation above are carried out in polar coordinates with $\boldsymbol{p} = \boldsymbol{p}^+ = -\boldsymbol{p}^-$, $p_0^+ = p_0^- = \omega' = 2\omega$, $kk' = 4\omega^2$ and $kp = \omega(p_0 - |\boldsymbol{p}|\cos(\phi))$. Consequently, the asymptote for the two-photon absorption process from the strong field is obtained

$$R^{2+1}_{n=2} \approx \frac{\mathfrak{e}^2 a_0'^2 m}{8\pi}\frac{\pi\eta^4}{128 s^8}\left[10 - 30s^2 + 19s^4 + 12s^8\right]. \tag{5.42}$$

As it was already anticipated in Eq. (5.36), the equation above provides a nonvanishing contribution at the energy threshold corresponding to $s = s_2 = \sqrt{1/2}$.

The threshold behaviour of the $n = 1$ and $n = 2$ rates denoting the two- and three-photon processes, correspondingly, can be seen in the upper and lower panels of Fig. 5.3. Here, the asymptotes derived in the current section are depicted in blue, whereas the red dashed curves result from numerically evaluating Eq. (5.30). The graphs stemming from the study in 2+1 dimensions are compared to the Breit-Wheeler particle rates in standard QED from subsection 3.1.1 (black). The dotted curves represent the outcomes from a consideration, where the quantised photon was polarised parallelly to the polarisation of the strong field as it was presented in Eqs. (3.21) and (3.27), whereas black solid curves stand for the rates taking into account an unpolarised photon (see Eqs. (3.22) and (3.28)). Moreover, this assessment has been done by setting $\eta = 0.01$. From the discussed figure it can be seen that, with exception of the three-photon processes in QED$_{2+1}$, all particle rates provide a zero contribution at the energy threshold.

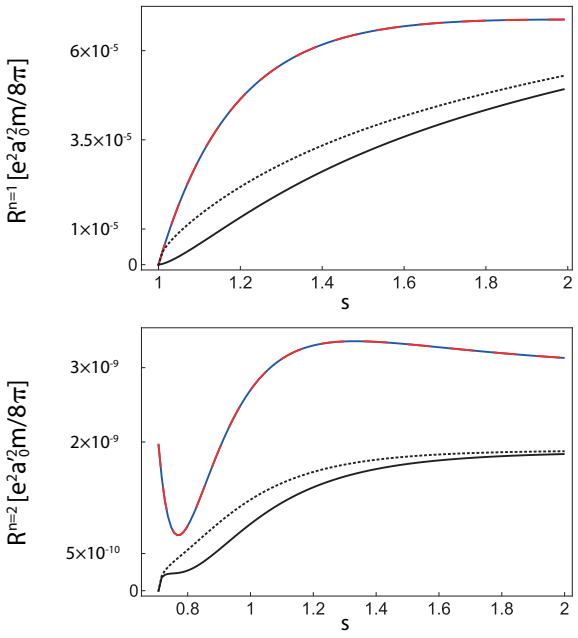

Figure 5.3: Pair production rates in 2+1 dimensions (blue and red) and in 3+1 dimensions (black) in dependence on the Mandelstam invariant s for $\eta = 0.01$. This figure was originally published in Ref. [100].

5.3.3 Behaviour for $\eta \gg 1$

In the high intensity limit a large number of strong field photons participates in the pair creation process. Thus, many summands in Eq (5.30) provide non-negligible contributions to the rate and, analogously to the calculation presented in section 3.1.2, a transition to the continuum limit $\sum_n ... \to \int dn...$ can be developed. Then, the integrals in n and $\boldsymbol{q}^+$ are performed with help of the delta functions and Eq. (5.30) reads

$$R^{2+1}_{\eta\gg1} = \frac{\mathfrak{e}^2 a_0'^2 m^2}{8\pi} \int \frac{d^2q^-}{q_0^- k q^+} |\mathcal{M}^{n=n^*}|^2 \tag{5.43}$$

with $|\mathcal{M}^{n=n^*}|^2$ as given in Eq. (5.29) for $n \to n^*$, $n^* = q^- k'/[\omega(\omega' - k_2' - q_0^- + q_2^-)]$. Here, it is assumed without loss of generality that the strong field a^μ is polarised in

x_1-direction. Next, a set of new variables is introduced:

$$\mathfrak{X} = \frac{kq^+}{m^2}\eta,\ \mathfrak{X}' = \frac{kq^-}{m^2}\eta,\ \gamma^- = q_0^- - q_2^-, \tag{5.44}$$

which allow for writing the arguments of the generalised Bessel functions $z_\pm$ as

$$z_+ = -\frac{\eta^3\kappa}{8\mathfrak{X}\mathfrak{X}'},\ z_- = \frac{\eta^2}{m\mathfrak{X}\mathfrak{X}'}(q^-\epsilon\mathfrak{X} - q^+\epsilon\mathfrak{X}') \tag{5.45}$$

with the quantum nonlinearity parameter in 2+1 dimensions $\kappa = \eta kk'/m^2$. The next step is represented by a substitution $q_2^- \to \gamma^-$ leading to

$$R^{2+1}_{\eta\gg1} = \frac{\mathfrak{e}^2 a_0'^2 m^2}{8\pi}\frac{\eta}{m^2}\int_{-\infty}^{\infty}\frac{dq_1^-}{\mathfrak{X}}\int_0^\lambda\frac{d\gamma^-}{\gamma^-}|\mathcal{M}^{n=n^*}|^2, \tag{5.46}$$

where $\lambda = \omega' - k_2'$. The squared amplitude in the expression above contains generalized Bessel functions, which are further developed in the limit of large arguments as the latter are dependent on η. The corresponding calculation is shown in appendix B.2, where changes induced by the lower dimensionality are highlighted throughout the study. Thus, taking into account Eq. (B.30) while setting $\sigma = 1$, which is justified as the process takes place in a plane and $\sigma = 1 + \mathfrak{t}^2$ with $\mathfrak{t}$ denoting a variable orthogonal to the surface spanned by the field polarisation and wave vectors (see Eq. (3.32) and description above it), one obtains for $\eta \gg 1$ and $\eta \gg \kappa^{1/3}$

$$|\mathcal{M}^{n=n^*}|^2 \approx \frac{2}{\pi}\left(-\frac{1}{4z_+\sin^2(x_0)}\right)^{2/3} \times\left[\Phi^2(z) - \left(1 - \frac{\kappa^2}{4\mathfrak{X}\mathfrak{X}'}\right)\left(\Phi^2(z) + \frac{\Phi'^2(z)}{z}\right)\right] \tag{5.47}$$

with $z = \frac{(-4\sin^2(x_0)z_+)^{2/3}}{\eta^2\sin(x_0)}$ and an Airy function $\Phi(z)$ [2]. Moreover, when deriving the equation above a new substitution involving x_0, $x_0 \in [0,\pi]$ has been performed: $\cos(x_0) = -\frac{\omega}{\kappa m^3}(q_1^-\gamma^+ - q_1^+\gamma^-)$ with $\gamma^+ = q_0^+ - q_2^+$ and $\gamma^+ + \gamma^- = \lambda$.

Further, a new integration variable ϑ is introduced, which is defined through

$$\mathfrak{X}' = \frac{\kappa}{2}[1 + \tanh(\vartheta)],\quad \mathfrak{X} = \frac{\kappa}{2}[1 - \tanh(\vartheta)]. \tag{5.48}$$

It is incorporated into the rate via a substitution $\mathfrak{X}' = \frac{\eta\omega}{m^2}\gamma^-$, which leads to integration limits over $\mathfrak{X}'$ spreading over the interval $[0,\kappa]$. As the integrand in Eq. (5.46) is symmetric in $\mathfrak{X}'$ and $\mathfrak{X}$ with $\mathfrak{X}' + \mathfrak{X} = \kappa$, the relation $\int_0^\kappa d\mathfrak{X}'... = 2\int_0^{\kappa/2} d\mathfrak{X}'...$ holds and the corresponding integration over ϑ runs from 0 to ∞. Taking these details into account the rate per area results to

$$R^{2+1}_{\eta\gg1} \approx \frac{\mathfrak{e}^2 a_0'^2 m}{8\pi}\frac{8}{\pi}\int_0^{\pi/2} dx_0 \int_0^\infty \frac{d\vartheta\sqrt{z}}{\cosh^2(\vartheta)}\left[\Phi^2(z)+\sinh^2(\vartheta)\left(\Phi^2(z)+\frac{\Phi'^2(z)}{z}\right)\right] \tag{5.49}$$

with $z = \left(\frac{2\cosh^2(\vartheta)}{\kappa\sin(x_0)}\right)^{2/3}$. Moreover, when using

$$\frac{\Phi'^2(z)}{z} = \frac{1}{2z}\frac{d^2\Phi^2(z)}{dz^2} - \Phi^2(z),\ \Phi^2(z) = \frac{1}{2^{2/3}\sqrt{\pi}}\int_0^\infty \frac{dt}{\sqrt{t}}\Phi(t+2^{2/3}z) \tag{5.50}$$

combined with the defining equation for the Airy functions (see Ref. [104]), the Breit-Wheeler rate can be written as a function depending linearly on the Airy function of the shifted argument $t + 2^{2/3}z$

$$R^{2+1}_{\eta\gg1} \approx \frac{\mathfrak{e}^2 a_0'^2 m}{8\pi}\frac{8}{2^{2/3}\pi^{3/2}}\int_0^{\pi/2} dx_0 \int_0^\infty \frac{dt}{\sqrt{t}} \times \int_0^\infty \frac{d\vartheta\sqrt{z}}{\cosh^2(\vartheta)}\left(1+\frac{2^{1/3}\sinh^2(\vartheta)}{z}\right)\Phi(t+2^{2/3}z). \tag{5.51}$$

Now, similarly to the procedure shown in subsection 3.1.2, the asymptotes of Eq. (5.49) for various κ regimes will be studied. Starting with $\kappa \ll 1$ it is helpful to notice that the Airy functions decrease monotonically with growing positive argument, i.e. since $z \geq 0$, the largest contribution to the integral in Eq. (5.49) results from the region close to $\tilde{\vartheta} = 0$ and $\tilde{x}_0 = \pi/2$. Hence, Φ and Φ' can be expanded for large arguments as $z \propto 1/(\kappa)^{2/3} \gg 1$

$$\Phi^2(z) = \frac{z}{3\pi}K^2_{1/3}\left(\frac{2}{3}z^{3/2}\right) \overset{z\to\infty}{\longrightarrow} \frac{z^{-1/2}}{4\pi}\mathrm{e}^{-\frac{4}{3}z^{3/2}}, \tag{5.52}$$

$$\Phi'^2(z) = \frac{z^2}{3\pi}K^2_{2/3}\left(\frac{2}{3}z^{3/2}\right) \overset{z\to\infty}{\longrightarrow} \frac{z^{1/2}}{4\pi}\mathrm{e}^{-\frac{4}{3}z^{3/2}} \tag{5.53}$$

with the modified Bessel functions of the second kind $K_\nu(x)$ [52]. After inserting the expressions above into Eq. (5.49) all functions dependent on ϑ and x_0 are expanded around $\tilde{\vartheta}$ and $\tilde{x}_0$. Then, after taking the leading contributions in the integration variables and subsequently carrying out the remaining integrals one ends up with

$$R^{2+1}_{\eta\gg1,\kappa\ll1} \approx \frac{\mathfrak{e}^2 a_0'^2 m}{8\pi}\frac{3\kappa}{8\sqrt{2}}\mathrm{e}^{-\frac{8}{3\kappa}}. \tag{5.54}$$

The equation above can now be compared to its 3+1 dimensional analogue given in Eq. (3.36). The main difference is manifested in the change of the power linked to the quantum nonlinearity parameter κ in the pre-exponential factor from 3/2 in QED to 1 in QED_{2+1}. This deviation is caused by the reduced dimensionality of the phase space as in both cases the integrand in the limit $\kappa \ll 1$ depends on κ solely

through the exponential function $\mathrm{e}^{-\frac{4}{3}z^{3/2}}$. Hence, since an integration over each variable provides a factor $\kappa^{1/2}$ and the rate in 2+1 dimensions does not depend on the variable responsible for a dimension orthogonal to the plane spanned by photon polarisations and propagation vectors ($\sigma = 1$), the expression above contains a power of 1/2 less in the quantum nonlinearity parameter when compared to Eq. (3.36).

Next, the $\kappa \gg 1$ limit is studied. To that end, beginning with Eq. (5.49), the substitutions $\kappa\mathrm{sin}(x_0) = p$ and $\mathrm{ch}(\vartheta) = u$ are performed and the involved Airy functions are written in terms of the modified Bessel functions of the second kind as it was shown in Eq. (5.52) leading to

$$R^{2+1}_{\eta\gg1,\kappa\gg1} \approx \frac{\mathfrak{e}^2 a_0'^2 m}{8\pi}\frac{16}{3\pi^2}\int_0^{\kappa}\frac{dp}{p\sqrt{\kappa^2-p^2}}\int_1^{\infty}\frac{du}{\sqrt{u^2-1}} \times\left[u^2K^2_{1/3}\left(\frac{4u^2}{3p}\right)+(u^2-1)K^2_{2/3}\left(\frac{4u^2}{3p}\right)\right], \quad (5.55)$$

while the integration over p is further divided into two intervals: $[0, p_0]$ and $[p_0, \kappa]$ with $p_0 \ll \kappa$. Then, the contribution from the first interval is negligible since $p/\kappa \ll 1$ holds and, as it is shown below, it scales with κ^{-1}

$$\int_0^{p_0}\frac{dp}{p\sqrt{\kappa^2-p^2}}... \approx \frac{1}{\kappa}\int_0^{p_0}\frac{dp}{p}... \sim \frac{p_0^{4/3}}{\kappa} \ll 1. \quad (5.56)$$

For the remaining integrations a subsequent substitution $t = 4u^2/3p$ (see the argument of the Bessel functions) is made, while leaving p unchanged. Consequently, one obtains

$$R^{2+1}_{\eta\gg1,\kappa\gg1} \approx \frac{\mathfrak{e}^2 a_0'^2 m}{8\pi}\frac{4}{\sqrt{3}\pi^2}\int_{p_0}^{\kappa}\frac{dp}{\sqrt{p}\sqrt{\kappa^2-p^2}}\int_{\frac{4}{3p}}^{\infty}dt \times\left[\frac{3p}{4}\sqrt{\frac{t}{\frac{3pt}{4}-1}}K^2_{1/3}(t)+\sqrt{\frac{\frac{3pt}{4}-1}{t}}K^2_{2/3}(t)\right], \quad (5.57)$$

which allows for exploiting the behaviour of $K_{1/3,2/3}(t)$ in various regimes in a more straight forward way. Having this goal in mind, the integration over t is split into two sectors:

$$\int_{4/3p}^{\infty}dt... = \int_{4/3p}^{t_0}dt... + \int_{t_0}^{\infty}dt... \quad (5.58)$$

with a parameter t_0 satisfying the following conditions

$$\frac{4}{3\kappa} \ll \frac{4}{3p_0} \ll t_0 \ll 1, \quad \frac{3\kappa t_0}{4} \gg \frac{3p_0 t_0}{4} \gg 1. \quad (5.59)$$

Let us consider firstly the contribution stemming from $[t_0, \infty]$, where $3pt/4 \gg 1$

holds and, as a consequence, the integral approximates

$$\int_{t_0}^{\infty} dt \left(\frac{3p}{4} \sqrt{\frac{t}{\frac{3pt}{4}-1}} K_{1/3}^2(t) + \sqrt{\frac{\frac{3pt}{4}-1}{t}} K_{2/3}^2(t) \right) \approx \sqrt{\frac{3p}{4}} \int_{t_0}^{\infty} dt \left(K_{1/3}^2(t) + K_{2/3}^2(t) \right) \approx \sqrt{\frac{3p}{4}} \frac{3\Gamma^2(\frac{2}{3})}{2^{2/3} t_0^{1/3}}. \quad (5.60)$$

For deriving the right hand side of the equation above the condition $t_0 \ll 1$ has been used and $\Gamma(x)$ stands for the gamma function [52].

Regarding the second contribution from Eq. (5.58) defined over $[4/3p, t_0]$: Here, since $t \ll 1$ applies, the small argument behaviour of the modified Bessel functions $K_\nu(t) \approx \Gamma(\nu)/2(t/2)^\nu$ [52] may be employed. Thus, taking advantage of the relations $4/3pt_0 \ll 1$ and $t_0 \ll 1$ the integration in t is carried out providing

$$\int_{4/3p}^{t_0} dt \left(\frac{3p}{4} \sqrt{\frac{t}{\frac{3pt}{4}-1}} K_{1/3}^2(t) + \sqrt{\frac{\frac{3pt}{4}-1}{t}} K_{2/3}^2(t) \right) \approx -\sqrt{\frac{3p}{4}} \frac{3\Gamma^2(\frac{2}{3})}{2^{2/3} t_0^{1/3}} + \frac{3^{5/6}\sqrt{\pi}}{2^{10/3}} \frac{\Gamma^2(\frac{2}{3})\Gamma(\frac{1}{3})}{\Gamma(\frac{11}{6})} p^{5/6} + \frac{3^{1/6}\sqrt{\pi}}{2^{5/3}} \frac{\Gamma^2(\frac{1}{3})\Gamma(-\frac{1}{3})}{\Gamma(\frac{1}{6})} p^{1/6}. \quad (5.61)$$

When the combined Eqs. (5.60) and (5.61) are inserted back into Eq. (5.57), which results in the dropping out of the ambiguous parameter t_0, as it should, and for the leading order in κ one obtains

$$R_{\eta \gg 1, \kappa \gg 1}^{2+1} \approx \frac{\mathfrak{e}^2 a_0'^2 m}{8\pi} \frac{3^{11/6}}{2^{1/3} 5\pi} \Gamma^2 \left(\frac{2}{3} \right) \kappa^{1/3}. \quad (5.62)$$

Similarly to the case of low quantum nonlinearity parameters, there are deviations in the expression above when compared to its 3+1 dimensional counterpart shown in Eq. (3.37) in subsection 3.1.2. In QED the rate in the studied limit shows a well known $\kappa^{2/3}$ behaviour, which provides insights on the applicability of the perturbation theory in the quantised field (see discussion below Eq. (3.41)) and leads to an establishment of a modified coupling in the strong fields $\alpha\kappa^{2/3}$. On contrary, in Eq. (5.62) the rate dependence on κ is given through an exponent of 1/3. Thus, the proper expansion parameter for QED$_{2+1}$ could read $g \sim \alpha_{2+1}\kappa^{1/3}$ whenever $g \ll 1$ holds. As for making a reliable statement on this issue a more sophisticated study of the next-to-leading order terms within the perturbative expansion [5, 105, 106, 107], which is beyond the scope of the present study, is required, the comment on the modified coupling provided above must be considered as a conjecture. However, owing to the superrenormalisable feature of the theory some interesting aspects can still be read off from Eq. (5.62). When assuming that κ in 2+1 dimensions corresponds to its 3+1 dimensional analogue and $\kappa \gg 1$ holds, the presence of the 1/3 exponent would induce a softer breakdown of the perturbation theory if $\alpha_{2+1} \sim \alpha$.

Conversely, if $\alpha_{2+1} \gg \alpha\kappa^{1/3}$, i.e. $\mathfrak{e}^2/(4\pi) \gg m\alpha\kappa^{1/3}$, the collapse in QED_{2+1} could be stronger than in QED.

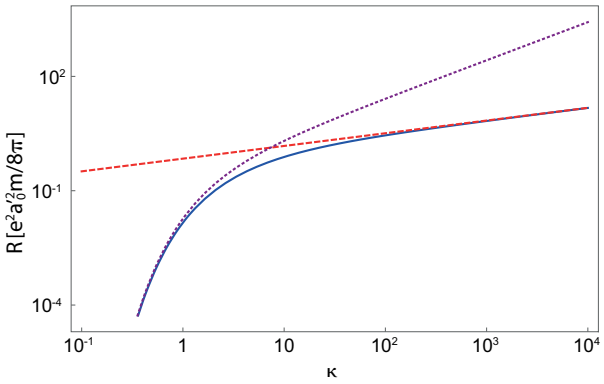

Figure 5.4: Comparison of the asymptotic rates in the limit of high intensity for $\kappa \ll 1$ (purple dotted) and $\kappa \gg 1$ (red dashed) with the pair production rate given in Eq. (5.49). This figure was originally published in Ref. [100].

In Fig. 5.4 the results of the present subsection are visualised as it shows the dependence of R^{2+1} on the quantum nonlinearity parameter κ for $\eta \gg 1$. The blue solid line represents numerically evaluated rates given in Eqs. (5.49) and Eqs. (5.51), whereas the small κ behaviour from Eq. (5.54) and large κ asymptote provided in Eq. (5.62) are shown as red dashed and purple dotted curves, correspondingly.

5.4 Summary

In the present chapter a study of the Breit-Wheeler pair creation in 2+1 dimensional Minkowski spacetime was presented. After a discussion on the applicability of the perturbative treatment and introduction of the field operators in the lowered dimensionality in the first section, the linear process was investigated. Moreover, in section 5.3 the Breit-Wheeler particle production resulting from the interaction of a weak quantised and a strong classical fields was shown. In this context, special attention was paid to the different intensity regimes of the strong field, which were compared to the calculation in the standard QED. Interestingly, some crucial differences caused by the dimensionality of the system were found. In the low intensity $\eta \ll 1$ domain the process rate, depending on the number of participating strong field photons, manifested a non-zero contribution at the energy threshold, where fermions are created with zero momentum. Thus, the probability for creating a pair with vanishing momentum is not zero for 2+1 dimensional systems, when an even number of strong field photons interacts with the weak field: a fact that will be studied further in the next chapter in another physical context given by the solid-state system of bandgapped graphene.

For $\eta \gg 1$ the particle rates, which conveniently depend on the quantum nonlinearity parameter κ, showed also an altered behaviour when compared to QED. To be more precise, the deviation occurred in the exponents of κ, which were lowered by 1/2 for $\kappa \ll 1$ and 1/3 for $\kappa \gg 1$. On the basis of the latter point, a conjecture on the breakdown of perturbation theory was provided and some comments on the modification of the coupling constant in the strong fields were discussed.

Chapter 6

Breit-Wheeler process in graphene

Building on the nonanticipated findings on the topic of Breit-Wheeler pair creation in a lowered 2+1 dimensional spacetime, which was considered in the previous chapter, here, the focus lies on an analogous process in a real physical system of graphene monolayers. The latter is well known as a low-energy test ground for QED processes as the electrons in this material at the vicinity of the Fermi surface show relativistic behaviour that can be described by a 2+1 dimensional Dirac-like equation of motion: A property that allowed for observation of Klein tunneling [108], Casimir force [109] or Coulomb supercriticality [110, 111] in this material. Moreover, graphene has drawn the attention of theoreticians in the context of the QED particle production as the interband transition of electrons in this system creates a hole in the valence band this way modelling a creation of quasiparticle-hole pairs. Since it can withstand high intensities, graphene represents a good candidate for experiments in strong electromagnetic fields. On that note, the Schwinger effect was thoroughly studied in gapless and bandgapped[1] graphene in Refs. [112, 113, 114, 115, 116, 117, 118, 119, 120], where a change in the pre-exponential factor from 2 in QED to 3/2 in graphene was found. Observe that the lowering of the pre-exponential factor stands in correspondence with the outcome for high intensity and quantum nonlinearity parameters in subsection 5.3.3. In this chapter the analogues of the linear and the three-photon Breit-Wheeler pair production taking place in graphene with a tiny bandgap are studied and compared to the consideration in QED_{2+1} as presented in subsection 5.3.2. Besides, the approach to the linear process provides an alternative channel with respect to section 4.2 for experimental observation of this effect. The three-photon reaction is discussed with reference to the previous chapter and allows for experimental verification of the striking changes to the rate on the energy threshold, which are caused by altered dimensionality. Lastly, the results presented here are based on Ref. [121] and on the corresponding Supplemental Material [122]. Moreover, the used unit system varies slightly from the one utilised earlier: While $\hbar = \epsilon_0 = 1$ still holds, the speed of light in vacuum c is restored.

[1]Since the introduction of a gap between the valence and the conduction bands is equivalent to the case of quasiparticles acquiring a non-zero mass, which reinforces the resemblance with QED_{2+1}, it will be also incorporated in the present study.

6.1 Graphene as a QED-like medium

Graphene is a solid state system assembled as a honeycomb lattice of carbon atoms, which lie in the (x, y)-plane and are connected by strong covalent $\sigma-$bonds according to a sp^2 hybridisation of $2s$, $2p_x$ and $2p_y$ orbitals [123]. The remaining electrons of the $2p_z$ ($\pi-$bond) orbitals, which are perpendicular to the plane and have weak overlaps, represent the dynamical degree of freedom and are responsible for the electronic and transport properties of graphene. A structure of this solid can be seen in Fig. 6.1. Here, the two base atoms A and B of the graphene unit cell are placed at $(0, h)$ and $(0, 0)$, respectively, with $h = a/\sqrt{3} = 0.142$ nm and two primitive lattice vectors (depicted in black)

$$\mathbf{a_1} = a\boldsymbol{e_x}, \quad \mathbf{a_2} = a\left(\frac{1}{2}\boldsymbol{e_x} + \frac{\sqrt{3}}{2}\boldsymbol{e_y}\right), \tag{6.1}$$

whereas the corresponding vectors of the reciprocal lattice read

$$\mathbf{b_1} = \frac{4\pi}{a}\left(\frac{1}{2}\boldsymbol{e_x} - \frac{\sqrt{3}}{2}\boldsymbol{e_y}\right), \quad \mathbf{b_2} = \frac{4\pi}{\sqrt{3}a}\boldsymbol{e_y}, \tag{6.2}$$

which were found by a relation $\mathbf{a_i b_j} = 2\pi\delta_{ij}$ with a Kronecker delta symbol δ_{ij}. The associated reciprocal lattice can be seen in Fig. 6.2 and, thus, it is also hexagonal. Moreover, the first Brillouin zone is depicted as a hexagon in the middle and has side length $l = \frac{4\pi}{3a}$. The vertices of the hexagon are denoted as $\boldsymbol{K}$ and $\boldsymbol{K}'$, which are two inequivalent points of the lattice as they can not be reached by the reciprocal lattice vectors.

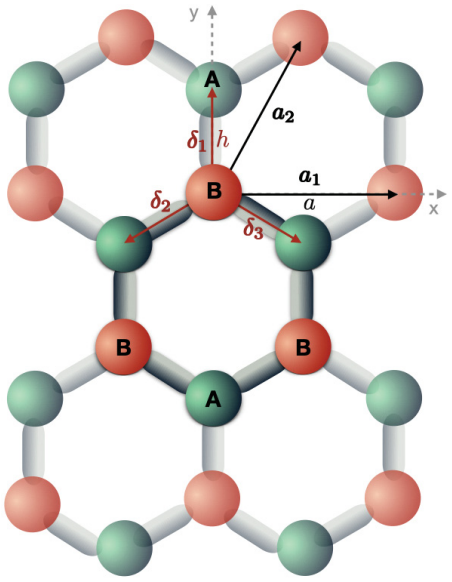

Figure 6.1: Monolayered graphene honeycomb lattice composed of two sublattices A and B.

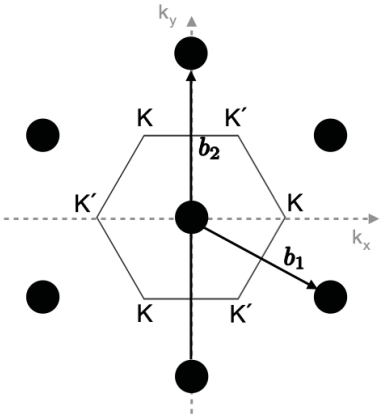

Figure 6.2: The first Brillouin zone of graphene with inequivalent points K and K'.

6.1.1 Massless graphene

The behaviour of the electrons in the non-hybridised p_z orbital is described further within the tight-binding approximation, which takes into account solely their interaction with the atoms in the nearest neighbourhood. Following

Fig. 6.1, the nearest neighbours of A and B are given by the atoms of the opposite sublattice and can be reached by the vectors

$$\boldsymbol{\delta_1} = \frac{a}{\sqrt{3}}\boldsymbol{e_y}, \quad \boldsymbol{\delta_2} = -\frac{a}{\sqrt{3}}\left(\frac{\sqrt{3}}{2}\boldsymbol{e_x} + \frac{1}{2}\boldsymbol{e_y}\right), \quad \boldsymbol{\delta_3} = \frac{a}{\sqrt{3}}\left(\frac{\sqrt{3}}{2}\boldsymbol{e_x} - \frac{1}{2}\boldsymbol{e_y}\right). \tag{6.3}$$

In this scenario the Hamiltonian representing an electron hopping from atom B to its nearest atoms A reads

$$\mathcal{H}_{TB} = -t \sum_{\boldsymbol{r};i=1,2,3;\sigma=\pm1} \left(\hat{c}_A^\dagger(\boldsymbol{r}+\boldsymbol{\delta_i},\sigma)\hat{c}_B(\boldsymbol{r},\sigma) + h.c.\right), \tag{6.4}$$

where $\hat{c}^{(\dagger)}_{A,B}(\boldsymbol{r},\sigma)$ stands for the annihilation (creation) operator of an electron with spin σ located at the position $\boldsymbol{r}$ in the sublattice A or B and

$$\hat{c}_{A,B}(\boldsymbol{r},\sigma) = \sum_{\boldsymbol{k}} \mathrm{e}^{i\boldsymbol{rk}}\hat{c}_{A,B}(\boldsymbol{k},\sigma), \tag{6.5}$$

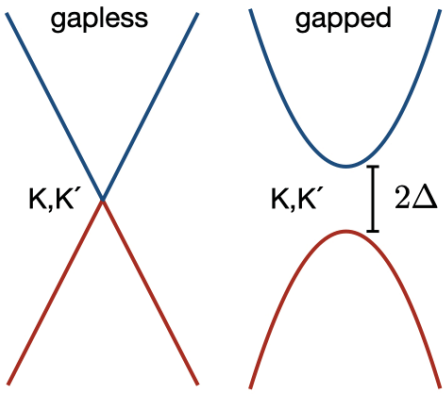

Figure 6.3: Valence and conduction bands for gapped (left) and gapless (right) grahene in the vicinity of K, K' points.

while $t \approx 2.8$ eV denotes the nearest neighbour hopping energy. From Eq. (6.4) two bands of graphene touching at the points $\boldsymbol{K}$ and $\boldsymbol{K'}$, which represent the Fermi surface of the system, can be derived. Moreover, near the Fermi points electrons show a for graphene characteristic relativistic behaviour that can be described by a Dirac-like equation with the speed of light c replaced by the Fermi velocity $v_F \approx c/300$, which makes this solid a suitable system for low-energy QED test ground. The dispersion relation for electrons in the vicinity of $\boldsymbol{K}$ and $\boldsymbol{K'}$ for a gapless system, which was discussed so far, can be seen in the left panel of Fig. 6.3. In this context, Eq. (6.4) can be written in the momentum representation and expanded around the $\boldsymbol{K}$, $\boldsymbol{K'}$ points. When taking into account the terms of up to the first order in the expansion parameter, the Hamiltonians for every Fermi point read [123]

$$\begin{aligned} \mathcal{H}_{\boldsymbol{K}} &= \sum_{\boldsymbol{p},\sigma=\pm1} \psi^\dagger_{\sigma\boldsymbol{K}}(v_F(\sigma_1 p_x + \sigma_2 p_y))\psi_{\sigma\boldsymbol{K}} \quad \text{and} \\ \mathcal{H}_{\boldsymbol{K'}} &= \sum_{\boldsymbol{p},\sigma=\pm1} \psi^\dagger_{\sigma\boldsymbol{K'}}(v_F(-\sigma_1 p_x + \sigma_2 p_y))\psi_{\sigma\boldsymbol{K'}} \end{aligned} \tag{6.6}$$

with the two-component irreducible spinors $\psi^T_{\sigma\boldsymbol{K}} = (\psi_{\sigma\boldsymbol{K}A}, \psi_{\sigma\boldsymbol{K}B})$, $\psi^T_{\sigma\boldsymbol{K'}} = (\psi_{\sigma\boldsymbol{K'}B}, \psi_{\sigma\boldsymbol{K'}A})$ combining the Bloch states associated with the two sublattices in

graphene linked to atoms A and B. This property, though arising from the underlying symmetry of the honeycomb lattice, resembles the electron spin and, thus, is assigned with the name pseudospin [124]. Additionally, the momentum $\boldsymbol{p} = (p_x, p_y)$ has to be understood relative to the $\boldsymbol{K}$ and $\boldsymbol{K'}$ points, which represented the points of the expansion, and satisfying the condition $|\boldsymbol{p}| \ll p_{\max} \approx |\boldsymbol{K}|, |\boldsymbol{K'}| \approx 3$ eV$/v_F$, while σ_i, $i = 1, 2$, stands for the Pauli matrices from appendix A.1.2.

6.1.2 Bandgapped graphene

Now, in order to model a system coming closest to QED$_{2+1}$, graphene with a tiny gap[2] (see the right panel of Fig. 6.3) is introduced. It is accounted for by adding a mass term $\Delta = m_g v_F^2$ in Eqs. (6.6), which leads to a relativistic dispersion relation for quasiparticles $\varepsilon_{\boldsymbol{p}} = \sqrt{v_F^2 \boldsymbol{p}^2 + \Delta^2}$ relative to the Fermi-level [120, 123]

$$\begin{aligned}
\mathcal{H}_{\boldsymbol{K}} &= \sum_{\boldsymbol{p},\sigma=\pm1} \psi^\dagger_{\sigma\boldsymbol{K}} (v_F(\sigma_1 p_x + \sigma_2 p_y) + \sigma_3 \Delta) \psi_{\sigma\boldsymbol{K}}, \\
\mathcal{H}_{\boldsymbol{K'}} &= \sum_{\boldsymbol{p},\sigma=\pm1} \psi^\dagger_{\sigma\boldsymbol{K'}} (v_F(-\sigma_1 p_x + \sigma_2 p_y) + \sigma_3 \Delta) \psi_{\sigma\boldsymbol{K'}}.
\end{aligned}$$

The equations above can be combined to a Hamiltonian [125]

$$\begin{aligned}
&\mathcal{H} = \sum_{\boldsymbol{p},\sigma} \bar{\Psi}_\sigma(t,\boldsymbol{p}) \left[v_F \tilde{\boldsymbol{\gamma}} \cdot \boldsymbol{p} + \Delta \right] \Psi_\sigma(t,\boldsymbol{p}) = \\
&\sum_{\boldsymbol{p},\sigma=\pm1} \left[\psi^\dagger_{\sigma,\boldsymbol{K}} (v_F(\sigma_1 p_x + \sigma_2 p_y) + \sigma_3 \Delta) \psi_{\sigma,\boldsymbol{K}} + \psi^\dagger_{\sigma,\boldsymbol{K'}} (v_F(\sigma_1 p_x + \sigma_2 p_y) - \sigma_3 \Delta) \psi_{\sigma,\boldsymbol{K'}} \right],
\end{aligned} \tag{6.7}$$

where $\bar{\Psi}_\sigma = \Psi^\dagger_\sigma \tilde{\gamma}^0$, $\Psi^T_\sigma = (\psi^T_{\sigma\boldsymbol{K}}, \psi^T_{\sigma\boldsymbol{K'}})$ is a four-component spinor and the gamma matrices $\tilde{\gamma}^\mu$ form a reducible 4×4 representation satisfying $\{\tilde{\gamma}^\mu, \tilde{\gamma}^\nu\} = 2g^{\mu\nu}\mathbb{1}_{4\times4}$ with the metric tensor $g^{\mu\nu} = \mathrm{diag}(1,-1,-1)$. Explicitly, they read $\tilde{\gamma}^\mu = \tau \otimes (\gamma^1, \gamma^2, \gamma^3)$ with $\tau = \sigma_3$, $\gamma^\mu = (\sigma_3, i\sigma_2, -i\sigma_1)$. Moreover, the matrices τ and γ^μ act in the spaces of $\boldsymbol{K}$, $\boldsymbol{K'}$ points and A, B sublattices, respectively.

While the first contribution in the second line of the expression above resembles the tight-binding Hamiltonian linked to the $\boldsymbol{K}$ point from Eq. (6.6), the second term differs from the standard representation associated with the point $\boldsymbol{K'}$. However, the latter can be achieved by developing the canonical transformations [123]

$$\psi^T_{\sigma,\boldsymbol{K}} = (\psi_{\sigma,\boldsymbol{K},A}, \psi_{\sigma,\boldsymbol{K},B}) \to \psi^T_{\sigma,\boldsymbol{K}}, \quad \psi^T_{\sigma,\boldsymbol{K'}} = (i\psi_{\sigma,\boldsymbol{K'},B}, -i\psi_{\sigma,\boldsymbol{K'},A}) \to \psi^T_{\sigma,\boldsymbol{K'}} \mathrm{e}^{(-i\pi\sigma_3/2)\sigma_1}. \tag{6.8}$$

[2] A gap in graphene can be induced through various experimental techniques such as epitaxial growth on suitable substrates, elastic strain or Rashba spin splittings on magnetic substrates [126, 127, 128, 129, 130]. The typical values for the gaps in such scenarios reach up to $\mathcal{O}(0.1)$ eV [131].

6.1.3 Effective action

In the present chapter an interaction of two high-intensity counterpropagating electromagnetic fields with four-potentials a and a', which propagate in 3+1 dimensional spacetime, with the electrons in graphene restricted to the $(\mathrm{x},\mathrm{y})-$plane will be studied. This system can be described by an effective action with $\alpha,\beta = 0,1,2,3$ and $x = (ct, \boldsymbol{x})$, $\boldsymbol{x} = (\mathrm{x},\mathrm{y})$ according to

$$S = \int d^3x d\mathrm{z} \left(-\frac{1}{4} f_{\alpha\beta}^2 - \frac{1}{2} f'_{\alpha\beta} f^{\alpha\beta} - \frac{1}{4} f'^2_{\alpha\beta} \right.$$
$$\left. + \delta(\mathrm{z}) \sum_{\sigma=\pm 1} \bar{\Psi}_\sigma(x,\mathrm{z}) \Big[i\tilde{\gamma}^0 \partial_t \; v_F \tilde{\gamma}^j \left(i\partial_j - \frac{e}{c} \mathcal{A}_j(x,\mathrm{z}) \right) - \Delta \Big] \Psi_\sigma(x,\mathrm{z}) \right), \quad (6.9)$$

where $\mathcal{A}_\alpha = a_\alpha + a'_\alpha$, $\mathcal{A}_0(x,\mathrm{z}) = 0$ is implied, $f^{(\prime)}_{\alpha\beta}$ refer to the associated field tensors $f^{(\prime)}_{\alpha\beta} = \partial_\alpha a^{(\prime)}_\beta - \partial_\beta a^{(\prime)}_\alpha$ and the derivatives read $\partial_{1,2} \equiv \partial/\partial\mathrm{x}, \partial/\partial\mathrm{y}$. Moreover, the gauge fields are on-shell, i.e. $\partial^\alpha f^{(\prime)}_{\alpha\beta} = 0$ with $a^{(\prime)}_\alpha(t,\boldsymbol{\infty}) \to 0$ and the spinors, the $\tilde{\gamma}-$matrices as well as the remaining parameters are specified below Eq. (6.7), whereas the repeated indices $j = 1,2$ mean summation.

From the interaction term $e\frac{v_F}{c} \int d^3x \, \boldsymbol{J} \cdot \boldsymbol{\mathcal{A}}(x)$ with the current density

$$\boldsymbol{J}(x) = \sum_{\sigma=\pm 1} \bar{\Psi}_\sigma(x) \tilde{\boldsymbol{\gamma}} \Psi_\sigma(x) = \sum_{\sigma=\pm 1} \Big[\bar{\psi}_{\sigma\boldsymbol{K}}(x) \boldsymbol{\gamma} \psi_{\sigma\boldsymbol{K}}(x) + \bar{\psi}_{\sigma\boldsymbol{K}'}(x) \boldsymbol{\gamma} \psi_{\sigma\boldsymbol{K}'}(x) \Big], \quad (6.10)$$

which is a vector lying in the plane of graphene, the scattering operator is obtained

$$\hat{S}_g = \mathcal{T} \left[\exp\left(ie\frac{v_F}{c} \sum_{\sigma=\pm 1} \int d^3x \; \hat{\bar{\psi}}_{\sigma\boldsymbol{K}} \; \boldsymbol{\gamma}\cdot(\boldsymbol{a} + \hat{\boldsymbol{a}}') \hat{\psi}_{\sigma\boldsymbol{K}} + \hat{\bar{\psi}}_{\sigma\boldsymbol{K}'} \; \boldsymbol{\gamma}\cdot(\boldsymbol{a} + \hat{\boldsymbol{a}}') \hat{\psi}_{\sigma\boldsymbol{K}'} \right) \right] \quad (6.11)$$

with $\hat{\bar{\psi}}_{\sigma\boldsymbol{K},\boldsymbol{K}'} = \hat{\psi}^\dagger_{\sigma\boldsymbol{K},\boldsymbol{K}'} \gamma^0$. Here, it is assumed that the intensity of a is much larger than a', and, thus, the stronger field can be incorporated via a coherent states treatment (see details in subsection 2.2.2), while the weaker field is quantised. Besides, all fields occurring in the equation above are evaluated at $\mathrm{z} = 0$ and have to be understood as operators within the interaction picture. Moreover, a remark regarding the energy scale is in order: since the Hamiltonian in Eq. (6.7) leading to the expression above was derived for the energies below 3 eV, this restriction holds also for the studied processes.

6.1.4 Electromagnetic fields

Since the interaction with electrons takes place in a plane, the wave vectors of both fields will also be bound to the graphene sheet. Moreover, the electromagnetic fields considered here are taken in Coulomb gauge ($a'_0(x) = 0$ and $a_0(x) = 0$) with $\boldsymbol{\nabla}\cdot\boldsymbol{a}(x) = \lim_{\mathrm{z}\to 0} \boldsymbol{\nabla}\cdot\boldsymbol{a}(x,\mathrm{z}) = 0$, $\boldsymbol{\nabla}\cdot\boldsymbol{a}'(x) = \lim_{\mathrm{z}\to 0} \boldsymbol{\nabla}\cdot\boldsymbol{a}'(x,\mathrm{z}) = 0$. In such a scenario,

the plane-wave expansion of the quantised weak electromagnetic field looks similar to Eq. (2.7)

$$\hat{a}'(x) = \sum_{k,\lambda=\parallel,\perp} \frac{\epsilon'_{k,\lambda} c}{\sqrt{2\omega' V_\gamma}} \left[\hat{a}_{k,\lambda} e^{-ikx} + \hat{a}^\dagger_{k,\lambda} e^{ikx} \right] \tag{6.12}$$

with a normalisation volume V_γ and $kx \equiv \omega t - \boldsymbol{k}\cdot\boldsymbol{x}$, $\boldsymbol{x} = (\mathrm{x}, \mathrm{y})$, where $k^\mu = (\omega/c, \boldsymbol{k})$. Here, the orthogonal transversal polarisation vectors $\epsilon'_{\parallel,\perp}$ are understood as parallel and perpendicular with respect to the graphene monolayer.

The strong classical field is linearly polarised with $a_\mu(x) = a_0 \epsilon_\mu \cos(kx)$. When taking the field polarisation under an angle θ to the graphene plane, $a_\mu(x)$ can be decomposed in terms of the perpendicular and parallel parts $a(x) = a_\perp(x) + a_\parallel(x)$ with $a_\perp(x) = a_0 \sin(\theta)\epsilon_\perp \cos(kx)$ and $a_\parallel(x) = a_0 \cos(\theta)\epsilon_\parallel \cos(kx)$. Then, the orthogonal pieces $a_\perp(x)$ are projected out[3] by the interaction given in Eq. (6.10) and above it, leaving the system with only one degree of freedom (similarly to QED_{2+1} in subsection 5.1.1). Thus, the problem can be considered as the one with fields of polarisation laying in the plane with $\epsilon_\parallel \cos(\theta) \equiv \epsilon_\parallel$ denoting the projection of the polarisation onto the graphene surface. Lastly, it is important to point out that regardless the resemblance with QED_{2+1} the dimensions of both the coupling strength and the electromagnetic field are associated with $3+1$ dimensions. The latter statement holds since the considered setup represents a real physical system embedded in the 3+1 dimensional spacetime.

6.1.5 Quasi-fermions

The fields $\psi_{\sigma,\boldsymbol{K}}(x)$ and $\psi_{\sigma,\boldsymbol{K}'}(x)$ stem from the solutions of the free Dirac-like equations

$$\left[i\gamma^0\partial_t + iv_F\gamma^j\partial_j - \Delta \right] \psi_{\sigma,\boldsymbol{K}}(x) = 0, \quad \left[i\gamma^0\partial_t + iv_F\gamma^j\partial_j + \Delta \right] \psi_{\sigma,\boldsymbol{K}'}(x) = 0 \tag{6.13}$$

denoting the behaviour of the quasi-particles at the degeneracy points $\boldsymbol{K}$ and $\boldsymbol{K}'$ (see Eq. (6.7)). These are solved, similarly to subsection 5.1.2, by a plane-wave ansatz with the elementary spinors

$$\begin{aligned} v_{\boldsymbol{K}'}(\boldsymbol{p}) \equiv u_{\boldsymbol{K}}(\boldsymbol{p}) &= \sqrt{\frac{\varepsilon_{\boldsymbol{p}} + \Delta}{2\Delta}} \begin{pmatrix} 1 \\ \frac{v_F(p_1+ip_2)}{\varepsilon_{\boldsymbol{p}}+\Delta} \end{pmatrix}, \\ u_{\boldsymbol{K}'}(\boldsymbol{p}) \equiv v_{\boldsymbol{K}}(\boldsymbol{p}) &= \sqrt{\frac{\varepsilon_{\boldsymbol{p}} + \Delta}{2\Delta}} \begin{pmatrix} \frac{v_F(p_1-ip_2)}{\varepsilon_{\boldsymbol{p}}+\Delta} \\ 1 \end{pmatrix} \end{aligned} \tag{6.14}$$

fulfilling the relations $u_{\boldsymbol{K}}(\boldsymbol{p})\bar{u}_{\boldsymbol{K}}(\boldsymbol{p}) = \frac{(\gamma^0\varepsilon_{\boldsymbol{p}} - v_F\boldsymbol{\gamma}\cdot\boldsymbol{p} + \Delta)}{2\Delta}$, $v_{\boldsymbol{K}}(\boldsymbol{p})\bar{v}_{\boldsymbol{K}}(\boldsymbol{p}) = \frac{(\gamma^0\varepsilon_{\boldsymbol{p}} - v_F\boldsymbol{\gamma}\cdot\boldsymbol{p} - \Delta)}{2\Delta}$.

When quantised, the corresponding plane-wave expansion of the field operator

[3] The same argument holds also for the weaker field with $a'_\perp(x)$.

$\psi_{\sigma,\boldsymbol{K}}(x)$ reads

$$\hat{\psi}_{\sigma,\boldsymbol{K}}(x) = \sum_{\boldsymbol{p}} \sqrt{\frac{\Delta}{\varepsilon_{\boldsymbol{p}} A}} \left[\hat{b}_{\sigma,\boldsymbol{K}}(\boldsymbol{p}) u_{\boldsymbol{K}}(\boldsymbol{p}) \mathrm{e}^{-ipx} \ + \hat{d}^{\dagger}_{\sigma,\boldsymbol{K}}(\boldsymbol{p}) v_{\boldsymbol{K}}(\boldsymbol{p}) \mathrm{e}^{ipx} \right] \tag{6.15}$$

with $px = \varepsilon_{\boldsymbol{p}} t - \boldsymbol{p} \cdot \boldsymbol{x}$ and normalised to one particle in the area A. Here, $\hat{b}^{(\dagger)}_{\sigma,\boldsymbol{K}}(\boldsymbol{p})$ and $\hat{d}^{(\dagger)}_{\sigma,\boldsymbol{K}}(\boldsymbol{p})$ stand for the annihilation (creation) operators for the quasiparticle (excited valence electron) and the hole at the Fermi point $\boldsymbol{K}$, respectively, with $b_{\sigma,\boldsymbol{K}}(\boldsymbol{p})|0\rangle = d_{\sigma,\boldsymbol{K}}(\boldsymbol{p})|0\rangle = 0$. Followingly, the field operators satisfy the nonvanishing equal time anticommutation relations

$$\{\hat{\psi}_{\sigma,\boldsymbol{K}}(t,\boldsymbol{x}), \hat{\psi}^{\dagger}_{\sigma',\boldsymbol{K}'}(t,\boldsymbol{x}')\} = \delta_{\sigma,\sigma'}\delta_{\boldsymbol{K},\boldsymbol{K}'}\delta^{(2)}(\boldsymbol{x}-\boldsymbol{x}'). \tag{6.16}$$

The plane-wave expansion of the field $\psi_{\sigma,\boldsymbol{K}'}(x)$ is obtained from Eq. (6.15) by replacing $\boldsymbol{K} \to \boldsymbol{K}'$, while two additional sets of the second quantisation operators relative to the $\boldsymbol{K}'$ point have to be incorporated with $b_{\sigma,\boldsymbol{K}'}(\boldsymbol{p})|0\rangle = d_{\sigma,\boldsymbol{K}'}(\boldsymbol{p})|0\rangle = 0$. Moreover, the operators need to preserve the corresponding spin and valley (the latter distinguishes between the two inequivalent points $\boldsymbol{K}$ and $\boldsymbol{K}'$) quantum numbers. Thus, $\{b_{\sigma,\boldsymbol{K}}(\boldsymbol{p}), b^{\dagger}_{\sigma',\boldsymbol{K}'}(\boldsymbol{p}')\} = \delta_{\sigma,\sigma'}\delta_{\boldsymbol{K},\boldsymbol{K}'}\delta_{\boldsymbol{p},\boldsymbol{p}'}$, $\{d_{\sigma,\boldsymbol{K}}(\boldsymbol{p}), d^{\dagger}_{\sigma',\boldsymbol{K}'}(\boldsymbol{p}')\} = \delta_{\sigma,\sigma'}\delta_{\boldsymbol{K},\boldsymbol{K}'}\delta_{\boldsymbol{p},\boldsymbol{p}'}$ must apply. In addition, the free propagators for graphene in momentum representation result

$$S_{\boldsymbol{K}}(\varepsilon,\boldsymbol{p}) = \frac{i}{\gamma^0\varepsilon - v_F\boldsymbol{\gamma}\cdot\boldsymbol{p} - \Delta + i0^+}, \quad S_{\boldsymbol{K}'}(\varepsilon,\boldsymbol{p}) = \frac{i}{\gamma^0\varepsilon - v_F\boldsymbol{\gamma}\cdot\boldsymbol{p} + \Delta + i0^+}. \tag{6.17}$$

6.2 Breit-Wheeler creation of the quasipairs

Next, the creation processes of a quasiparticle and a hole with energies and momenta $(\varepsilon_{\boldsymbol{p}_-}, \boldsymbol{p}_-)$ and $(\varepsilon_{\boldsymbol{p}_+}, \boldsymbol{p}_+)$ from two electromagnetic fields a and a' with the wave vectors k and k', correspondingly, in a graphene sheet will be discussed. The scheme of the setup is displayed in Fig. 6.4. Here, in terms of the modified intensity parameters $\eta_g^{(\prime)} = |e|a_0^{(\prime)}/(m_g v_F c)$, the field amplitudes are supposed to fulfil the conditions $\eta_g \gg \eta_g'$ and $\eta_g, \eta_g' \ll 1$ simultaneously. The latter restriction is required for the perturbative treatment in both fields, which is pursued, since the Furry picture approach relying on the incorporation of the Volkov states as the exact solutions of the Dirac equation in plane-wave electromagnetic fields (see section 2.4) is not applicable in graphene. This problematic relies on the fact that, due to the asymmetry introduced by the Fermi velocity v_F, the corresponding Dirac-like equation in graphene is not solved by Volkov states [132, 133]. Moreover, the intensity of a is chosen sufficiently large for the strong field procedure involving coherent states to apply and, in this context, the transition amplitude reads

$$\langle 1_{\boldsymbol{p}_+}; 1_{\boldsymbol{p}_-} | \hat{S}_g[\hat{\psi}, \hat{\bar{\psi}}, \hat{a}' + a] | 1_{k',\epsilon'} \rangle \tag{6.18}$$

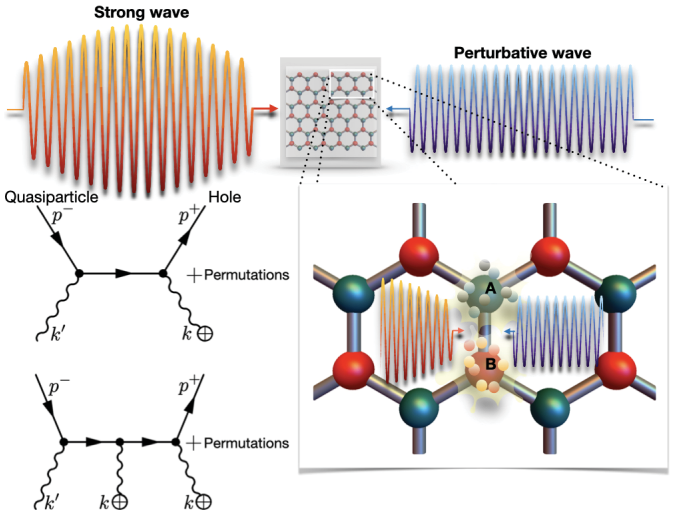

Figure 6.4: Scheme of the Breit-Wheeler-type production of Dirac-like quasipairs in graphene. The Feynman diagrams for two- and three-photon processes are shown on the left. A variation of this figure was originally published in Ref. [121].

with the scattering operator from Eq. (6.11). Here, one is interested in the two- and three-photon creation of quasiparticle-hole pairs. For the respective Feynman diagrams see the left panel of Fig. 6.4. Correspondingly, the processes are described by $\hat{S}_g^{(2)}$ and $\hat{S}_g^{(3)}$ contributions in the scattering operator expansion (compare to Eqs. (2.5) and (2.6)). Notice that the production of quasipairs from one photon is energetically forbidden, in similarity with QED, in gapped graphene monolayers. Conversely, in the gapless system the tree level process represents a leading-order term [134, 135]. Besides, when calculating the rates of the discussed processes, it is sufficient to take into account only a contribution from one of the Fermi points and spin configurations and multiply the outcome by the spin-valley degeneracy number, which is equal to $N_f = 4$. This simplification holds as the result is not dependent on the spin of the excited valence electron and on the sign in front of Δ (corresponding to $\boldsymbol{K}$ or $\boldsymbol{K}'$, see Eqs. (6.13)), because the rates calculated further only depend on Δ^{2n} with an integer n.

6.2.1 Linear quasipair creation

Having all these details in mind, for the two-photon transition amplitude resulting from the first contribution in Eq. (6.11) for $\boldsymbol{K}$ and $\sigma = +1$ one obtains

$$S_{fi} = \langle 1_{\boldsymbol{p}_+}; 1_{\boldsymbol{p}_-} | \hat{S}_g^{(2)} | 1_{k',\epsilon'} \rangle = -(2\pi)^3 \sqrt{\frac{\Delta^2}{\varepsilon_{\boldsymbol{p}_+}\varepsilon_{\boldsymbol{p}_-}A^2}} \frac{e^2 a_0 a_0' v_F^2}{4c^2} \mathcal{M}_1 \times \delta(\varepsilon_{\boldsymbol{p}_+} + \varepsilon_{\boldsymbol{p}_-} - \omega - \omega') \delta^{(2)}(\boldsymbol{p}_+ + \boldsymbol{p}_- - \boldsymbol{k} - \boldsymbol{k}'), \quad (6.19)$$

where the δ-functions encode the energy-momentum conservation and the relation $\sqrt{c^2/2\omega' V_\gamma} = a_0'/2$ was used[4]. Besides, the matrix element reads

$$\mathcal{M}_1 = \bar{u}_{\boldsymbol{K}}(\boldsymbol{p}_-)\left[\not{\epsilon}' S_{\boldsymbol{K}}(\omega - \varepsilon_{\boldsymbol{p}_+}, \boldsymbol{k} - \boldsymbol{p}_+)\not{\epsilon} + \not{\epsilon} S_{\boldsymbol{K}}(\omega' - \varepsilon_{\boldsymbol{p}_+}, \boldsymbol{k}' - \boldsymbol{p}_+)\not{\epsilon}'\right] v_{\boldsymbol{K}}(\boldsymbol{p}_+), \quad (6.20)$$

while the usual slash notation for products with $\gamma-$matrices is implied. However, here, the latter are $2\times 2-$dimensional and defined as it is shown in appendix A.1.2.

The rate of the quasipair production per unit area is obtained by squaring the transition amplitude, dividing it through the interaction time T and the normalisation area A while integrating over the density of final states and multliplying with the degeneracy number N_f

$$R^g = N_f \int \frac{A\, d^2p_+}{(2\pi)^2} \int \frac{A\, d^2p_-}{(2\pi)^2} \frac{|S_{fi}|^2}{TA} \ . \quad (6.21)$$

Here, it is important to point out that the field frequencies have to be chosen such that the integrals remain restricted to the regions where $|\boldsymbol{p}_\pm| \ll p_{\max}$ holds.

For the linear process, the equation above contains the term $|\mathcal{M}_1|^2$, which with help of spinor properties displayed below Eq. (6.14) can be rewritten as a trace over a $2\times 2-$dimensional matrix

$$\begin{aligned}|\mathcal{M}_1|^2 = \frac{1}{4\Delta^2}\mathrm{Tr}\Big[&\Big(\not{\epsilon}' S_{\boldsymbol{K}}(\omega - \varepsilon_{\boldsymbol{p}_+}, \boldsymbol{k} - \boldsymbol{p}_+)\not{\epsilon} + \not{\epsilon} S_{\boldsymbol{K}}(\omega' - \varepsilon_{\boldsymbol{p}_+}, \boldsymbol{k}' - \boldsymbol{p}_+)\not{\epsilon}'\Big) \\ &\times (\gamma^0 \varepsilon_{\boldsymbol{p}_+} - v_F \boldsymbol{\gamma}\cdot\boldsymbol{p}_+ - \Delta)\Big(\not{\epsilon} S_{\boldsymbol{K}}(\omega - \varepsilon_{\boldsymbol{p}_+}, \boldsymbol{k} - \boldsymbol{p}_+)\not{\epsilon}' + \not{\epsilon}' S_{\boldsymbol{K}}(\omega' - \varepsilon_{\boldsymbol{p}_+}, \boldsymbol{k}' - \boldsymbol{p}_+)\not{\epsilon}\Big) \\ &\times (\gamma^0 \varepsilon_{\boldsymbol{p}_-} - v_F \boldsymbol{\gamma}\cdot\boldsymbol{p}_- + \Delta)\Big]. \quad (6.22)\end{aligned}$$

It is noteworthy that, if the final state is chosen relative to the $\boldsymbol{K}'$ point, $|\mathcal{M}_1|^2$ would contain $S_{\boldsymbol{K}'}$ rather than $S_{\boldsymbol{K}}$ and the first bracket in the second line would exchange its position with the one given in the final line. However, the equation above turns out to be invariant under such replacement and, after calculating the traces with help of relations from appendix A.1.2, reads

$$|\mathcal{M}_1|^2 = \frac{1}{4\Delta^2}\left[C(k,k') + D(k) + D(k')\right] \quad (6.23)$$

[4]This transition resembles a multiplication of the transition amplitude with $\sqrt{\mathcal{N}_\parallel} = \sqrt{\frac{2\omega' V_\gamma}{c^2}\frac{a_0'^2\cos^2(\theta')}{4}}$, where $\mathcal{N}_\parallel$ stands for the number of photons in the beam with parallel polarisation assuming a generalised geometry with a weak field polarisation having an angle θ' to the graphene surface (see discussion below Eq. (6.12)). For the case of field polarisation lying in the $(\mathrm{x},\mathrm{y})-$ plane, $\theta' = 0$ and the expression provided in the text holds.

with

$$C(k,k') = \frac{2}{[(k'k') - 2(k'p_+)][(kk) - 2(kp_+)]} \{2(k'p_-)(kp_+) + 2(k'p_+)(kp_-) \\ +8(p_-p_+)(kp_+) + 8(p_-p_+)(kp_-) - 10(kk')(p_-p_+) \\ +\Delta^2[8(p_-p_+) - 4(kp_-) - 4(k'p_-) + 12(kp_+) + 12(k'p_+) - 10(kk')] - 8\Delta^4\} \quad (6.24)$$

and

$$D(k) = \frac{1}{[(kk) - 2(kp_+)]^2} \{4(kp_-)(kp_+) - 2(kk)(p_-p_+) \\ -\Delta^2[8(p_-p_+) - 24(kp_+) - 8(kp_-) + 18(kk)] - 24\Delta^4\}. \quad (6.25)$$

Here, the notation $(kp) = \omega\varepsilon_{\boldsymbol{p}} - v_F^2/c\ \boldsymbol{k}\cdot\boldsymbol{p}$ was introduced. Thus, it can be seen that the Lorentz invariance in the products is broken by the presence of the Fermi velocity. Moreover, the squared transition amplitude is invariant under a transition $\Delta \to -\Delta$.

Now, the equations above combined with Eq. (6.19) can be inserted into the defining expression for the rate from Eq. (6.21), which can be written in polar coordinates and integrated using the three $\delta-$functions. In the present context, a particularization to the case with $\omega = \omega'$ is assumed, such that $\boldsymbol{p} \equiv \boldsymbol{p}_+ = -\boldsymbol{p}_-$ applies[5] and $(kp) = \omega^2 - \omega v_F^2/c\ |\boldsymbol{p}|\cos(\varphi)$, $|\boldsymbol{p}| = \sqrt{\omega^2 - \Delta^2}/v_F$ hold. Then, the remaining integration is carried out and the rate per area in terms of the Mandelstam variable $s = \omega/\Delta$ reads

$$R_1^g = \frac{\eta_g'^2\eta_g^2 m_g^3 c^4}{8s^4} \frac{F(s,\beta)}{(1+\beta^2)G(s,\beta)} \quad (6.26)$$

with $\beta = v_F/c$ and

$$F(s,\beta) = -s^3(1+\beta^2)G(s,\beta) + s^6(1-\beta^2)^2(1+\beta^4) \\ + 2s^4\beta^2[3 + 2\beta^2 - 5\beta^4 + 8\beta^6] - 32\beta^6 - 16s^2\beta^6(\beta^2 - 3), \quad (6.27)$$

$$G(s,\beta) = [s^2(1-\beta^2)^2 + 4\beta^2]^{3/2}. \quad (6.28)$$

As one would expect, the rate above vanishes at the energy threshold ($s = 1$) and for $v_F = c = 1$ it equals to the corresponding expression derived in the framework of QED_{2+1} in Eq. (5.39). Moreover, in the limit $v_F/c \ll 1$, which is valid as $v_F \approx c/300 \ll c$, the rate of the process approximates

$$R_1^g \approx \eta_g^2\eta_g'^2 m_g^3 v_F^4 \frac{\mathfrak{r}^2(4+\mathfrak{r}^2)}{4(1+\mathfrak{r}^2)^{\frac{5}{2}}}, \quad (6.29)$$

[5]Following the conservation of energy and momentum in graphene provided by the $\delta-$functions, the latter can be fulfilled by the quasiparticles alone, without participation of the ionic lattice to absorb the recoil momentum.

where $\mathfrak{r} = |\boldsymbol{p}|/(m_g v_F)$ denotes a dimensionless parameter related to s through $\mathfrak{r} = \sqrt{s^2-1}$.

6.2.2 Three-photon process

In reference to the unanticipated results from the QED_{2+1} calculation from subsection 5.3.2, a particular interest in this section lies on the rate describing the production of quasipairs driven by an interaction of two classical photons with the quantised field (see lower Feynman diagram in Fig. 6.4). When considering the created quasiparticle-hole pair relative to the $\boldsymbol{K}$ point and $\sigma = 1$, the corresponding S-matrix element results from the third order term in the expansion of the scattering operator $\hat{S}_g^{(3)}$ when taking into account only the first term in Eq. (6.11)

$$S_{fi} = \langle 1_{\boldsymbol{p}_+}; 1_{\boldsymbol{p}_-}|\hat{S}_g^{(3)}|1_{k',\epsilon'}\rangle = -i(2\pi)^3\sqrt{\frac{\Delta^2}{\varepsilon_{\boldsymbol{p}_+}\varepsilon_{\boldsymbol{p}_-}A^2}}\frac{e^3a_0^2a_0'v_F^3}{8c^3}\,\mathcal{M}_2 \\ \times\,\delta(\varepsilon_{\boldsymbol{p}_+}+\varepsilon_{\boldsymbol{p}_-}-2\omega-\omega')\delta^{(2)}(\boldsymbol{p}_+ + \boldsymbol{p}_- - 2\boldsymbol{k}-\boldsymbol{k}') \quad (6.30)$$

with the amplitude given by

$$\mathcal{M}_2 = \bar{u}_{\boldsymbol{K}}(\boldsymbol{p}_-)\left[\not{\epsilon}S_{\boldsymbol{K}}(\varepsilon_{\boldsymbol{p}_-}-\omega,\boldsymbol{p}_- - \boldsymbol{k})\not{\epsilon}S_{\boldsymbol{K}}(\omega'-\varepsilon_{\boldsymbol{p}_+},\boldsymbol{k}'-\boldsymbol{p}_+)\not{\epsilon}'\right. \\ +\not{\epsilon}S_{\boldsymbol{K}}(\varepsilon_{\boldsymbol{p}_-}-\omega,\boldsymbol{p}_- - \boldsymbol{k})\not{\epsilon}'S_{\boldsymbol{K}}(\omega-\varepsilon_{\boldsymbol{p}_+},\boldsymbol{k}-\boldsymbol{p}_+)\not{\epsilon} \\ \left.+\not{\epsilon}'S_{\boldsymbol{K}}(\varepsilon_{\boldsymbol{p}_-}-\omega',\boldsymbol{p}_- - \boldsymbol{k}')\not{\epsilon}S_{\boldsymbol{K}}(\omega-\varepsilon_{\boldsymbol{p}_+},\boldsymbol{k}-\boldsymbol{p}_+)\not{\epsilon}\right]v_{\boldsymbol{K}}(\boldsymbol{p}_+). \quad (6.31)$$

When taking a careful look at the expression above, it can be seen that, conversely to the fully perturbative treatment involving three quantised photons with six contributions (see for instance the orthopositronium decay in [136]), only three terms are present above. The reason for this deviation lies in the coherent nature of the strong field description as the photons stemming from this field are nondistinguishable. Additionally, the squared amplitude needed for the calculation of the rate reads

$$|\mathcal{M}_2|^2 = \frac{1}{4\Delta^2}\mathrm{Tr}\Big[\left[\not{\epsilon}S_{\boldsymbol{K}}(\varepsilon_{\boldsymbol{p}_-}-\omega,\boldsymbol{p}_- - \boldsymbol{k})\not{\epsilon}S_{\boldsymbol{K}}(\omega'-\varepsilon_{\boldsymbol{p}_+},\boldsymbol{k}'-\boldsymbol{p}_+)\not{\epsilon}'\right. \\ +\not{\epsilon}S_{\boldsymbol{K}}(\varepsilon_{\boldsymbol{p}_-}-\omega,\boldsymbol{p}_- - \boldsymbol{k})\not{\epsilon}'S_{\boldsymbol{K}}(\omega-\varepsilon_{\boldsymbol{p}_+},\boldsymbol{k}-\boldsymbol{p}_+)\not{\epsilon} \\ \left.+\not{\epsilon}'S_{\boldsymbol{K}}(\varepsilon_{\boldsymbol{p}_-}-\omega',\boldsymbol{p}_- - \boldsymbol{k}')\not{\epsilon}S_{\boldsymbol{K}}(\omega-\varepsilon_{\boldsymbol{p}_+},\boldsymbol{k}-\boldsymbol{p}_+)\not{\epsilon}\right](\gamma^0\varepsilon_{\boldsymbol{p}_+}-v_F\boldsymbol{\gamma}\cdot\boldsymbol{p}_+-\Delta) \\ \times\left[\not{\epsilon}'S_{\boldsymbol{K}}(\omega'-\varepsilon_{\boldsymbol{p}_+},\boldsymbol{k}'-\boldsymbol{p}_+)\not{\epsilon}S_{\boldsymbol{K}}(\varepsilon_{\boldsymbol{p}_-}-\omega,\boldsymbol{p}_- - \boldsymbol{k})\not{\epsilon}\right. \\ +\not{\epsilon}S_{\boldsymbol{K}}(\omega-\varepsilon_{\boldsymbol{p}_+},\boldsymbol{k}-\boldsymbol{p}_+)\not{\epsilon}'S_{\boldsymbol{K}}(\varepsilon_{\boldsymbol{p}_-}-\omega,\boldsymbol{p}_- - \boldsymbol{k})\not{\epsilon} \\ \left.+\not{\epsilon}S_{\boldsymbol{K}}(\omega-\varepsilon_{\boldsymbol{p}_+},\boldsymbol{k}-\boldsymbol{p}_+)\not{\epsilon}S_{\boldsymbol{K}}(\varepsilon_{\boldsymbol{p}_-}-\omega',\boldsymbol{p}_- - \boldsymbol{k}')\not{\epsilon}'\right](\gamma^0\varepsilon_{\boldsymbol{p}_-}-v_F\boldsymbol{\gamma}\cdot\boldsymbol{p}_-+\Delta)\Big], \quad (6.32)$$

which also contains a trace over a 2×2 matrix.

Next, in order to obtain the rate of the three-photon process the equation above with the corresponding square of the transition amplitude is inserted into Eq. (6.21).

Then, similarly to the previous subsection, $\omega' = 2\omega$ with $\boldsymbol{p} \equiv \boldsymbol{p}_+ = -\boldsymbol{p}_-$ is assumed and three of the integrals are carried out by the $\delta-$functions, whereas the remaining integration is specified in polar coordinates with $(kp) = 2\omega^2 - \omega v_F^2/c\ |\boldsymbol{p}|\cos(\varphi)$, $|\boldsymbol{p}| = \sqrt{4\omega^2 - \Delta^2}/v_F$. As expected from Eq. (6.32), the resulting expression for the process rate turns out to be quite tedious and, therefore, is handled numerically. However, when expanded up to the second order in β, in terms of the dimensionless momentum parameter the latter reads

$$R_2^g \approx \frac{\eta_g^4 \eta_g'^2 m_g^3 v_F^4}{729(1+\mathfrak{r}^2)^{\frac{11}{2}}}(72 - 96\beta^2 + \mathfrak{r}^8(306 - 50\beta^2) - 1404\mathfrak{r}^4(-1+3\beta^2) + 52\mathfrak{r}^2(-9+20\beta^2) - 6\mathfrak{r}^6(-375+358\beta^2)) \quad (6.33)$$

and, thus, for $v_F/c \ll 1$ one obtains

$$R_2^g \approx \eta_g^4 \eta_g'^2 m_g^3 v_F^4 \frac{2(4 - 30\mathfrak{r}^2 + 108\mathfrak{r}^4 + 17\mathfrak{r}^6)}{81(1+\mathfrak{r}^2)^{\frac{9}{2}}} \overset{\mathfrak{r}\to 0}{\to} \frac{8\eta_g^4 \eta_g'^2 m_g^3 v_F^4}{81}. \quad (6.34)$$

Here, the scaling in the intensity parameters $\propto \eta_g'^2$ and $\propto \eta_g^4$ stems from the fact that for the pair creation an absorption of one quantised and two strong field photons is needed. Moreover, from the equation above, it can be seen that the rate for the three-photon process is not zero at the energy threshold. Hence, the outcome firstly found in the lower dimensional theory of QED_{2+1} can be observed in a real physical system of the gapped graphene and is not disturbed by the breakdown of the Lorentz invariance in this framework caused by the Fermi velocity of the quasiparticles. In addition, the behaviour of the rates for the two- (blue solid) and three-photon (red dashed) rates near $|\boldsymbol{p}| = 0$ is depicted in the upper panel of Fig. 6.5 denoted with a). The displayed curves resemble the

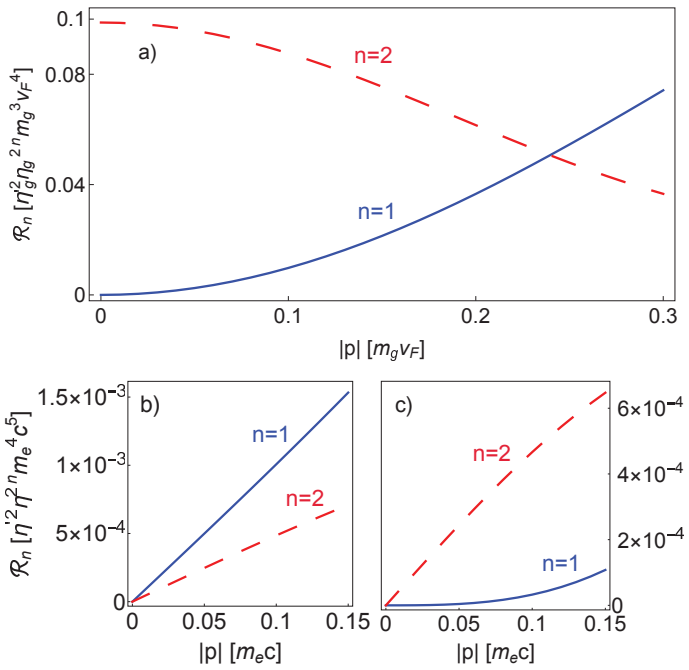

Figure 6.5: Behaviour of the rates in QED (lower panel) and graphene (upper panel) near the energy threshold. Here, the results for an unpolarised γ-photon and a photon polarised parallelly to the strong field are shown in panels b) and c), correspondingly. This figure was originally published in Ref. [121].

behaviour provided in this and the previous subsections: while the blue line starts at zero, the $n = 2$ contribution attains a non-zero value at the threshold.

6.2.3 Comparison to QED and discussion

The fact that the quasiparticle production rate when two strong field photons are absorbed does not vanish for $|\boldsymbol{p}| = 0$ stands in sharp contrast to the QED rates from chapter 3, which are always equal to zero in the corresponding limit[6] (see Eq. (5.33)). Thus, in this subsection, a comparison between the results found in the present chapter and the Breit-Wheeler pair creation in the framework of ordinary QED is discussed. To that end, the rates R_n^g (panel a) in Fig. 6.5) are plotted against their QED analogues, which are depicted in the lower panel of Fig. 6.5. The rates stemming from Eq. (3.15) for the configuration involving an unpolarised photon are shown in the panel b), while the case with a photon polarised parallelly to the polarisation of the strong field from Eq. (3.14) is given in the panel denoted with c).

Putting aside the obvious differences in the threshold behaviour at $|\boldsymbol{p}| = 0$ for $n = 2$, which can be explained by the reduced dimensionality of the phase space of the created quasipairs (see subsection 5.3.1), the course of the curve representing $R_1^g \sim |\boldsymbol{p}|^2$ will be discussed next. As it was anticipated for the QED_{2+1} rate in Eq. (5.30) and reviewed below this equation, following Fig. 6.5 the behaviour of the rate in question rather resembles the trend set by the corresponding $n = 1$ curve in the panel c). This agreement can be explained by the fact that for the process taking place in graphene only the projections of the field polarisations on the graphene surface are relevant (see discussion below Eq. (6.12)). Thus, in the chosen case of the counterpropagating fields, the setup resembles the situation of photons polarised parallelly to each other.

Moreover, an interesting insight for the understanding of the vanishing and non-vanishing threshold rates in graphene for the considered cases is provided by an exposition of the total angular momentum of the system. According to the zero momentum of created quasiparticles at the threshold, they do not carry orbital angular momentum. In addition, the total spin of the quasiparticle-hole pair is also zero as the spin is conserved in the electronic transition from the valence to the conduction band [134]. However, following the structure of the spinors given below Eq. (6.6) and in Eq. (6.14), an excited valence electron changes its pseudospin acquiring, according to Ref. [134], one unit of angular momentum. The latter must be delivered to the system by the participating photons, which is not possible when only two linearly polarised photons take part in the reaction and at the threshold $R_1^g = 0$ must hold. Conversely, one unit of angular momentum can be provided by the three-photon interaction resulting in a threshold behaviour of $R_2^g > 0$. This situation resembles the decay of orthopositronium, a spin-triplet state, which can

[6]The procedure shown in chapter 3 was restricted to the leading order in the fine-structure constant α. When the next orders are taken into account, due to the Coulomb interactions in the final state, the rates in QED attain a tiny non-zero threshold value; see, e.g. Ref. [137].

annihilate only into three photons because a two-photon decay is forbidden.

Lastly, the results provided in this chapter can be verified experimentally when applying moderately intense beams of terahertz radiation [138, 139, 140]. To that end, when assuming a bandgap of $\Delta = 0.1\,\mathrm{eV}$ [126, 127, 128, 129, 130] combined with the frequencies $\omega' = 2\omega \gtrsim 0.1\,\mathrm{eV}$ and intensities $I_0 = 10I_0' = 10^5\,\mathrm{W/cm^2}$ ($\eta_g \approx 0.1$, $\eta_g' \approx 1.6 \times 10^{-2}$), at the threshold the particle rate per area $\mathcal{R}_2^g \approx 10^{10}$ $\mathrm{s^{-1}\mu m^{-2}}$ can be obtained. At this point a remark is in order: The perturbative framework applied in this chapter holds only whenever the field amplitudes lie well below the critical field in graphene $E_c = \Delta^2/|e|v_F$, which translates to the critical intensity of $I_c = cE_{\mathrm{crit}}^2/2 \approx 6 \times 10^7\,\mathrm{W/cm^2}$ for the considered gap. Moreover, a detection of the created quasipairs could follow by measuring the current induced by the excited valence electrons when an external voltage is applied [112].

6.3 Summary

In this chapter the linear and three-photon Breit-Wheeler processes represented by a creation of quasiparticle-hole pairs in gapped graphene monolayers were studied. The results obtained in this way provide a physical realisation of a low dimensional system similar to QED_{2+1} considered in the previous chapter. Here, as the intensity of the photon sources, which are counterpropagating, was chosen in a way that $\eta_g,\ \eta_g' \ll 1$, $\eta_g \gg \eta_g'$ hold, a perturbative treatment in both fields applies. However, coherent implementation of the stronger field allows for better comparison with the pure QED_{2+1} and QED analogues.

While the study of the two-photon process generates a new method for experimental observation of the linear Breit-Wheeler reaction, the discussion on the three-photon interaction verifies peculiar results provided in subsection 5.3.1. Thus, the rate calculated in subsection 6.2.2 featured a nonvanishing contribution at the energy threshold, where the created pair has zero momentum. Despite the fact that this result has been shown explicitly only for a three-photon rate, since it relies on the lower dimensionality of the underlying vacuum state, it is expected to be expandable to the case when the total number of absorbed strong field photons is even (see Eq. (5.33)). Though, the next order processes which would exhibit similar behaviour are much more difficult to detect at low and moderate intensities with $\eta_g,\ \eta_g' \ll 1$.

Chapter 7

Conclusions and outlook

In this thesis the Breit-Wheeler particle creation in various scenarios was discussed. Thus, after a short introduction to the framework of QED at the beginning and consequent review of the pair production in an electromagnetic plane-wave field, a study of the linear process resulting from the interaction of an intense x-ray laser and up to several GeV bremsstrahlung photons was presented in section 4.2. Thus, when using incident bremsstrahlung electron bunches with up to 1 nC of charge, the detection of 80-800 pairs is expected providing a long overdue experimental verification of the linear Breit-Wheeler process from real photons.

When the x-ray laser in this setup is exchanged with an optical one of high intensity, the nonperturbative regime with $\xi \gg 1$ and $\kappa \approx 1$, as proposed in section 4.3, is in reach. The analysis here has been focused on the incorporation of different laser field models, including the constant crossed field, the plane wave and the paraxial Gaussian pulse. In the case of the latter the impact of laser focusing was studied by means of variation of the intensity and the corresponding beam waist, presence of longitudinal focusing or adoption of super-Gaussian time and space envelopes. Thus, it has been shown that the yielded number of pairs strongly depends on both the laser intensity and the interaction volume. Moreover, in this setup an estimated number of up to 10 pairs per hour is expected, which appears to be resolvable with the currently available sophisticated detection technologies. Lastly, both studies presented in chapter 4 may be complemented with the energy and momentum spectra of created particles. This kind of information, which could be provided from the side of theory with help of electron states derived in Refs. [25, 141], would facilitate the experimental detection effort.

In the chapter 5, the Breit-Wheeler pair creation in 2+1 dimensional Minkowski spacetime was investigated. Similarly to the previous case, the discussion involved the weak field perturbative and strong field nonperturbative regimes. For the former, a peculiar behaviour of the rates resulting from the absorption of an even number of strong field photons was found that represents a general consequence of the 2+1 dimensional spacetime. They manifest a non-zero contribution at the energy threshold, where the created particles have zero momentum. Similar even-odd staggerings appear also in strong field processes in ordinary QED such as high-harmonic genera-

tion, where they are related to the total parity of the photons that participate in the reaction: a point that could be an extension of the present study. In the strong field regime, a deviation in the exponent of the quantum nonlinearity parameter when comparing to QED rates was highlighted. This mismatch can potentially lead to different criteria for the applicability of the perturbation theory in 2+1 dimensions. Thus, a corresponding calculation regarding the radiative corrections can be conducted in the future and provide insights on the breakdown of perturbation theory [5].

The low dimensional consideration in vacuum has been extended by a study of the two- and three-photon Breit-Wheeler processes in bandgapped graphene, which were presented in chapter 6. Since the behaviour of the charge carriers in this material resembles the QED_{2+1}-like description, the expected lifting of the three-photon rate at the threshold could be verified. Moreover, the study of the linear Breit-Wheeler process provides an alternative way for observation of this process. Finally, in future work, regardless being tedious as a consequence of elaborate Volkov-like solutions in graphene, the discussion could be extended by the incorporation of the high intensity regime.

Concluding, it is noteworthy to point out that the investigations displayed in the present work are relevant for the experimental efforts undertaken currently. Thus, the discussion on the nonlinear nonperturbative Breit-Wheeler process was performed within the scope of the research unit FOR2783, where a possibility to observe the pair creation in the parameter range $\xi \gg 1$, $\kappa \approx 1$ for the first time is studied experimentally and theoretically [33]. In addition, the Breit-Wheeler consideration in graphene supplements recent studies on the electron manipulation by means of applied electromagnetic fields with the goal of the exploration of the photon driven effects (see e.g. [142] and references therein).

Appendices

Appendix A

Conventions and important relations

A.1 Traces and identities involving $\gamma-$matrices

A.1.1 3+1 dimensions

Firstly, the focus is put on $4 \times 4-$dimensional matrices γ^μ with $\mu = 0, 1, 2, 3$, which are relevant for calculations in 3+1 dimensional QED (as it can be seen from its action in Eq. (2.1)). These satisfy the anticommutation relation $\{\gamma^\mu, \gamma^\nu\} = 2g^{\mu\nu}$ involving a four-dimensional metric tensor $g^{\mu\nu}$ with signature a $\mathrm{diag}(g^{\mu\nu}) = (1, -1, -1, -1)$. Moreover, for trace calculations in chapter 3 the following relations have been used

$$\begin{aligned}
&\gamma^0\gamma^{\dagger\mu}\gamma^0 = \gamma^\mu, \quad \gamma^\mu\gamma_\mu = 4\mathbb{1}_{4\times4}, \quad \mathrm{Tr}[\gamma^\mu\gamma^\nu] = 4g^{\mu\nu}, \quad \gamma^\mu\gamma^\nu\gamma_\mu = -2\gamma^\nu, \\
&\mathrm{Tr}[\gamma^{\mu_1}...\gamma^{\mu_n}] = 0 \text{ for odd } n, \quad \mathrm{Tr}[\gamma^\mu\gamma_\mu] = 16, \\
&\mathrm{Tr}[\gamma^{\mu_1}...\gamma^{\mu_n}] = g^{\mu_1\mu_2}\mathrm{Tr}[\gamma^{\mu_3}...\gamma^{\mu_n}] - g^{\mu_1\mu_3}\mathrm{Tr}[\gamma^{\mu_2}\gamma^{\mu_4}...\gamma^{\mu_n}] + ... + g^{\mu_1\mu_n}\mathrm{Tr}[\gamma^{\mu_2}...\gamma^{\mu_n}], \\
&\gamma^\mu\gamma^\alpha\gamma^\beta\gamma_\mu = 2\gamma^\alpha\gamma^\beta + 2\gamma^\beta\gamma^\alpha, \quad \gamma^\mu\gamma^\nu\gamma^\alpha\gamma^\beta\gamma^\sigma\gamma_\mu = 2\gamma^\sigma\gamma^\nu\gamma^\alpha\gamma^\beta + 2\gamma^\beta\gamma^\alpha\gamma^\nu\gamma^\sigma.
\end{aligned} \tag{A.1}$$

A.1.2 2+1 dimensions

In contrast to QED, in QED_{2+1} the Dirac matrices γ^μ, $\mu = 0, 1, 2$, are $2 \times 2-$ dimensional satisfying the anticommutation relation $\{\gamma^\mu, \gamma^\nu\} = 2g^{\mu\nu}$, where $g^{\mu\nu}$ is a metric tensor with signature $\mathrm{diag}(g^{\mu\nu}) = (1, -1, -1)$. Here, the particularization $\gamma^\mu = (\sigma_3, i\sigma_2, -i\sigma_1)$ with the Pauli matrices

$$\sigma_1 = \begin{pmatrix} 0 & 1 \\ 1 & 0 \end{pmatrix}, \quad \sigma_2 = \begin{pmatrix} 0 & -i \\ i & 0 \end{pmatrix}, \quad \sigma_3 = \begin{pmatrix} 1 & 0 \\ 0 & -1 \end{pmatrix} \tag{A.2}$$

is made. Moreover, in 2+1 dimensions the gamma matrices satisfy the following relations [99]

$$\gamma^0\gamma^{\dagger\mu}\gamma^0 = \gamma^\mu, \quad \gamma^\mu\gamma_\mu = 3\mathbb{1}_{2\times2}, \quad \mathrm{Tr}[\gamma^\mu\gamma^\nu] = 2g^{\mu\nu}, \quad \mathrm{Tr}[\gamma^\mu\gamma_\mu] = 6, \quad \gamma^\mu\gamma^\nu\gamma_\mu = -\gamma^\nu,$$
$$\mathrm{Tr}[\gamma^\nu] = 0, \quad \mathrm{Tr}[\gamma^\mu\gamma^\nu\gamma^\alpha] = -2i\epsilon^{\mu\nu\alpha}, \quad \gamma^\mu\gamma^\nu\gamma^\alpha\gamma_\mu = 4g^{\nu\alpha} - \gamma^\nu\gamma^\alpha,$$
$$\gamma^\mu\gamma^\nu\gamma^\alpha\gamma^\beta\gamma_\mu = \gamma^\nu\gamma^\alpha\gamma^\beta - 2\gamma^\beta\gamma^\alpha\gamma^\nu, \quad \mathrm{Tr}[\gamma^\mu\gamma^\nu\gamma^\alpha\gamma^\beta] = 2(g^{\mu\nu}g^{\alpha\beta} - g^{\mu\alpha}g^{\nu\beta} + g^{\mu\beta}g^{\nu\alpha}) \tag{A.3}$$

with the Levi-Civita tensor $\epsilon^{\mu\nu\alpha}$ and $\epsilon^{012} = 1$.

A.2 Spinors

A.2.1 3+1 dimensions

The free Dirac equation provided in Eq. (2.14) is solved by employing a plane-wave ansatz $\psi_p(x) = Nu_{p,s}\mathrm{e}^{-ipx}$ with a spinor $u_{p,s}$ satisfying $(\not{p} - m)u_{p,s} = 0$. Thus, a positive-energy solution representing an electron can be found. Analogously, a negative-energy approach $\psi_p(x) = Nv_{p,s}\mathrm{e}^{ipx}$ with $(\not{p} + m)v_p = 0$ leads to a positron solution. Hence, one obtains four-dimensional vectors [34]

$$u_{p_-,s} = N_{p_-}\begin{pmatrix} \chi_s \\ \frac{\boldsymbol{\sigma p}_-}{m+p_0^-}\chi_s \end{pmatrix}, \; v_{p_+,s} = N_{p_+}\begin{pmatrix} \frac{\boldsymbol{\sigma p}_+}{m+p_0^+}\chi'_s \\ \chi'_s \end{pmatrix} \tag{A.4}$$

containing normalisation constants $N_{p_\pm} = \sqrt{\frac{m+p_0^\pm}{2m}}$ and elementary two-dimensional spinor vectors $\chi_1^T = \chi_1'^T = (1,0)$, $\chi_2^T = \chi_2'^T = (0,1)$, which represent the spin degree of freedom, as well as $\boldsymbol{\sigma} = (\sigma_1, \sigma_2, \sigma_3)$ with the Pauli matrices σ_i, $i = 1,2,3$ from Eq. (A.2).

Moreover, the spinors $u_{p_-,s}$ and $v_{p_+,s}$ are normalised in accordance with the following relations:

$$\sum_{s=1}^{2} u_{p_-,s}\bar{u}_{p_-,s} = \frac{\not{p}_- + m}{2m}, \quad \sum_{s=1}^{2} v_{p_+,s}\bar{v}_{p_+,s} = \frac{\not{p}_+ - m}{2m} \tag{A.5}$$

and $\bar{u}_{p_-,s}\gamma^\mu u_{p_-,s} = \frac{p_-^\mu}{m}$ for $\bar{u}_{p_-,s} \equiv u_{p_-,s}^\dagger\gamma^0$, $\bar{v}_{p_+,s} \equiv v_{p_+,s}^\dagger\gamma^0$.

A.2.2 2+1 dimensions

In order to solve the free Dirac equation given in Eq. (5.6) by a plane-wave ansatz, a solution of the equation $(\not{p}_- - m)u_{p_-} = 0$ for the electron spinor and $(\not{p}_+ + m)v_{p_+} = 0$ for the positron spinor has to be found, which in this case are represented by two-

dimensional vectors and result to

$$u_{p_-} = N_{p_-} \begin{pmatrix} 1 \\ \frac{p_-^1 + ip_-^2}{m+p_0^-} \end{pmatrix}, \; v_{p_+} = N_{p_+} \begin{pmatrix} \frac{p_+^1 - ip_+^2}{m+p_0^+} \\ 1 \end{pmatrix} \tag{A.6}$$

with the normalisation constant $N_{p_\pm} = \sqrt{\frac{m+p_0^\pm}{2m}}$. Note that in QED_{2+1} the states do not have the spin degree of freedom. Further, the spinors u_{p_-} and v_{p_+} are normalised in accordance with the following relations:

$$u_{p_-}\bar{u}_{p_-} = \frac{\not{p}_- + m}{2m}, \quad v_{p_+}\bar{v}_{p_+} = \frac{\not{p}_+ - m}{2m}, \tag{A.7}$$

where, when compared to Eq. (A.5) no summation over the spin is needed, and $\bar{u}_{p_-}\gamma^\mu u_{p_-} = \frac{p_-^\mu}{m}$ for $\bar{u}_{p_-} \equiv u_{p_-}^\dagger \gamma^0$, $\bar{v}_{p_+} \equiv v_{p_+}^\dagger \gamma^0$.

Appendix B

Properties of generalised Bessel functions

A generalised Bessel function [2, 50, 143] is defined as an infinite sum of products of ordinary Bessel functions of one argument $J_i(x)$ [52]

$$\tilde{J}_n(z_-, z_+) = \sum_{m=-\infty}^{\infty} J_{n-2m}(z_-) J_m(z_+). \tag{B.1}$$

When one of its arguments is zero, the latter can be written as [50, 143]

$$\tilde{J}_n(0, z_+) = \begin{cases} J_{n/2}(z_+), & n \text{ even}, \\ 0, & n \text{ odd} \end{cases} \text{ and } \tilde{J}_n(z_-, 0) = J_n(z_-). \tag{B.2}$$

Moreover, the following relations hold:

$$\tilde{J}_n(-z_-, z_+) = (-1)^n \tilde{J}_n(z_-, z_+), \quad \tilde{J}_n(z_-, -z_+) = (-1)^n \tilde{J}_{-n}(z_-, z_+) \tag{B.3}$$

and

$$\tilde{J}_{-n}(z_-, z_+) = (-1)^n \tilde{J}_n(z_-, -z_+). \tag{B.4}$$

In order to evaluate the integrals in chapters 3 and 5, a Fourier expansion of the generalised Bessel function is introduced

$$\mathrm{e}^{-iz_-\sin(kx) - iz_+\sin(2kx)} = \sum_{n=-\infty}^{\infty} \mathrm{e}^{-inkx} \tilde{J}_n(z_-, z_+) \tag{B.5}$$

and when Euler's representation is incorporated, terms proportional to $\cos^l(kx)$ with $l = 1, 2$ can be written as

$$\begin{aligned}
&\cos^l(kx)\mathrm{e}^{-iz_-\sin(kx)-iz_+\sin(2kx)} = \sum_{n=-\infty}^{\infty} \mathrm{e}^{-inkx}\tilde{\mathcal{J}}_n^l, \\
&\tilde{\mathcal{J}}_n^1 \equiv \frac{1}{2}\left[\tilde{J}_{n+1}(z_-,z_+) + \tilde{J}_{n-1}(z_-,z_+)\right], \\
&\tilde{\mathcal{J}}_n^2 \equiv \frac{1}{4}\left[\tilde{J}_{n+2}(z_-,z_+) + 2\tilde{J}_n(z_-,z_+) + \tilde{J}_{n-2}(z_-,z_+)\right].
\end{aligned} \tag{B.6}$$

B.1 Small argument behaviour

Depending on its arguments, generalised Bessel functions show different asymptotic behaviour. As the arguments considered in the present thesis are proportional to the laser intensity parameter ξ: $z_- = \xi\beta, z_+ = \xi^2\varrho$ with $\beta = -m(\frac{q^+\epsilon}{q^+k} - \frac{q^-\epsilon}{q^-k})$, $\rho = -\frac{m^2}{8}\frac{kk'}{kq^+kq^-}$, the field strength will be the governing parameter for the function's behaviour. Following appendix C in [50], for small arguments, i.e. $\xi \ll 1$, the generalised Bessel functions can be represented as a sum:

$$\tilde{J}_n(\xi\beta,\xi^2\varrho) \approx \left(\frac{\xi^2\varrho}{2}\right)^{\frac{n}{2}} \times \begin{cases} \sum_{k=0}^{n/2} \frac{(\beta^2/2\varrho)^k}{(2k)!(n/2-k)!} & \text{for even } n, \\ \sum_{k=0}^{(n-1)/2} \frac{(\beta^2/2\varrho)^{k+1/2}}{(2k+1)!((n-1)/2-k)!} & \text{for odd } n. \end{cases} \tag{B.7}$$

For the study presented in subsection 3.1.1 the small ξ limit of contributions including Bessel functions with $n = 1$ and $n = 2$ are of interest. Thus, the relevant terms read

$$\tilde{J}_{n=1}^2(z_-,z_+) \approx \frac{\xi^2\beta^2}{4}, \qquad (\tilde{\mathcal{J}}_{n=1}^1)^2 - \tilde{J}_{n=1}(z_-,z_+)\tilde{\mathcal{J}}_{n=1}^2 \approx \frac{1}{4}, \tag{B.8}$$

$$\tilde{J}_{n=2}^2(z_-,z_+) \approx \left(\frac{\xi^2\beta^2}{8} + \frac{\xi^2\rho}{2}\right)^2 \text{ and } \quad (\tilde{\mathcal{J}}_{n=2}^1)^2 - \tilde{J}_{n=2}(z_-,z_+)\tilde{\mathcal{J}}_{n=2}^2 \approx \frac{\xi^2\beta^2}{32} - \frac{\xi^2\rho}{8}. \tag{B.9}$$

B.2 Large argument behaviour

Next, large-argument asymptotes for generalised Bessel functions $\tilde{J}_n(z_-,z_+)$ and the combination $(\tilde{\mathcal{J}}_n^1)^2 - \tilde{J}_n(z_-,z_+)\tilde{\mathcal{J}}_n^2$ are provided, as they are needed for evaluation of the squared matrix elements throughout this thesis. The procedure will be shown following the lines of appendix B in Ref. [2].

Since the considered limit implies $\xi \gg 1$, it is convenient to bring the generalised Bessel functions in a suitable form, where this property can be exploited. To that

end, one uses their integral representation

$$\tilde{J}_n(z_-, z_+) = \frac{1}{\pi}\mathrm{Re}\left[\int_0^\pi d\theta \mathrm{e}^{f(\theta)}\right] \text{ with}$$
$$f(\theta) = -iz_-\sin(\theta) - iz_+\sin(2\theta) + in\theta \tag{B.10}$$

and performs the integration asymptotically via the method of steepest descent [144].

This is done by promotion of θ to a complex variable $\theta = x + iy$ and transformation of the integration in Eq. (B.10) into an integral over a contour C going through the saddle point θ_0 for which a condition $f'(\theta_0) = 0$ holds (see Fig. B.1). Moreover, at the edges of the contour $\mathrm{Re}\,[f(\theta)] \to -\infty$ must apply in order to avoid divergence. Next, $f(\theta)$ is expanded around θ_0.

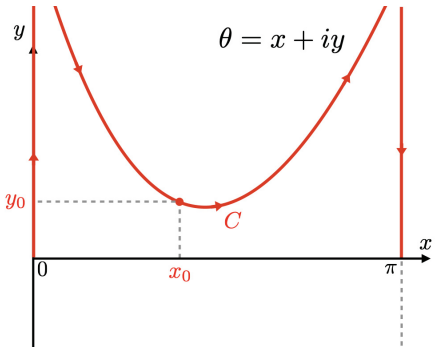

Figure B.1: Analytically continued contour of integration C (red line).

Even though this problem has been treated thoroughly by various authors [2, 3, 4, 50, 145, 146], the majority of them has restricted the analysis to an expansion up to the second order of the function $f(\theta)$, which turns out to be a good approximation when describing the limit of small κ. However, here, the focus lies on deriving asymptotic formulas for both $\kappa \ll 1$ and $\kappa \gg 1$ and, therefore, an expansion of $f(\theta)$ up to the third order term is needed [2, 147]

$$\tilde{J}_n(z_-, z_+) \approx \frac{1}{\pi}\mathrm{Re}\left[\int_C d\theta \mathrm{e}^{f(\theta_0)+\frac{1}{2!}f''(\theta_0)(\theta-\theta_0)^2+\frac{1}{3!}f'''(\theta_0)(\theta-\theta_0)^3}\right]. \tag{B.11}$$

As it will be shown below, next order terms in the expansion will not provide significant contributions. Once this step has been carried out, the saddle point condition ($f'(\theta_0) = 0$) is studied in more detail, which gives rise to a quadratic equation in $\cos(\theta_0)$:

$$\cos^2(\theta_0) + \frac{z_-}{4z_+}\cos(\theta_0) - \frac{n}{4z_+} - \frac{1}{2} = 0 \tag{B.12}$$

the solution of which can be expressed as

$$\cos(x_0)\cosh(y_0) - i\sin(x_0)\sinh(y_0) = \cos(\theta_0) = -\frac{z_-}{8z_+} \pm \frac{i}{\xi}\sqrt{\sigma} \tag{B.13}$$

with $\sigma = -\xi^2\left(\frac{z_-^2}{64z_+^2} + \frac{1}{2} + \frac{n}{4z_+}\right)$. In Sec. 3.1.2 it is shown that for the Breit-Wheeler process at high intensities $\sigma \geq 1$ holds. Additionally, in QED_{2+1} once Eqs. (5.4), (5.45) and the energy-momentum balance are used, one arrives at $\sigma = 1$. To guarantee the convergence of the analytically continued integral in Eq. (B.11) we choose the saddle point with $y > 0$, which implies that $\sinh(y_0) \propto \sqrt{\sigma}/\xi$ for $x_0 \in [0, \pi]$ (see

Fig. B.1). This translates into the following behaviour

$$\begin{aligned}\cos(x_0)\cosh(y_0) &\overset{\xi\gg1}{\approx} \cos(x_0) = -\frac{z_-}{8z_+},\ \sin(x_0)\sinh(y_0) = \frac{\sqrt{\sigma}}{\xi},\\ 1+2\cos^2(x_0)+2\sinh^2(y_0) &\overset{\xi\gg1}{\approx} 1+2\cos^2(x_0) = -\frac{n}{2z_+}\end{aligned} \tag{B.14}$$

and $y_0 \propto \mathcal{O}(1/\xi)$, $x_0 \propto \mathcal{O}(1)$. Consequently, having the relations above in mind, one finds for $\xi \gg 1$

$$\mathrm{Re}[f(\theta_0)] \approx -y_0^3\frac{4n\sin^2(x_0)}{3(1+2\cos^2(x_0))},\ \zeta \equiv \mathrm{Im}[f(\theta_0)] \approx n\left[x_0 - \frac{3\sin(x_0)\cos(x_0)}{1+2\cos^2(x_0)}\right], \tag{B.15}$$

$$f''(\theta_0) \approx -y_0\frac{4n\sin^2(x_0)}{1+2\cos^2(x_0)},\ f'''(\theta_0) \approx i\frac{4n\sin^2(x_0)}{1+2\cos^2(x_0)} = \frac{4n\sin^2(x_0)}{1+2\cos^2(x_0)}\mathrm{e}^{i\delta} \tag{B.16}$$

with $\delta = \pi/2$. For $\xi \gg 1$ the number of absorbed photons approximates $n \geq n_0 \approx \xi^3/\kappa \propto \xi^3$ for fixed κ. Observe that this condition implies that $\xi \gg \kappa^{1/3}$. Hence, the expressions above behave effectively as $\mathrm{Re}[f(\theta_0)] \propto \text{const}$, $\zeta \propto \xi^3$, $f''(\theta_0) \propto \xi^2$ and $f'''(\theta_0) \propto \xi^3$ providing an estimation for the effective integration region $(\theta - \theta_0) \sim 1/\xi$. It can be shown that all higher derivatives $f^{(n)}(\theta)$ evaluated at θ_0 will grow as ξ^3. Therefore, all products of the form $f^{(n)}(\theta_0)(\theta-\theta_0)^n \sim 1/\xi^{n-3}$ will be suppressed as compared to the first three terms in the expansion. With all these details to our disposal, the contour integration is performed by an appropriated modification of the integration path.

Firstly, following Eq. (B.10) the only non-zero contribution to the integral is provided by the middle part of C, which is denoted as $\tilde{C}$, since the shares of its vertical parts are imaginary and do not change the outcome. The complex plane of integration is depicted in Fig. B.2. Moreover, as there are no poles, the Cauchy integration theorem applies and $\tilde{C}$ can be replaced by a curve L (green solid) as long as at the edges of both the condition $\mathrm{Re}[f(\theta)] \to -\infty$ is valid and the connecting pieces (green dotted), therefore, do not contribute. When approximating $f(\theta)$ by its expansion up to the third derivative, the latter condition holds whenever $\mathrm{Re}[f'''(\theta)(\theta-\theta_0)^3] < 0$ [blue areas in Fig. B.2] as according to Eqs. (B.15) and (B.16) the third derivative $f'''(\theta_0)$ is the fastest growing function in ξ. Similarly, the contour L can be replaced by a straight line L' that extends to $\pm\infty$ and is parallel to the boundaries of the blue sectors. Now, a substitution $u = re^{i\varepsilon} = \theta - \theta_0 + \frac{f''(\theta_0)}{f'''(\theta_0)}$

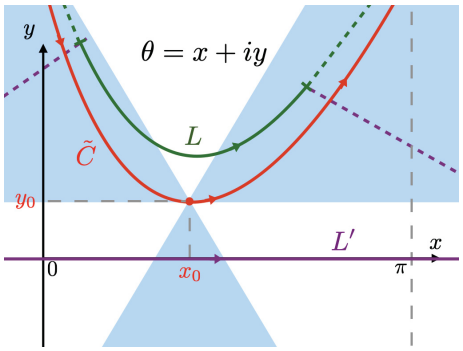

Figure B.2: Contour of integration (red line).

is made resulting into

$$I_0 = \int_{\tilde{C}} d\theta \mathrm{e}^{f(\theta_0)+\frac{(\theta-\theta_0)^2}{2!}f''(\theta_0)+\frac{(\theta-\theta_0)^3}{3!}f'''(\theta_0)} = \mathrm{e}^{f(\theta_0)+\frac{f''^3(\theta_0)}{3f'''^2(\theta_0)}} \int_{L'} du\ \mathrm{e}^{\frac{f'''(\theta_0)}{6}u^3-\frac{f''^2(\theta_0)}{2f'''(\theta_0)}u} \tag{B.17}$$

with L' chosen to go through the point $u = 0$. Hence, for the direction of integration as shown in Fig. B.2 along L' from $-\infty$ to ∞ the condition $\varepsilon = 0$ holds and one obtains

$$I_0 = \mathrm{e}^{f(\theta_0)+\frac{f''^3(\theta_0)}{f'''^2(\theta_0)}} \int_{-\infty}^{\infty} dr\ \exp\left(i\frac{|f'''(\theta_0)|}{6}r^3 - \frac{f''^2(\theta_0)}{2f'''(\theta_0)}r\right). \tag{B.18}$$

After substitution $t = \left(\frac{|f'''(\theta_0)|}{2}\right)^{1/3} r$ and $z = i\frac{f''^2(\theta_0)}{2f'''(\theta_0)}\left(\frac{2}{|f'''(\theta_0)|}\right)^{1/3}$ while making use of the symmetry properties of the Euler form of the exponential function the integral above reads

$$I_0 = 2\mathrm{e}^{f(\theta_0)+\frac{f''^3(\theta_0)}{f'''^2(\theta_0)}} \left(\frac{2}{|f'''(\theta_0)|}\right)^{1/3} \int_0^{\infty} dt\ \cos\left(\frac{t^3}{3}+zt\right) \tag{B.19}$$

and with help of the integral representation of the Airy function $\Phi(y) = \frac{1}{\sqrt{\pi}}\int_0^{\infty}\cos(t^3/3+yt)dt$ one ends up with

$$\begin{aligned} I_0 &= \int_C d\theta \mathrm{e}^{f(\theta)} \approx \int_C d\theta \mathrm{e}^{f(\theta_0)+\frac{(\theta-\theta_0)^2}{2!}f''(\theta_0)+\frac{(\theta-\theta_0)^3}{3!}f'''(\theta_0)} \\ &\approx 2\sqrt{\pi}\left(\frac{2}{|f'''(\theta_0)|}\right)^{1/3}\Phi(z)\mathrm{e}^{f(\theta_0)+\frac{f''^3(\theta_0)}{3f'''^2(\theta_0)}} = 2\sqrt{\pi}\left(\frac{2}{|f'''(\theta_0)|}\right)^{1/3}\Phi(z)\mathrm{e}^{i\zeta}, \end{aligned} \tag{B.20}$$

where $z \approx y_0^2\left(\frac{|f'''(\theta_0)|}{2}\right)^{2/3}$ [2, 3]. The last approximation occurs because $\mathrm{Re}[f(\theta_0)] + \frac{f''^3(\theta_0)}{3f'''^2(\theta_0)} = 0$ holds (see Eqs. (B.15) and (B.16)). Correspondingly, when exploiting Eq. (B.10) we obtain

$$\tilde{J}_n(z_-, z_+) \approx \frac{1}{\pi}\mathrm{Re}[I_0] = \frac{2}{\sqrt{\pi}}\left(\frac{2}{|f'''(\theta_0)|}\right)^{1/3}\Phi(z)\cos(\zeta). \tag{B.21}$$

Next, we proceed to the calculation of $(\tilde{\mathcal{J}}_n^1)^2 - \tilde{J}_n(z_-, z_+)\tilde{\mathcal{J}}_n^2$. Similarly to Eq. (B.10), it can be written as

$$\begin{aligned} (\tilde{\mathcal{J}}_n^1)^2 - \tilde{J}_n(z_-, z_+)\tilde{\mathcal{J}}_n^2 = \frac{1}{\pi^2}\Bigg(&\mathrm{Re}\left[\int_0^{\pi} d\theta\cos(\theta)\mathrm{e}^{f(\theta)}\right]^2 \\ &-\mathrm{Re}\left[\int_0^{\pi} d\theta\mathrm{e}^{f(\theta)}\right]\mathrm{Re}\left[\int_0^{\pi} d\theta\cos^2(\theta)\mathrm{e}^{f(\theta)}\right]\Bigg), \end{aligned} \tag{B.22}$$

which is further expanded in $\cos(\theta) \approx \cos(\theta_0) - \sin(\theta_0)(\theta-\theta_0) + 1/2\cos(\theta_0)(\theta-\theta_0)^2$

around the saddle point θ_0. When defining

$$I_1 = \int_C d\theta(\theta-\theta_0)\mathrm{e}^{f(\theta)},\ I_2 = \int_C d\theta(\theta-\theta_0)^2\mathrm{e}^{f(\theta)} \tag{B.23}$$

one obtains up to I_0^2/ξ^3 order

$$\begin{aligned}\pi^2\left((\tilde{\mathcal{J}}_n^1)^2 - \tilde{J}_n(z_-,z_+)\tilde{\mathcal{J}}_n^2\right) &\approx \mathrm{Re}\left[\sin(\theta_0)\right]^2\left[\mathrm{Re}[I_1]^2 - \mathrm{Re}[I_0]\mathrm{Re}[I_2]\right]\\ &+ \mathrm{Im}[\cos(\theta_0)]^2|I_0|^2 + 2\mathrm{Re}[\sin(\theta_0)]\mathrm{Im}[\cos(\theta_0)]\left(\mathrm{Re}[I_1]\mathrm{Im}[I_0] - \mathrm{Re}[I_0]\mathrm{Im}[I_1]\right).\end{aligned} \tag{B.24}$$

Whereas the asymptotic expression for I_2 results from Eq. (B.20) when taking a derivative with respect to $f''(\theta_0)$ of the last contribution in the first line and the first term of the second line, the asymptote for I_1 can be read off from a relation $2f''(\theta_0)I_1 \approx -f'''(\theta_0)I_2$

$$I_1 \approx -\frac{4\sqrt{\pi}f'''(\theta_0)}{f''^2(\theta_0)}\left(\frac{2}{|f'''(\theta_0)|}\right)^{1/3}\mathrm{e}^{i\zeta}\left[z^{3/2}\Phi(z) + z\Phi'(z)\right], \tag{B.25}$$

$$I_2 \approx \frac{8\sqrt{\pi}}{f''^2(\theta_0)}\left(\frac{2}{|f'''(\theta_0)|}\right)^{1/3}\mathrm{e}^{i\zeta}\left[z^{3/2}\Phi(z) + z\Phi'(z)\right]. \tag{B.26}$$

Combining outcomes from Eqs. (B.21), (B.24),(B.25) and (B.26) one ends up with

$$\begin{aligned}\tilde{J}_n^2(z_-,z_+) &\approx \frac{2}{\pi}\left(\frac{2}{|f'''(\theta_0)|}\right)^{2/3}\Phi^2(z)\left(1+\cos(2\zeta)\right),\\ (\tilde{\mathcal{J}}_n^1)^2 - \tilde{J}_n(z_-,z_+)\tilde{\mathcal{J}}_n^2 &\approx \frac{2}{\pi\xi^2}\left(\frac{2}{|f'''(\theta_0)|}\right)^{2/3}\\ &\quad\times\left[\Phi^2(z) + \frac{\Phi'^2(z)}{z} + \cos\left(2\zeta\right)\left(\Phi^2(z) - \frac{\Phi'^2(z)}{z}\right)\right].\end{aligned} \tag{B.27}$$

Notice that the contributions to the rate coming from terms which are proportional to $\cos(2\zeta)$ can be neglected. They are highly oscillating since a large number of photons is needed for the process to take place and the argument of the $\cos(2\zeta)$ is proportional to n (see Eq. (B.15)). Hence, the asymptotic expressions for large arguments behaviour of generalised Bessel functions read

$$\begin{aligned}\tilde{J}_n^2(z_-,z_+) &\approx \frac{2}{\pi}\left(\frac{2}{|f'''(\theta_0)|}\right)^{2/3}\Phi^2(z),\\ (\tilde{\mathcal{J}}_n^1)^2 - \tilde{J}_n(z_-,z_+)\tilde{\mathcal{J}}_n^2 &\approx \frac{2}{\pi\xi^2}\left(\frac{2}{|f'''(\theta_0)|}\right)^{2/3}\left[\Phi^2(z) + \frac{\Phi'^2(z)}{z}\right].\end{aligned} \tag{B.28}$$

Finally, by making use of Eqs. (B.14)-(B.16) one finds

$$\left(\frac{2}{|f'''(\theta_0)|}\right)^{2/3} \approx \frac{1}{\xi^2 \sin^2(x_0)}\frac{\sigma}{z},\ y_0 \approx \frac{\sqrt{\sigma}}{\xi \sin(x_0)},\ z = \left(-\frac{4z_+}{\xi^3 \sin(x_0)}\right)^{2/3}\sigma \tag{B.29}$$

and

$$\begin{aligned} &\tilde{J}_n^2(z_-, z_+) \approx \frac{2\sigma}{\pi\xi^2 z \sin^2(x_0)}\Phi^2(z), \\ &(\tilde{\mathcal{J}}_n^1)^2 - \tilde{J}_n(z_-, z_+)\tilde{\mathcal{J}}_n^2 \approx \frac{2\sigma^2}{\pi\xi^4 z \sin^2(x_0)}\left[\Phi^2(z) + \frac{\Phi'^2(z)}{z}\right]. \end{aligned} \tag{B.30}$$

Appendix C

Laser field profiles

This appendix draws on sections dedicated to the laser pulse profiles in Refs. [51, 60].

C.1 Fourier transformed of a Gaussian pulse's vector potential

In the Lorentz gauge with $\varphi = 0$, the electric field relates to the vector potential $\mathcal{A}^\mu = (\varphi, \boldsymbol{\epsilon}\mathfrak{a})$ via an expression $\boldsymbol{\mathcal{E}} = -\boldsymbol{\epsilon}\frac{\partial \mathfrak{a}}{\partial t}$. Thus, the Fourier transformed of the vector potential amplitude can be written as

$$\tilde{\mathfrak{a}}(\tilde{k}, k) = -\int d^4x \mathrm{e}^{i\tilde{k}x} \int^t dt' \mathcal{E}((t', \boldsymbol{x}), k). \tag{C.1}$$

Next, the Fourier transformed of the vector potential corresponding to the field in Eq. (4.1) with $\Phi_0 = \pi/2$ is calculated following the equation above as it is required for the calculations presented in subsection 4.2.2. To that end, firstly, the integrations over the spatial components d^3x are performed while writing the $\cos(\Phi)$ in the Euler representation and using

$$\int_{-\infty}^{\infty} du\ \mathrm{e}^{-au^2+ibu} = \sqrt{\frac{\pi}{a}}\mathrm{e}^{-\frac{b^2}{4a}}, \quad \mathrm{e}^{i\arctan(\zeta)} = \frac{\sqrt{1+\zeta^2}}{1+i\zeta}, \tag{C.2}$$

which results in

$$\tilde{\mathcal{E}}((t', \tilde{\boldsymbol{k}}), k) = \int d^3x \mathrm{e}^{-i\tilde{\boldsymbol{k}}\boldsymbol{x}} \mathcal{E}((t', \boldsymbol{x}), k) = \frac{\pi\sqrt{\pi} w_0^2 \mathcal{E}_0}{2} \frac{\tau}{\sqrt{2\ln(2)}} \mathrm{e}^{-\frac{\tilde{k}_\perp^2 w_0^2}{4}}$$
$$\times \left[\mathrm{e}^{-\frac{(\tau/\sqrt{2\ln(2)})^2}{4}(-\tilde{k}_z+\omega-\frac{\tilde{k}_\perp^2 w_0^2}{4z_R})^2} \mathrm{e}^{-it(\tilde{k}_z+\frac{\tilde{k}_\perp^2 w_0^2}{4z_R})} + \mathrm{e}^{-\frac{(\tau/\sqrt{2\ln(2)})^2}{4}(-\tilde{k}_z-\omega+\frac{\tilde{k}_\perp^2 w_0^2}{4z_R})^2} \mathrm{e}^{-it(\tilde{k}_z-\frac{\tilde{k}_\perp^2 w_0^2}{4z_R})} \right]. \tag{C.3}$$

Further, the integrals over t' and t are carried out and one obtains

$$\tilde{a}_0(\tilde{k},k) = -\frac{i\pi^2\sqrt{\pi}w_0^2\mathcal{E}_0}{\tilde{k}_0}\frac{\tau}{\sqrt{2\ln(2)}}\mathrm{e}^{-\frac{\tilde{k}_\perp^2 w_0^2}{4}} \times\left[\mathrm{e}^{-\frac{(\tau/\sqrt{2\ln(2)})^2}{4}(\omega-\tilde{k}_0)^2}\delta\left(\tilde{k}_z-\tilde{k}_0+K\right)+\mathrm{e}^{-\frac{(\tau/\sqrt{2\ln(2)})^2}{4}(\omega+\tilde{k}_0)^2}\delta\left(\tilde{k}_z-\tilde{k}_0-K\right)\right] \tag{C.4}$$

with $K=\frac{\tilde{k}_\perp^2 w_0^2}{4z_R}$.

For long pulses, i.e. $\omega\tau\gg 1$, the biggest contribution in the exponential functions is provided by $\tilde{k}_0\approx\pm\omega$. Thus, when inserting the definition of z_R, the expression above approximates

$$\tilde{a}_0(\tilde{k},k) = -\frac{i\pi\sqrt{\pi}w_0^2\mathcal{E}_0}{\tilde{k}_0}\frac{\tau}{\sqrt{2\ln(2)}}\mathrm{e}^{-\frac{\tilde{k}_\perp^2 w_0^2}{4}}\delta\left(\tilde{k}_z-\tilde{k}_0+\frac{\tilde{k}_\perp^2}{2\tilde{k}_0}\right) \times\left[\mathrm{e}^{-\frac{(\tau/\sqrt{2\ln(2)})^2}{4}(\omega-\tilde{k}_0)^2}+\mathrm{e}^{-\frac{(\tau/\sqrt{2\ln(2)})^2}{4}(\omega+\tilde{k}_0)^2}\right], \tag{C.5}$$

which coincides with the corresponding result found in [148] for $\tilde{k}_\perp\ll\tilde{k}_0$.

C.2 Energy of the Gaussian pulse

The beam energy carried by the Gaussian pulse can be calculated from the associated beam power, which is obtained by integrating the $z-$component of the absolute value of the Poynting vector over the transverse area $d^2r=dxdy$ through the focus

$$P(t,z) = \frac{\mathcal{E}_0^2}{2}\frac{\pi w_0^2}{2}\mathrm{e}^{-2\left(\sqrt{2\ln(2)}\frac{\varphi}{\omega\tau}\right)^2} \times\left\{1-\frac{1}{1+\zeta(z)^2}\left[\cos\left(2\left(\Phi_0+\varphi\right)\right)-\zeta(z)\sin\left(2\left(\Phi_0+\varphi\right)\right)\right]\right\} \tag{C.6}$$

with $\varphi=\omega(t-z)$. Once the equation above is integrated over time, one obtains the pulse energy

$$W_\mathrm{G}\approx\frac{\mathcal{E}_0^2}{2}\frac{\pi w_0^2}{2}\frac{\tau}{2}\sqrt{\frac{\pi}{\ln(2)}} \tag{C.7}$$

with the accuracy up to a term decreasing exponentially in $(\omega\tau)^2$ for $\omega\tau\gg 1$. Since it does not influence the pulse energy, $\Phi_0=0$ was set.

In order to identify an effective interaction area A_int and an effective interaction time T_int associated with a paraxial Gaussian pulse, its energy is compared to the ones resulting from the laser field modelled as a plane-wave Gaussian pulse and monochromatic plane wave. The field associated with the pulsed scenario can be

read off from Eq. (4.1) when the limit $w_0 \to \infty$ is taken. Explicitly it reads

$$\mathcal{E}_x(\varphi) = \mathcal{E}_0 \mathrm{e}^{-\left(\sqrt{2\ln(2)}\frac{\varphi}{\omega\tau}\right)^2} \sin(\varphi) := \mathcal{E}_0 \psi(\varphi). \tag{C.8}$$

As the expression above does not depend on transversal coordinates, its beam power would formally diverge. Therefore, the infinite area is parametrised as A_{int} leading to $P(\varphi) = \mathcal{E}_x^2(\varphi) A_{\mathrm{int}}$ and the corresponding beam energy

$$W_{\mathrm{pw}} \approx \frac{\mathcal{E}_0^2}{2} A_{\mathrm{int}} \frac{\tau}{2} \sqrt{\frac{\pi}{\ln(2)}}. \tag{C.9}$$

When keeping the energy of both configurations constant, one can identify the effective interacting area $A_{\mathrm{int}} = \pi w_0^2/2$. Implicitly, this means that the plane-wave field is truncated transversally, i.e. $\mathcal{E}_x(\varphi) \to \mathcal{E}_x(\varphi)\Theta(r)\Theta(w_0/\sqrt{2} - r)$ with the unit step function $\Theta(x)$.

For $\omega\tau \to \infty$ the plane wave in Eq. (C.8) goes over to a monochromatic limit with a power $P(\varphi) = \mathcal{E}_0^2 \sin^2(\varphi) A_{\mathrm{int}}$. In this context, the beam energy equals $W_{\mathrm{mpw}} = \langle P \rangle T_{\mathrm{int}}$, where

$$\langle P \rangle = \lim_{T_{\mathrm{int}} \to \infty} \frac{1}{T_{\mathrm{int}}} \int_{-\frac{1}{2}T_{\mathrm{int}}}^{\frac{1}{2}T_{\mathrm{int}}} P(\varphi) dt = I A_{\mathrm{int}} \tag{C.10}$$

is its mean power with $I = \mathcal{E}_0^2/2$ referring to the time-averaged intensity. When comparing the expression above with Eqs. (C.9) and (C.10) the effective interaction time equals $T_{\mathrm{int}} = \frac{\tau}{2}\sqrt{\frac{\pi}{\ln(2)}}$.

C.3 Gaussian pulse beyond paraxial approximation

The electric and magnetic fields of a strong Gaussian pulse are modified by higher order contributions in the diffraction angle $\epsilon = w_0/z_R$. According to Ref. [61], up to the fourth order in ϵ they read

$$\begin{aligned}
\mathcal{E}_x &= \mathcal{E}_0 \mathrm{e}^{-\left(\sqrt{2\ln(2)}\frac{(t-z)}{\tau}\right)^2} \mathrm{e}^{-\frac{r^2}{w^2(z)}} \left(S_1 + \epsilon^2 \left[\nu^2 S_3 - \frac{\rho^4 S_4}{4} \right] \right. \\
&\quad \left. + \epsilon^4 \left[\frac{S_3}{8} - \frac{\rho^2 S_4}{4} - \frac{\rho^2(\rho^2 - 16\nu^2) S_5}{16} - \frac{\rho^4(\rho^2 + 2\nu^2) S_6}{8} + \frac{\rho^8 S_7}{32} \right] + \mathcal{O}(\epsilon^6) \right), \\
\mathcal{E}_y &= \mathcal{E}_0 \nu\eta \mathrm{e}^{-\left(\sqrt{2\ln(2)}\frac{(t-z)}{\tau}\right)^2} \mathrm{e}^{-\frac{r^2}{w^2(z)}} \left(\epsilon^2 S_3 + \epsilon^4 \left[\rho^2 S_5 - \frac{\rho^4 S_6}{4} \right] + \mathcal{O}(\epsilon^5) \right), \\
\mathcal{E}_z &= \mathcal{E}_0 \nu \mathrm{e}^{-\left(\sqrt{2\ln(2)}\frac{(t-z)}{\tau}\right)^2} \mathrm{e}^{-\frac{r^2}{w^2(z)}} \left(\epsilon S_2 + \epsilon^3 \left[-\frac{S_3}{2} + \rho^2 S_4 - \frac{\rho^4 S_5}{4} \right] + \mathcal{O}(\epsilon^5) \right),
\end{aligned} \tag{C.11}$$

$$\mathcal{B}_x = 0, \quad \mathcal{B}_z = \mathcal{E}_0 \eta \mathrm{e}^{-\left(\sqrt{2\ln(2)}\frac{(t-z)}{\tau}\right)^2} \mathrm{e}^{-\frac{r^2}{w^2(z)}} \left(\epsilon S_2 + \epsilon^3 \left[\frac{S_3}{2} + \frac{\rho^2 S_4}{2} - \frac{\rho^4 S_5}{4} \right] + \mathcal{O}(\epsilon^5) \right)$$
$$\mathcal{B}_y = \mathcal{E}_0 \mathrm{e}^{-\left(\sqrt{2\ln(2)}\frac{(t-z)}{\tau}\right)^2} \mathrm{e}^{-\frac{r^2}{w^2(z)}} \left(S_1 + \epsilon^2 \left[\frac{\rho^2 S_3}{2} - \frac{\rho^4 S_4}{4} \right] \right.$$
$$\left. + \epsilon^4 \left[-\frac{S_3}{8} + \frac{\rho^2 S_4}{4} + \frac{5\rho^4 S_5}{16} - \frac{\rho^6 S_6}{4} + \frac{\rho^8 S_7}{32} \right] + \mathcal{O}(\epsilon^6) \right). \tag{C.12}$$

In these formulae $\nu = x/w_0$, $\eta = y/w_0$, $\rho^2 = \nu^2 + \eta^2$ and

$$S_n = \left(\frac{1}{\sqrt{1+\zeta(z)^2}} \right)^n \sin\left[\Phi + (n-1)\ \arctan(\zeta)\right],$$

$$C_n = \left(\frac{1}{\sqrt{1+\zeta(z)^2}} \right)^n \cos\left[\Phi + (n-1)\ \arctan(\zeta)\right],$$

where an explicit expression for Φ can be found in Eq. (4.2). Moreover, the pulse energy calculated with accuracy up to the fourth order in ϵ is equal to

$$W_{\mathrm{BPA}} \approx \frac{\mathcal{E}_0^2}{2} \frac{\pi w_0^2}{2} \left(1 + \frac{\epsilon^2}{4} + \frac{\epsilon^4}{8} \right) \frac{\tau}{2} \sqrt{\frac{\pi}{\ln(2)}}. \tag{C.13}$$

Bibliography

[1] G. Breit and J. A. Wheeler, Collision of two light quanta, Phys. Rev. **46**, 1087 (1934)

[2] A. I. Nikishov and V. I. Ritus, Quantum processes in the field of a plane electromagnetic wave and in constant field I, Zh. Eksp. Teor. Fiz. **46**, 776 (1963)

[3] V. I. Ritus, Quantum effects of the interaction of elementary particles with an intense electromagnetic field, J. Sov. Laser Res. **6**, 497 (1985)

[4] A. I. Nikishov and V. I. Ritus, Pair production by a photon and photon emission by an electron in the field of an intense electromagnetic wave and in a constant field, Zh. Eksp. Teor. Fiz. **52**, 1707 (1967)

[5] V. I. Ritus, Radiative effects and their enhancement in an intense electromagnetic field, Zh. Eksp. Teor. Fiz **57**, 2176 (1969)

[6] D. L. Burke et al., Positron Production in Multiphoton Light-by-Light Scattering, Phys. Rev. Lett. **79**, 1626 (1997)

[7] C. Bamber et al., Studies of nonlinear QED in collisions of 44.6 GeV electrons with intense laser pulses, Phys. Rev. D **60**, 092004 (1999)

[8] H. R. Reiss, Special analytical properties of ultrastrong coherent fields, Eur. Phys. J. D **55**, 365 (2009)

[9] H. Hu, C. Müller and C. H. Keitel, Complete QED Theory of Multiphoton Trident Pair Production in Strong Laser Fields, Phys. Rev. Lett. **105**, 080401 (2010)

[10] J. Adam et al. (STAR Collaboration), Measurement of e^+e^- Momentum and Angular Distributions from Linearly Polarized Photon Collisions, Phys. Rev. Lett. **127**, 052302 (2021)

[11] B. King, H. Gies and A. Di Piazza, Pair production in a plane wave by thermal background photons, Phys. Rev. D **86**, 125007 (2012)

[12] O. J. Pike, F. Mackenroth, E. G. Hill and S. J. Rose, A photon-photon collider in a vacuum hohlraum, Nat. Photonics **8**, 434 (2014)

[13] I. Drebot, D. Micieli, E. Milotti, V. Petrillo, E. Tassi and L. Serafini, Matter from light-light scattering via Breit-Wheeler events produced by two interacting Coulomb sources, Phys. Rev. Accel. Beams **20**, 043402 (2017)

[14] X. Ribeyre, E. d'Humières, O. Jansen, S. Jequier, V. T. Tikhonchuk and M. Lobet, Pair creation in collision of γ-ray beams produced with high-intensity lasers, Phys. Rev. E **93**, 013201 (2016)

[15] T. Wang, X. Ribeyre, Z. Gong, O. Jansen, E. d'Humières, D. Stutman, T. Toncian and A. Arefiev, Power scaling for collimated γ-ray beams generated by structured laser-irradiated targets and its application to two-photon pair production, Phys. Rev. Applied **13**, 054024 (2020)

[16] B. Kettle et al., A laser-plasma platform for photon-photon physics: the two photon Breit-Wheeler process, New J. Phys. **23** 115006 (2021)

[17] A. Di Piazza, C. Müller, K. Z. Hatsagortsyan and C. H. Keitel, Extremely high-intensity laser interactions with fundamental quantum systems, Rev. Mod. Phys. **84**, 1177 (2012)

[18] A. Fedotov, A. Ilderton, F. Karbstein, B. King, D. Seipt, H. Taya and G. Torgrimsson, Advances in QED with intense background fields, arXiv:2203.00019

[19] H. Abramowicz et al., Letter of intent for the LUXE experiment, arXiv:1909.00860; H. Abramowicz et al., Conceptual design report for the LUXE experiment, Eur. Phys. J.: Spec. Top. **230**, 2445 (2021)

[20] S. Meuren, E-320 collaboration at FACET-II, https://facet.slac.stanford.edu [accessed 13 December 2022]

[21] C. H. Keitel et al., Photo-induced pair production and strong field QED on Gemini, arxiv:2103.06059

[22] A. I. Titov, H. Takabe, B. Kämpfer and A. Hosaka, Enhanced Subthreshold e^+e^- Production in Short Laser Pulses, Phys. Rev. Lett. **108**, 240406 (2012)

[23] A. I. Titov, H. Takabe, B. Kämpfer and A. Hosaka, Breit-Wheeler process in very short electromagnetic pulses, Phys. Rev. A **87**, 042106 (2013)

[24] S. Meuren, K. Z. Hatsagortsyan, C. H. Keitel and A. Di Piazza, Polarization-operator approach to pair creation in short laser pulses, Phys. Rev. D **91**, 013009 (2015)

[25] A. Di Piazza, Nonlinear Breit-Wheeler Pair Production in a Tightly Focused Laser Beam, Phys. Rev. Lett. **117**, 213201 (2016)

[26] M. J. A. Jansen and C. Müller, Strong-field Breit-Wheeler pair production in two consecutive laser pulses with variable time delay, Phys. Lett. B **766**, 71 (2017)

[27] Q. Z. Lv, S. Dong, Y. T. Li, Z. M. Sheng, Q. Su and R. Grobe, Role of the spatial inhomogeneity on the laserinduced vacuum decay, Phys. Rev. A **97**, 022515 (2018)

[28] A. I. Titov, H. Takabe and B. Kämpfer, Breit-Wheeler process in short laser double pulses, Phys. Rev. D **98**, 036022 (2018)

[29] A. I. Titov and B. Kämpfer, Nonlinear Breit-Wheeler process with linearly polarized beams, Eur. Phys. J. D **74**, 218 (2020)

[30] S. Tang and B. King, Pulse envelope effects in nonlinear Breit-Wheeler pair creation, Phys. Rev. D **104**, 096019 (2021)

[31] A. Mercuri-Baron, M. Grech, F. Niel, A. Grassi, M. Lobet, A. Di Piazza and C. Riconda, Impact of the laser spatiotemporal shape on Breit-Wheeler pair production, New J. Phys. **23**, 085006 (2021)

[32] T. G. Blackburn and M. Marklund, Nonlinear Breit-Wheeler pair creation with bremsstrahlung γ rays, Plasma Phys. Controlled Fusion **60**, 054009 (2018)

[33] F. C. Salgado et al., Towards pair production in the non-perturbative regime, New J. Phys. **23**, 105002 (2021)

[34] M. D. Shwartz, Quantum Field Theory and the Standard Model, Cambridge University Press (2014)

[35] R. Greiner, Field Quantization, Springer-Verlag Berlin Heidelberg (1996)

[36] S. Weinberg, The Quantum Theory of Fields. Vol.1 Foundations, Cambridge University Press (1995)

[37] R. J. Glauber, The Quantum Theory of Optical Coherence, Phys. Rev. **130**, 2529 (1963)

[38] R. J. Glauber, Coherent and Incoherent States of the Radiation Field, Phys. Rev. **131**, 2766 (1963)

[39] E. S. Fradkin, D. M. Gitman and Sh. M. Shvartsman, Quantum Electrodynamics with Unstable Vacuum, Springer-Verlag Berlin Heidelberg (1991)

[40] J. Bergou and S. Varro, Nonlinear scattering processes in the presence of a quantised radiation field: II. Relativistic treatment, J. Phys. A **14**, 2281 (1981)

[41] D. Seipt, T. Heinzl, M. Marklund and S. S. Bulanov, Depletion of Intense Fields, Phys. Rev. Lett. **118**, 154803 (2017)

[42] A. Ilderton and D. Seipt, Backreaction on background fields: A coherent state approach, Phys. Rev. D **97**, 016007 (2018)

[43] W. H. Furry, On Bound States and Scattering in Positron Theory, Phys. Rev. **81**, 115 (1950)

[44] D. M. Volkov, Über eine Klasse von Lösungen der Diracschen Gleichung, Z. Phys. **94**, 250 (1935)

[45] W. B. Berestetzki, E. M. Lifschitz and L. P. Pitajewski, Quantenelektrodynamik, Akademie-Verlag Berlin (1989)

[46] J. Schwinger, On Gauge Invariance and Vacuum Polarization, Phys. Rev. **82**, 664 (1951)

[47] V. I. Ritus, Radiative corrections in quantum electrodynamics with intense field and their analytical properties, Ann. Phys. **69**, 555 (1972)

[48] M. Boca and V. Florescu, The completeness of Volkov spinors , Rom. Journ. Phys. **55**, 511 (2010)

[49] S. Zakowicz, Square-integrable wave packets from the Volkov solutions, J. Math. Phys.**46**, 032304 (2005)

[50] H. R. Reiss, Effect of an intense electromagnetic field on a weakly bound system, Phys. Rev. A **22**, 1786 (1980)

[51] A. Golub, S. Villalba-Chávez and C. Müller, Nonlinear Breit-Wheeler pair production in collisions of bremsstrahlung γ quanta and a tightly focussed laser pulse, Phys. Rev. D, **105**, 116016 (2022)

[52] F. W. J. Olver, D. W. Lozier, R. F. Boisvert and C. W. Clark, NIST Handbook of Mathematical Functions, Cambridge University Press (2010)

[53] H. R. Reiss, Production of Electron Pairs from a Zero-Mass State, Phys. Rev. Lett. **26**, 1072 (1971)

[54] A. Hartin, A. Ringwald and N. Tapia, Measuring the boiling point of the vacuum of quantum electrodynamics, Phys. Rev. D **99**, 036008 (2019)

[55] A. Eckey, A. B. Voitkiv and C. Müller, Strong-field Breit- Wheeler pair production with bremsstrahlung γ rays in the perturbative-to-nonperturbative transition regime, Phys. Rev. A **105**, 013105 (2022)

[56] A. J. Gonsalves et al., Petawatt Laser Guiding and Electron Beam Acceleration to 8 GeV in a Laser-Heated Capillary Discharge Waveguide, Phys. Rev. Lett. **122**, 084801 (2019)

[57] G. Götzfried et al., Physics of Nanocoulomb-Class Electron Beams in Laser-Plasma Wakefields, Phys. Rev. X **10**, 041015 (2020)

[58] H. Chen et al., Relativistic Positron Creation Using Ultraintense Short Pulse Lasers, Phys. Rev. Lett. **102**, 105001 (2009)

[59] G. Sarri et al., Table-Top Laser-Based Source of Femtosecond, Collimated, Ultrarelativistic Positron Beams, Phys. Rev. Lett. **110**, 255002 (2013)

[60] A. Golub, S. Villalba-Chávez and C. Müller, Linear Breit-Wheeler pair production by high-energy bremsstrahlung photons colliding with an intense x-ray laser pulse, Phys. Rev. D **103**, 016009 (2021)

[61] Y. I. Salamin, Fields of Gaussian beam beyond paraxial approximation, Appl. Phys. B **86**, 319 (2007)

[62] P. A. Zyla et al. (Particle Data Group), Review of Particle Physics, Prog. Theor. Exp. Phys. **2020**, 083C01 (2020)

[63] Y.-S. Tsai, Pair production and bremsstrahlung of charged leptons, Rev. Mod. Phys.**46**, 815 (1974)

[64] E. Esarey, P. Sprangle, J. Krall and A. Ting, Overview of plasma-based accelerator concepts, IEEE Trans. Plasma Sci. **24**, 252 (1996)

[65] E. Esarey, C. B. Schroeder and W. P. Leemans, Physics of laser-driven plasma-based electron accelerators, Rev. Mod. Phys. **81**, 1229 (2009)

[66] M. Lobet, X. Davoine, E. d'Humiéres and L. Gremillet, Generation of high-energy electron-positron pairs in the collision of a laser-accelerated electron beam with a multipetawatt laser, Phys. Rev. Accel. Beams **20**, 043401 (2017)

[67] G. Geloni et. al., Coherence properties of the European XFEL, New J. Phys. **12**, 035021 (2010)

[68] E. A. Schneidmiller and M. V. Yurkov, Coherence properties of the radiation from FLASH, J. Mod. Opt. **63**, 293 (2016)

[69] C. Gutt et al., Single Shot Spatial and Temporal Coherence Properties of the SLAC Linac Coherent Light Source in the Hard X-Ray Regime, Phys. Rev. Lett. **108**, 024801 (2012)

[70] W. P. Leemans et al., Multi-GeV Electron Beams from Capillary-Discharge-Guided Subpetawatt Laser Pulses in the Self-Trapping Regime, Phys. Rev. Lett. **113**, 245002 (2014)

[71] http://www.hibef.eu/ [accessed 13 December 2022]

[72] https://lcls.slac.stanford.edu/parameters [accessed 13 December 2022]

[73] A. Hartin, A. Ringwald and N. Tapia, Measuring the boiling point of the vacuum of quantum electrodynamics, Phys. Rev. D **99**, 036008 (2019)

[74] A. Di Piazza, M. Tamburini, S. Meuren and C. H. Keitel, Improved local-constant-field approximation for strongfield QED codes, Phys. Rev. A **99**, 022125 (2019)

[75] S. S. Bulanov, V. D. Mur, N. B. Narozhny, J. Nees and V. S. Popov, Multiple Colliding Electromagnetic Pulses: A Way to Lower the Threshold of e^+e^- Pair Production from Vacuum, Phys. Rev. Lett. **104**, 220404 (2010)

[76] A. Fedotov, A. Ilderton, F. Karbstein, B. King, D. Seipt, H. Taya and G. Torgrimsson, Advances in QED with intense background fields, arXiv:2203.00019

[77] R. A. Neville and F. Rohrlich, Quantum electrodynamics on null planes and applications to lasers, Phys. Rev. D **3**, 1692 (1971)

[78] W. Becker and H. Mitter, Vacuum polarization in laser fields, J. Phys. A **8**, 1638 (1975)

[79] A. Di Piazza, M. Tamburini, S. Meuren and C. H. Keitel, Implementing nonlinear Compton scattering beyond the local-constant-field approximation, Phys. Rev. A **98**, 012134 (2018)

[80] K. Gillen-Christandl, G. D. Gillen, M. J. Piotrowicz and M. Saffman, Comparison of Gaussian and super Gaussian laser beams for addressing atomic qubits, Appl. Phys. B **122**, 131 (2016)

[81] M. Santarsiero and R. Borghi, Correspondence between super-Gaussian and flattened Gaussian beams, J. Opt. Soc. Am. A **16**, 188 (1999)

[82] L. Fister, R. Alkofer and K. Schwenzer, On the infrared behavior of Landau Gauge Yang-Mills theory with a fundamentally charged scalar field, Phys. Lett. B **688**, 237 (2010)

[83] T. Banks and M. O'Loughlin, Two-dimensional quantum gravity in Minkowski space, Nucl. Phys. B **362**, 649 (1991)

[84] R. Prange and S. Girvin, The Quantum Hall Effect, Springer-Verlag, New York, 1990

[85] S. Desser, R. Jakiw and S. Templeton, Topologically massive gauge theories, Ann. Phys. (N.Y.) **140**, 372 (1982)

[86] Q. Lin, Electron-positron pair creation in a vacuum by an electromagnetic field in 3+1 and lower dimensions, J. Phys. G **25**, 17 (1999)

[87] S. P. Gavrilov and D. M. Gitman, Vacuum instability in external fields, Phys. Rev. D **53**, 7162 (1996)

[88] Y. Lu, N. Christensen, Q. Su and R. Grobe, Space-time resolved Breit-Wheeler process for a model system, Phys. Rev. A **101**, 022503 (2020)

[89] Q. Z. Lv, N. D. Christensen, Q. Su and R. Grobe, Validity of one-dimensional QED for a system with spatial symmetry, Phys. Rev. A **92**, 052115 (2015)

[90] E. A. Martinez et al., Real-time dynamics of lattice gauge theories with a few-qubit quantum computer, Nature (London) **534**, 516 (2016)

[91] A. N. Pieiro, D. Genkina, M. Lu and I. B. Spielman, Sauter-Schwinger effect with a quantum gas, New J. Phys. **21**, 083035 (2019)

[92] N. Szpak and R. Schützhold, Quantum simulator for the Schwinger effect with atoms in bichromatic optical lattices, Phys. Rev. A **84**, 050101(R) (2011)

[93] N. Szpak and R. Schützhold, Optical lattice quantum simulator for quantum electrodynamics in strong external fields: spontaneous pair creation and the Sauter-Schwinger effect, New J. Phys. **14**, 035001 (2012)

[94] T. Pichler, M. Dalmonte, E. Rico, P. Zoller and S. Montangero, Real-Time Dynamics in $U(1)$ Lattice Gauge Theories with Tensor Networks, Phys. Rev. X **6**, 011023 (2016)

[95] E. Zohar, A. Farace, B. Reznik, and J. Ignacio Cirac, Digital Quantum Simulation of Z_2 Lattice Gauge Theories with Dynamical Fermionic Matter, Phys. Rev. Lett. **118**, 070501 (2017)

[96] T. V. Zache et al., Quantum simulation of lattice gauge theories using Wilson fermions, Quantum Sci. Technol. **3**, 034010 (2018)

[97] L. Klar, N. Szpak and R. Schützhold, Quantum simulation of spontaneous pair creation in 2D optical lattices, arXiv:1901.09880

[98] R. Ott, T. V. Zache, N. Müller and J. Berges, Noncancellation of the parity anomaly in the strong-field regime of QED_{2+1}, Phys. Lett. B **805**, 135459 (2020)

[99] J. M. Guilarte and M. de la Torre Mayado, QED_{2+1}: The Compton effect, An. Fis. (Spain) **6**, 237 (2002), arXiv:hep-th/0009003

[100] A. Golub, S. Villalba-Chávez and C. Müller, Strong-field Breit-Wheeler pair production in QED_{2+1}, Phys. Rev. D **103**, 096002 (2021)

[101] D. Boito, L. N. S. de Andrade, G. de Sousa, R. Gama, C. Y. M. London,On Maxwell's electrodynamics in two spatial dimensions, Rev. Bras. Ens. Fís. **42**, e20190323 (2020)

[102] S. Bellucci, A. A. Saharian and V. M. Bardeghyan, Induced fermionic current in toroidally compactified spacetimes with applications to cylindrical and toroidal nanotubes, Phys. Rev. D **82**, 065011 (2010)

[103] I. S. Gradshtein and I. M. Ryzhik, Table of Integrals, Series, and Products (Sixth Edition) Academic Press, New York, (2000)

[104] D. E. Aspnes, Electric-field effects on optical absorption near threshold in solids, Phys. Rev. **147**, 554 (1966)

[105] A. A. Mironov, S. Meuren and A. M. Fedotov, Resummation of QED radiative corrections in a strong constant crossed field, Phys. Rev. D **102**, 053005 (2020)

[106] T. Podszus and A. Di Piazza, High-energy behavior of strong-field QED in an intense plane wave, Phys. Rev. D **99**, 076004 (2019)

[107] A. Ilderton, Note on the conjectured breakdown of QED perturbation theory in strong fields, Phys. Rev. D **99** 085002 (2019),

[108] M. I. Katsnelson, K. S. Novoselov and A. K. Geim, Chiral tunnelling and the Klein paradox in graphene, Nat. Phys. **2**, 620 (2006)

[109] A. A. Banishev, H. Wen, J. Xu, R. K. Kawakami, G. L. Klimchitskaya, V. M. Mostepanenko and U. Mohideen, Measuring the Casimir force gradient from graphene on a SiO_2 substrate, Phys. Rev. B **87**, 205433 (2013)

[110] V. M. Pereira, J. Nilsson, and A. H. Castro Neto, Coulomb Impurity Problem in Graphene, Phys. Rev. Lett. **99**, 166802 (2007)

[111] I. S. Terekhov, A. I. Milstein, V. N. Kotov and O. P. Sushkov, Screening of Coulomb Impurities in Graphene, Phys. Rev. Lett. **100**, 076803 (2008)

[112] D. Allor, T. D. Cohen and D. A. McGady, The Schwinger mechanism and graphene, Phys. Rev. D **78**, 096009 (2008)

[113] M. Lewkowicz and B. Rosenstein, Dynamics of Particle- Hole Pair Creation in Graphene, Phys. Rev. Lett. **102**, 106802 (2009)

[114] B. Dora and R. Moessner, Nonlinear electric transport in graphene: Quantum quench dynamics and the Schwinger mechanism, Phys. Rev. B **81**, 165431 (2010)

[115] S. P. Gavrilov, D. M. Gitman and N. Yokomizo, Dirac fermions in strong electric field and quantum transport in graphene, Phys. Rev. D **86**, 125022 (2012)

[116] G. L. Klimchitskaya and V. M. Mostepanenko, Creation of quasiparticles in graphene by a time-dependent electric field, Phys. Rev. D **87**, 125011 (2013)

[117] H. K. Avetissian, A. K. Avetissian, G. F. Mkrtchian and Kh. V. Sedrakian, Creation of particle-hole superposition states in graphene at multiphoton resonant excitation by laser radiation, Phys. Rev. B **85**, 115443 (2012)

[118] F. Fillion-Gourdeau and S. MacLean, Time-dependent pair creation and the Schwinger mechanism in graphene, Phys. Rev. B **92**, 035401 (2015)

[119] I. Akal, R. Egger, C. Müller, and S. Villalba-Chávez, Low-dimensional approach to pair production in an oscillating electric field: Application to bandgap graphene layers, Phys. Rev. D **93**, 116006 (2016)

[120] I. Akal, R. Egger, C. Müller and S. Villalba-Chávez, Simulating dynamically assisted production of Dirac pairs in gapped graphene monolayers, Phys. Rev. D **99**, 016025 (2019)

[121] A. Golub, R. Egger, C. Müller and S. Villalba-Chávez, Dimensionality-driven photoproduction of massive Dirac pairs near threshold in gapped graphene monolayers, Phys. Rev. Lett. **124**, 110403 (2020)

[122] http://link.aps.org/supplemental/10.1103/PhysRevLett.124.110403 [accessed 13 December 2022]

[123] E. C. Marino, Quantum Field Theory Approach to Condensed Matter Physics, Cambridge University Press, (2017)

[124] P. Kim, Graphene and Relativistic Quantum Physics, Progress in Mathematical Physics **71**, 1-23 Springer International Publishing (2017)

[125] V. P. Gusynin, S. G. Sharapov and J. P. Carbotte, AC conductivity of graphene: from tight-binding model to 2+1-dimensional quantum electrodynamics, Int. J. Mod. Phys. **B21**, 4611 (2007)

[126] S. Y. Zhou, G.-H. Gweon, A. V. Fedorov, P. N. First, W. A. de Heer, D.-H. Lee, F. Guinea, A. H. Castro Neto and A. Lanzara, Substrate-induced band gap opening in epitaxial graphene, Nat. Mater. **6**, 770 (2007)

[127] A. Varykhalov, J. Sánchez-Barriga, A. M. Shikin, C. Biswas, E. Vescovo, A. Rybkin, D. Marchenko and O. Rader, Electronic and Magnetic Properties of Quasifreestanding Graphene on Ni, Phys. Rev. Lett. **101**, 157601 (2008)

[128] A. K. Geim and I. V. Grigorieva, Van der Waals heterostructures, Nature (London) **499**, 419 (2013),

[129] B. Liu and K. Zhou, Recent progress on graphene-analogous 2D nanomaterials: Properties, modeling and applications, Prog. Mater. Sci. **100**, 99 (2019)

[130] M. Yankowitz, Q. Ma, P. Jarillo-Herrero and B. J. LeRoy, van der Waals heterostructures combining graphene and hexagonal boron nitride, Nat. Rev. Phys. **1**, 112 (2019)

[131] G. Giovannetti, P. A. Khomyakov, G. Brocks, P. J. Kelly and J. van den Brink, Substrate-induced band gap in graphene on hexagonal boron nitride: Ab initio density functional calculations, Phys. Rev. B **76**, 073103 (2007)

[132] S. Varró, New exact solutions of the Dirac equation of a charged particle interacting with an electromagnetic plane wave in a medium, Laser Phys. Lett. **10**, 095301 (2013)

[133] M. Oliva-Leyva and G. G. Naumis, Sound waves induce Volkov-like states, band structure and collimation effect in graphene, J. Phys. Condens. Matter **28**, 025301 (2016)

[134] M. Mecklenburg, J. Woo and B. C. Regan, Tree-level electron-photon interactions in graphene, Phys. Rev. B **81**, 245401 (2010)

[135] M. Lewkowicz, H. C. Kao and B. Rosenstein, Signature of the Schwinger pair creation rate via radiation generated in graphene by a a strong electric current, Phys. Rev. B **84**, 035414 (2011)

[136] W. B. Berestetzki, E. M. Lifschitz and L. P. Pitajewski, Quantenelektrodynamik, Akademie Verlag, Berlin (1991)

[137] R. J. Gould, Born-approximation and radiative corrections to pair production in photon-photon collisions, Astrophys. J. **337**, 950 (1989)

[138] J. Reimann et al., Subcycle observation of lightwave-driven Dirac currents in a topological surface band, Nature (London) **562**, 396 (2018)

[139] D. J. Cook and R. M. Hochstrasser, Intense terahertz pulses by four-wave rectification in air, Opt. Lett. **25**, 1210 (2000)

[140] T. Bartel, P. Gaal, K. Reimann, M. Woerner and T. Elsaesser, Generation of single-cycle THz transients with high electric-field amplitudes, Opt. Lett. **30**, 2805 (2005)

[141] A. Di Piazza, Ultrarelativistic Electron States in a General Background Electromagnetic Field, Phys. Rev. Lett. **113**, 040402 (2014)

[142] T. Higuchi, C. Heide, K. Ullmann, H. B. Weber and P. Hommelhoff, Light-field-driven currents in graphene, Nature **555**, 224 (2017)

[143] V. P. Krainov, H. R. Reiss and B. M. Smirnov, Radiative processes in atomic physics, John Wiley and Sons (1997)

[144] M. J. Ablowitz and A. S. Fokas, Complex Variables: Introduction and Applications, Cambridge University Press (2003)

[145] H. J. Korsch, A. Klumpp and D. Witthaut, On two-dimensional Bessel functions, J. Phys. A: Math. Gen. **39**, 14947 (2006)

[146] M. H. Mittleman, Multiphoton pair creation, Phys. Rev. A **35**, 4624 (1987)

[147] C. Leubner, Uniform asymptotic expansion of a class of generalized Bessel functions occuring in the study of fundamental scattering processesin intense laser fields, Phys. Rev. A **23**, 2877 (1981)

[148] W. J. Waters and B. King, On beam models and their paraxial approximation, Laser Phys. **28**, 015003 (2018)

Eidesstattliche Versicherung

Ich versichere an Eides Statt, dass die Dissertation von mir selbständig und ohne unzulässige fremde Hilfe unter Beachtung der "Grundsätze zur Sicherung guter wissenschaftlicher Praxis an der Heinrich-Heine-Universität Düsseldorf" erstellt worden ist. Ich habe keine anderen als die im Literaturverzeichnis angegebenen Quellen genutzt; wörtliche oder sinngemäße Inhalte anderer Werke oder Quellen sind als solche kenntlich gemacht. Weiterhin erkläre ich, dass die vorliegende Arbeit zuvor weder von mir, noch - soweit mir bekannt - von anderen Personen an dieser oder an einer anderen Hochschule eingereicht wurde und ich bisher weder erfolglose noch erfolgreiche Promotionsversuche unternommen habe. Darüber hinaus ist mir bekannt, dass jeder Betrugsversuch zum Nichtbestehen oder zur Aberkennung der Prüfungsleistung führen kann.

Düsseldorf, 14th December 2022 _____

Alina Golub